Doped ZnO nanostructures for optoelectronics: growth, properties and devices

Md. Azizar Rahman

A thesis submitted in fulfilment for the degree of Doctor of Philosophy

School of Mathematical & Physical Sciences
Faculty of Science

UNIVERSITY OF TECHNOLOGY SYDNEY
AUSTRALIA

January 2019

Declaration of Authorship

I certify that the work in this thesis has not previously been submitted for a degree nor has it been submitted as part of requirements for a degree except as part of the collaborative doctoral degree and/or fully acknowledged within the text.

I also certify that the thesis has been written by me. Any help that I have received in my research work and the preparation of the thesis itself has been acknowledged. In addition, I certify that all information sources and literature used are indicated in the thesis.

This research is supported by an Australian Government Research Training Program Scholarship.

Production Note:
Signature removed prior to publication.

Signature of Student

Date: 05-01-2019

Abstract

Zinc oxide (ZnO) semiconductor is a highly attractive material for optoelectronic and photonic applications due to its high exciton binding energy (60 meV) and large bandgap (3.37 eV) at room temperature. In addition, ZnO doped with group III elements is a promising system for wavelength-tunable plasmonics because of its low absorption loss in the infrared region compared with metals. However, poor understanding of native defects and of their interaction with impurities has limited the development of practical ZnO-based photonic and plasmonic devices. The primary aim of this project was to investigate the effects of the incorporation of donor and acceptor impurities on the optoelectronic properties of ZnO nanostructures and to exploit new properties in optoelectronic devices.

First, Li dopants were used to produce multi-colour emitting ZnO films fabricated by the spray pyrolysis technique. The pyrolytic films exhibit multi-colour emissions of yellow, green and blue, which can be tuned by varying the Li concentration. Simulation of the cathodoluminescence spectra from the Li-doped films using the Huang-Rhys model enables the determination of the energy levels of luminescence centres and their electron-phonon coupling strength. These centres are attributable to either V_{Zn} or Li_{Zn} acceptor states.

Second, Ga was used to enhance the electrical and optical properties of ZnO nanorods. A large number of ZnO nanowires and nanorods were fabricated with various Ga concentration up to 1.4 at% by the vapour phase transport method. It was found that Ga incorporation activates the Cu luminescence centres, which lead to the emergence of a characteristic fine structure in the green luminescence (GL) band of ZnO. The emergence of the structured GL is due to the Cu^+ state being stabilized by the rise in the Fermi level above the 0/- (Cu^{2+}/Cu^{+}) charge transfer level as a result of Ga donor incorporation. From a combination of optical characterisation and simulation using the Brownian oscillator model, the doublet fine structures are shown to originate from two hole transitions with the Cu^{+} state located at 390 meV above the valence band.

Third, bandgap engineering in a single ZnO microrod was demonstrated through crystal defect mediation. ZnO microrods with graded distribution of Ga dopants were fabricated by the vapour phase transport method. The near-band-edge (NBE) emission of the graded microrods was found to be red shifted by ~ 0.6 eV due to the merging of Ga-related impurity bands with the ZnO energy bands, consistent with the bandgap shift as calculated by the Density Function Theory. The results demonstrate self-regulation of charged defect compensation and the possibility of multi-wavelength light sources within a microrod.

Finally, Ga-doped ZnO nanorods were optimised and electrically integrated into Si-based photonic devices in order to fabricate light emitting diodes (LEDs). LEDs fabricated from the Ga-doped ZnO nanorod/p-Si heterojunction display bright and colour-tunable electroluminescence (EL). These nanorod LEDs possess a dramatically enhanced performance and an order of magnitude higher EL compared with equivalent LED devices made with pristine nanorods. These results point to an effective route for large-scale fabrication of conductive, single-crystalline Ga-doped ZnO nanorods for photonic and optoelectronic applications.

Acknowledgements

First of all, I express my profound gratitude to my supervisors A/Prof. Cuong Ton-That, Prof. Matthew Ronald Phillips, Dr. Angus Gentle for their constructive criticism, continuous guidance, and inspiration in conducting my PhD research and writing up this thesis. I would like to thank Geoff McCredie, Katie McBean, Herbert Yuan, and Mark Berkahn for giving me the valuable technical support in my experimental work in the Microstructural Analysis Unit.

I appreciate the assistance of Sumin Choi and Saskia Fiedler have provided me in photoluminescence and X-ray photoelectron spectroscopy experiments, respectively. I am grateful to Sajid Ali, my friend, for helping with theoretical bandgap calculations of Ga-doped ZnO. I would like to thank Mika T. Westerhausen for the ICP-MS measurements of Ga-doped ZnO nanowires. I am also grateful to John Scott for his useful advice on TEM. I am also thankful to Liangchen Zhu and Olivier Lee for their valuable tips and suggestions on the use of the cathodoluminescence spectrometer.

Finally, I would like to express my special gratefulness to my family, especially Urfi Tabassum, for their moral support and sustaining inspiration. This dissertation would never be possible without their love and affection.

List of Publications

Journal papers

1. **M. Azizar Rahman**, Matthew R. Phillips, Cuong Ton-That, "Efficient multi-coloured Li-doped ZnO thin films fabricated by spray Pyrolysis" Journal of Alloys and Compounds, 691 (2017) 339.

2. **M. Azizar Rahman**, Mika T. Westerhausen, Christian Nenstiel, Sumin Choi, Axel Hoffmann, Angus Gentle, Matthew R. Phillips, and Cuong Ton-That, "Charge state switching of Cu acceptors in ZnO nanorods", Applied Physics Letters, 110 (2017) 121907.

3. **M. Azizar Rahman**, John A. Scott, A. Gentle, Matthew R. Phillips, Cuong Ton-That, "A facile method for bright, colour-tunable light-emitting diodes based on Ga-doped ZnO nanorods, Nanotechnology, 29 (2018) 425707.

4. **M. Azizar Rahman**, Sajid Ali, Michael J. Ford, Matthew R. Phillips, and Cuong Ton-That, "Ga-mediated optical emission from ZnO microrods", in preparation.

5. A. M. M. Tanveer Karim, **M. Azizar Rahman,** M. Sazzad Hossain[1], M. K. Rahman Khan, M. Mozibur Rahman, M. Kamruzzaman and Cuong Ton-That "Multi-Colour Excitonic Emissions in Chemical Dip-Coated Organolead Mixed-Halide Perovskite", Chemistry select, 3 (2018) 1

Conference presentations

1. **M. Azizar Rahman**, Matthew R. Phillips, Cuong Ton-That, "Structured green emission band and electron-phonon coupling in Ga-doped ZnO nanowires", ICONN, 7 – 11 February 2016, Canberra, Australia.

2. **M. Azizar Rahman**, A. Gentle, Matthew R. Phillips, Cuong Ton-That, "Activating the Cu acceptors in ZnO nanorods by Ga doping", ICONN, 29 January – 2 February 2018, Wollongong, Australia.

Table of Content

Chapter 1. General background and motivation

Chapter 2. ZnO: defects, impurities and optoelectronic devices

Chapter 3. Experimental details

Chapter 4. Li acceptors in ZnO

Chapter 5. Cu acceptors in ZnO nanorods

Chapter 6. Bandgap engineering and doping of ZnO

Chapter 7. Optimisation of ZnO nanorods for LED devices

Chapter 8. Conclusions and outlook

List of Figures

List of Tables

List of Acronyms

$A^{\circ}X$	Neutral acceptor bound exciton
AFM	Atomic force microscope
BL	Blue luminescence
CL	Cathodoluminescence
CVD	Chemical vapour deposition
CCD	Charge-coupled device
CTL	Charge transfer level
$D^{+}X$	Ionised donor bound exciton
$D^{\circ}X$	Neutral donor bound exciton
DAP	Donor acceptor pair
DL	Deep level
DFT	Density function theory
DOS	Density of state
EL	Electroluminescence
EDS	Energy dispersive spectroscopy
FWHM	Full width at half maximum
FX	Free exciton
GL	Green luminescence
GGA	Generalized gradient approximation
LED	Light Emitting diode
LDA	Local density approximation
LA-ICP-MS	Laser ablated inductively coupled plasma mass spectroscopy
LO	Longitudinal optics
MBO	Multimode Brownian oscillator
MOCVD	Metal-organic chemical vapour deposition
MBE	Molecular beam epitaxy
NBE	Near-band-edge emission
NIST	National institute of standard and technology

NIR	Near infrared region
NRs	Nanorods
PL	Photoluminescence
PMMA	Poly-methyl-methacrylate
PEDOT	Poly(3,4-ethylenedioxythiophene)
RL	Red luminescence
SEM	Scanning electron microscope
SEAD	Selected area diffraction
TEM	Transmission electron microscope
UV	Ultraviolet
VPT	Vapour phase transport
XPS	X-ray photoelectron spectroscopy
XRD	X-ray diffraction
YL	Yellow luminescence
ZPL	Zero phonon line

Chapter 1

General background and motivation

1.1. Background

ZnO is widely recognised as an ideal semiconductor for optoelectronic applications including light-emitting diodes [1], lasers [2] and transparent conducting oxides [3] because of its high exciton binding energy (60 meV) and wide bandgap (3.37 eV) at room temperature. In addition, this material is promising for phosphor applications due to its strong luminescence in the visible region of the spectrum [4]. Moreover, the high thermal conductivity of this material translates high efficiency of heat removal during device operation [5].

Fabrication of reproducible and stable p-type ZnO has remained a major challenge to date. The main reason is that the native point defects of ZnO have a tendency to produce n-type conductivity and play an important role as a compensating centre in p-type doping [5, 6]. Group I elements (Li, Na and K) and group V elements (N, P, As and Pb) have been regarded as most promising p-type dopants for ZnO [7, 8]. It has been reported that the group I elements are more effective dopants than the group-V in terms of the shallowness of the acceptor level [9]. However, the group I elements have a tendency to diffuse into the interstitial sites that compensate the p-type conductivity [10]. The large bond length of group V elements induces donor-like antisites, which degrade the acceptor concentration [6]. Experimentally, several groups have reported p-type conductivity in ZnO [11-13].

But these reports have not been followed up with reports on reproducible p-n junctions, raising questions about stability and reproducibility of p-type ZnO. In order to overcome this challenge, a clear understanding of the role of point defects (vacancies, interstitials and antisites) on the p-type doping in ZnO is necessary.

Recent reports on room temperature ferromagnetism and p-type conduction in Cu-doped ZnO illustrates the wide range of promising applications of this martial in spintronic and photonic devices [14-16]. Room temperature ferromagnetism of Cu-doped ZnO has been reported by several groups [17, 18], conversely, the absence of ferromagnetism in this material was also confirmed by other works [19]. The origin of ferromagnetism in Cu-doped ZnO is ambiguous since Cu and Zn are not ferromagnetic elements. It has been reported that group IB elements (Cu, Au and Ag) act as deep acceptors in ZnO and do not contribute to the p-type conduction [5]. Photoluminescence experiments have shown that Cu impurity is responsible for the fine structure in the green emission band of ZnO [20, 21]. On the other hand, Reynold et al. reported that the structured green emission band in ZnO is due to the transitions of two shallow donors to V_{Zn} acceptor [22]. These inconsistent results highlight the fact that the nature of Cu acceptors in ZnO and its role in the optical, electrical and magnetic properties is highly controversial.

Group III elements (Ga, Al and In) have been reported as n-type dopants in ZnO and have a strong effect on the formation of intrinsic defects and optoelectronic properties of this material [23-25]. In addition, ZnO doped with these elements has been suggested as an alternative to traditional plasmonic materials (Au and Ag) due to their low optical loss in the visible and near infrared regions [26, 27]. The optical properties of these materials can be further improved if their electronic band structure is engineered to obtain lower optical loss. Among the n-type dopants, Ga has been recognised as one of the most efficient dopants for enhancing the electrical conductivity and has widely been used for engineering the band structure of ZnO [28, 29]. Kim et al. reported that Ga can increase the bandgap of ZnO and makes it more suitable for plasmonic applications [26]. Alternatively, the decrease of the bandgap in ZnO with Ga doping has also been reported [29]. Theoretical and experimental studies have shown that group III elements interact with acceptor-like native defects, producing the abundance of acceptor complexes (Al_{Zn}-V_{Zn} and Ga_{Zn}-V_{Zn}). These acceptors are electrically active [24, 30], but their optical properties have not been studied extensively. The role of Ga-related defects on the optoelectronic properties of ZnO nanostructures has not been clear yet.

ZnO nanowires/nanorods have attracted much attention in the recent years for solid state lighting devices due to their high crystalline quality, short carrier transport distance and high surface-to-volume ratio [31]. In many respects, ZnO is considered as an alternative of GaN for light emitting devices due to its high binding energy and relatively low production cost. Moreover, GaN nanowires and particularly vertically aligned nanowires are difficult to grow. Vertical nanowires/nanorods provide waveguided optical emission, which allows the fabrication of light emitting devices with improved light extraction efficiency [32]. However, the lack of stable p-type ZnO nanowires is a major issue in fabricating homojunction light emitting diodes. In most cases, the light emissions from ZnO nanowires-based light emitting diodes are unstable and incandescent. Vertically aligned ZnO nanowires-based light emitting diodes with low power consumption, high efficiency, low heat output and high colour gamut are still required to replace traditional incandescent and fluorescent lamps.

1.2. Aims of the project

The specific aims of the work described in this thesis were:

- Adapt and refine the vapour phase transport and spray pyrolysis methods to fabricate high-quality Li- and Ga- doped ZnO nanostructures with controlled doping concentrations and optoelectronic properties.
- Determine the main factors that govern those optical and electronic properties of thin films and nano/microrods that are doped with donor and acceptor impurities.
- Determine the chemical origin and characteristics of emissions introduced by the dopants and their effects on the band and defect structure.
- Explore the utility of the optimised electrical properties in ZnO by fabricating and evaluating prototype wavelength-tunable light emitting diodes based on doped ZnO nanorods.

1.3. Structure of the thesis

In this work, doped ZnO nanostructures such as films and nano/microrods were grown successfully by spray pyrolysis and vapour phase transport methods. Additionally, the donor and acceptor impurities in ZnO nanostructures and their effects on the optoelectronic properties of this material have also been demonstrated. Moreover, vertically aligned ZnO nanorods have been electrically integrated into Si-based photonic devices to fabricate light emitting diodes. This thesis is composed of the following chapters.

Chapter 1: Introduction

Chapter 1 gives an overview of current status and future prospects of ZnO-based optoelectronics. This chapter also presents the scope of research in the field of ZnO, and the motivations of this project.

Chapter 2: ZnO: defects, impurities and optoelectronic devices

This chapter focuses the native defects, dopants and unintentional impurities in ZnO. ZnO nanostructures growth mechanism and ZnO-based light emitting applications are also reviewed in this chapter.

Chapter 3: Experimental details

This chapter explains the main experimental techniques employed in this project.

Chapter 4: Li acceptors in ZnO

This chapter focuses on the optical emissions in Li-doped ZnO films. The Li-related defects and their effects on the optical properties of ZnO are also discussed in this chapter.

Chapter 5: Cu acceptors in ZnO nanorods

This chapter explains the switching behaviour of Cu charge state in ZnO nanorods by Ga doping. The optical measurements and simulations of Cu-related green emission band are also presented in this chapter to explain the carrier-mediated conversion of the Cu charge state in ZnO.

Chapter 6: Bandgap engineering and doping of ZnO

This chapter focuses on the bandgap engineering in a single ZnO microrod. The theoretical calculations of Ga-related defects are also presented in this chapter to explain the electronic band structure of Ga-doped ZnO.

Chapter 7: Optimisation of ZnO nanorods for LED devices

This chapter focuses on the optimisation of ZnO nanorod-based light emitting devices. The current-voltage characteristics and light emission behaviour of these devices are also presented in this chapter.

Chapter 8: Conclusions and outlook

This chapter presents the summary of this project and suggestions for future research directions.

Chapter 2

ZnO: defects, impurities and optoelectronic devices

The doping of ZnO nanostructures has attracted much attention over past decades for tuning the optical, electrical and magnetic properties of this material to use in high-performance optoelectronic, photonic and spintronic devices. Group I (Li, Na and K) and group IB (Cu, Au and Ag) elements are potential useful dopants for p-type ZnO. The group I elements are theoretically predicted to be shallow acceptors and are considered for substituting Zn atoms. However, p-type ZnO is unstable and difficult to reproduce due to the self-compensation mechanism of native defects. On the other hand, the group III elements (Ga, Al and In) are well known n-type dopants in ZnO. ZnO can be made highly transparent and conductive by suitably doped with group III elements. The physical properties of doped ZnO nanostructures largely depend on growth methods as well as growth parameters. To fabricate ZnO-based practical devices with optimum physical properties, doping limit in ZnO nanostructures is a debatable issue. This chapter mainly concentrates on the native point defects and defects induced by the group I and group III elements, which are crucial for controlling optoelectronic properties of ZnO. The various defects, which act as donors and acceptors to realise either n-type or p-type are reviewed. This chapter also focuses on the doping of ZnO nanostructures, including an overview of spray pyrolysis method and vapour phase transport method and doped ZnO-based light emitting diodes.

2.1. Native defects in ZnO

Intrinsic or native defects are lattice imperfections in the crystal that involve only constituent elements including interstitials, vacancies and antisites. The most common native defects in ZnO are oxygen vacancies (V_O), zinc interstitials (Zn_i), zinc vacancies (V_{Zn}), oxygen interstitials (O_i), oxygen antisites (O_{Zn}), and zinc antisites (Zn_O). In equilibrium conditions, some defects are optically and electrically active and can influence the optoelectrical properties of ZnO. These defects have a strong interaction with the extrinsic defects and are related to the compensation of donor and acceptor dopants, i.e. acceptor defects are easier to form in n-type ZnO, while donor defects are easier to form in p-type ZnO. The control, formation and evaluation of native defects have been studied by both theoretically and experimentally [5, 33, 34]. However, the origin of residual n-type conductivity, defect energy levels, formation energies and chemical origin of deep level emissions are still controversial issues. A clear understanding of the nature of native defects and their roles on dopants in ZnO is essential for successful application in practical devices.

Oxygen vacancies

Oxygen vacancies have the lowest formation energy among the native donor-like defects (Figure 2.1) and have frequently been appealed as a source of residual n-type conductivity in ZnO. But, recent studies show that oxygen vacancies are deep donors and cannot be the source of background n-type conductivity [5, 35]. The V_O^+ charge state is thermodynamically unstable for any position of the Fermi-level [36]. But, electron paramagnetic resonance (EPR) experiments identified the existence of V_O^+ in ZnO, indicating the formation of V_O^+ metastable state under electron irradiation [37]. Oxygen vacancies become neutral when the Fermi level is close to the conduction band and act as a source of compensation in p-type ZnO, while they are in 2+ charge state when the Fermi level is close to the valence band maximum (Figure 2.1). The position of the 0/2+ charge transfer level of V_O is highly controversial (Table 2.1). The position of 0/2+ level was calculated to be 0.5-0.8 eV above the valence band by several groups [38, 39], alternatively, the 0/2+ level was estimated to be 1-2 eV below the conduction band maximum by other groups [40, 41].

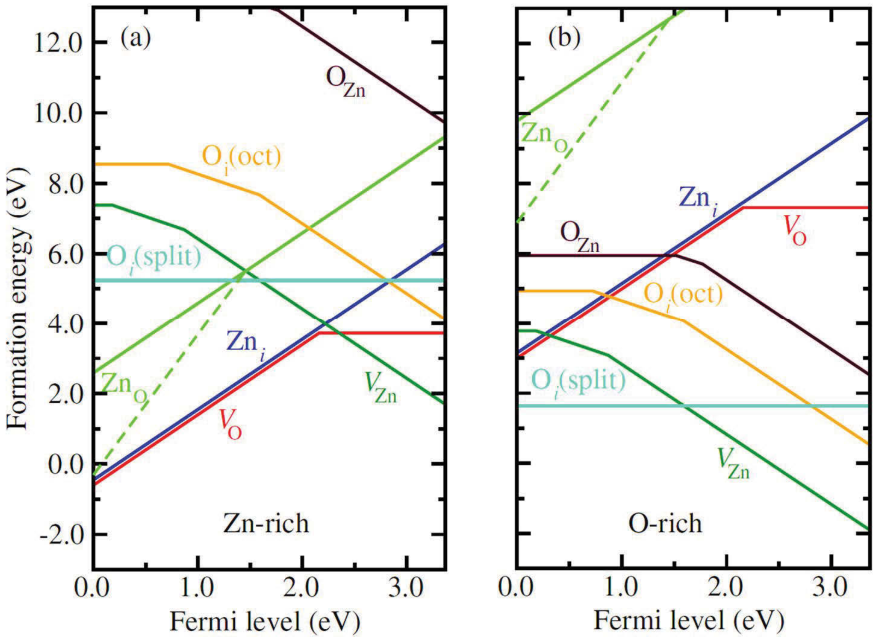

Figure 2.1. Calculated formation energies of native defects in ZnO as a function of Fermi-level for (a) Zn-rich and (b) O-rich conditions. The formation energies were obtained by local density approximation (LDA). The zero of Fermi-level indicating the valence band maximum and the slope corresponding to the charge states [35].

Oxygen vacancies show a broad green emission band as an optical signature [42-44]. The peak position of V_O-related green luminescence is highly controversial and is varied in the 2.42 – 2.54 eV energy range (Table 2.2). Ye et al. reported that the radiative recombination of an electron from the V_O^+ state to the valence band is responsible for the 2.5 eV green emission band [45], alternatively, Hofmann et al. reported that the optical excitation can convert only a fraction of V_O to V_O^+ , which is thermodynamically unstable [46]. Deep level transient spectroscopy experiments show that oxygen vacancies capture and emit always two electrons, thus 0 to 2+ transition is responsible for the green emission band in n-type ZnO [46].

Zinc vacancies

Zinc vacancies are acceptors and have high formation energy in p-type ZnO (Figure 2.1). So, the concentration of V_{Zn} is negligible in p-type ZnO. In n-type ZnO, on the other hand, zinc vacancies have lower formation energies and are present in a moderate concentration in n-type ZnO [35]. These acceptors are more favourable in the O-rich environment (Figure 2.1). Positron annihilation experiments have shown that zinc vacancies are dominant compensating acceptors in n-type ZnO [47]. The energy levels of V_{Zn} for different charge states are controversial (Table 2.1). First principle calculations find 0/1- and 1-/2- acceptor states at 180-200 meV and 870-1200 meV, respectively above the valence band maximum [35, 48]. On the other hand, the 0/1- and 1-/2- levels of V_{Zn} were calculated to be 90 meV and 1500 meV, respectively by generalised gradient approximation (GGA) [49]. EPR experiments have shown that the 1-/2- level of V_{Zn} lies 1.0 eV above the valence band maximum [50, 51].

Table 2.1: Summary of energy positions of different native defects in ZnO

Native defect	Charge state	Energy level (eV)	References
V_O	0	$E_c - 0.05$	[52]
	1+	$E_c - 2.0$, $E_c - 1.92$ $E_c - 2.24$	[52] [53] [54]
	2+	$E_c - 1.0$, $E_c - 1.1$	[36] [45]
Zn_i	0	$E_c - 0.05$	[52] [53]
	1+	$E_c - 0.5$, $E_c - 0.2$	[52] [53]
	2+	$E_c - 0.15$, $E_c - 0.08$	[40] [55]
V_{Zn}	0	$E_v + 0.3$, $E_v + 0.31$	[56, 57]
	1-	$E_v + 0.7$, $E_v + 82$,	[52] [53]
	2-	$E_v + 2.8$, $E_v + 2.91$, $E_v + 2.67$	[52] [54]
O_i	0	$E_v + 1.08$, $E_v + 0.9$	[56, 58]
	1-	$E_v + 0.38$, $E_v + 0.4$	[59] [58]
	2-	$E_v + 0.99$, $E_v + 1.43$ $E_v + 0.79$	[57] [59]

Zinc vacancies are considered as another source of green emission band in ZnO [43, 44]. The peak positions of the reported V_{Zn}-related green luminescence are found in the 2.30 – 2.53 eV energy range (Table 2.2). The electronic transition responsible for the green emission band in ZnO is a debatable subject. Different research groups suggested different types of electronic transitions to describe the green luminescence band such as from a shallow donor to deep V_{Zn} acceptor [60], from conduction band to V_{Zn} acceptor [54], from Zn_i to V_{Zn} acceptor level [61] and a hole transfer from divalent zinc vacancy (V_{Zn}^{2-}) and monovalence (V_{Zn}^{-}) defects [62]. Sekiguchi et al. also provided a strong argument in favour of zinc vacancies being the origin of green emission [63, 64]. They reported that the hydrogen plasma treatment strongly passivates the green emission band in ZnO. This observation indicates that zinc vacancies are responsible for the green emission and can be passivated by hydrogen.

Table 2.2: Summary of energy positions and assigned chemical origins of deep level emissions in ZnO.

Peak position (eV)	Emission colour	Chemical origin		References
2.5, 2.2, 2.45, 2.35, 2.48, 2.36, 2.53	Green	V_o		[43] [44] [42] [46] [65] [66] [44]
2.53, 2.35, 2.30	Green	V_{Zn}		[43] [44] [65]
2.4	Structured green			[22]
2.42, 2.45, 2.43	Structured green	Cu_{Zn}		[20] [67] [21] [68]
2.26,	Green	O_i		[65]
2.06, 2.03, 2.1	Yellow/Orange			[66] [69] [70]
1.79, 1.98, 1.95	Red			[60] [71] [72]
2.17, 1.93, 2.07	Yellow	Li_{Zn}, Li_{Zn}-related complexes	Deep state	[43] [73] [74] [75]
3.0, 3.05	DAP*, Blue		Shallow state	[74] [76] [77] [75]
1.8, 1.9	Red	$Ga_{Zn} - V_{Zn}$ and $Ga_{Zn} - O_i$		[78] [79]
~2.0-1.28	Yellow-Red, Near infrared	$Ga_{Zn} - V_o$, Ga_{Zn}-related complexes		[80] [81]

*Donor-acceptor pair

Zinc interstitials

In wurtzite ZnO structure, zinc interstitials could occupy either octahedral sites or tetrahedral sites and are more stable at the octahedral site than tetrahedral site because of their high formation energy at the tetrahedral site [48]. Among the three charge states of zinc interstitials (Zn_i^o, Zn_i^+ and Zn_i^{2+}), the most stable state is Zn_i^{2+}, which is formed by donating two electrons to the conduction band. Under equilibrium conditions, zinc interstitials have high formation energy in n-type ZnO and their concentration should be negligible [48]. So, zinc interstitials cannot be a source of the background n-type conductivity in ZnO even under Zn-rich conditions [48]. However, it has been suggested that they can be a source of n-type conductivity under non-equilibrium conditions. For examples, Hutson et al. reported the presence of Zn_i shallow donors with an activation energy of 51 meV in Hall experiments [82] and Look et al. also observed the presence of Zn_i shallow donors when ZnO samples were irradiated by high-energy electron beam [83]. The formation energy of Zn_i decreases with decreasing the Fermi energy, indicating that they act as a compensating defect in p-type ZnO [48].

Oxygen interstitials

The formation of oxygen interstitials is due to the excess of oxygen atoms in ZnO. Oxygen atoms can occupy either the octahedral interstitial site or tetrahedral interstitial site. First principle calculations suggest that the tetrahedral interstitials are unstable and can diffuse into the split-interstitial configurations, also known as dumbbell configuration [40]. Oxygen interstitials are more stable and electrically active in the octahedral interstitial site [49]. The octahedral O_i introduce $\varepsilon(-/2-)$ and $\varepsilon(0/-)$ acceptor levels at 1.59 and 0.72 eV, respectively above the valence band maximum, indicating that they are deep acceptors [5]. The octahedral O_i configurations have high formation energy and their concentration is negligible in

ZnO under equilibrium conditions. Janotti et al. reported that oxygen interstitials are electrically inactive in p-type ZnO and act as a deep acceptor when the Fermi level is greater than 2.8 eV [5].

A broad yellow emission peaking in the ~ 2.0 – 2.1 eV energy range has been reported in ZnO nanostructures (Table 2.2) [66, 70]. This yellow emission band in ZnO has been attributed to O_i defects [66, 70]. Moreover, several groups reported that the red emission centred at ~1.80 eV in ZnO nanostructures is due to O_i defects [60, 71]. The energy levels of different defects and their electronic transitions suggested by different groups are presented in the Figure 2.2.

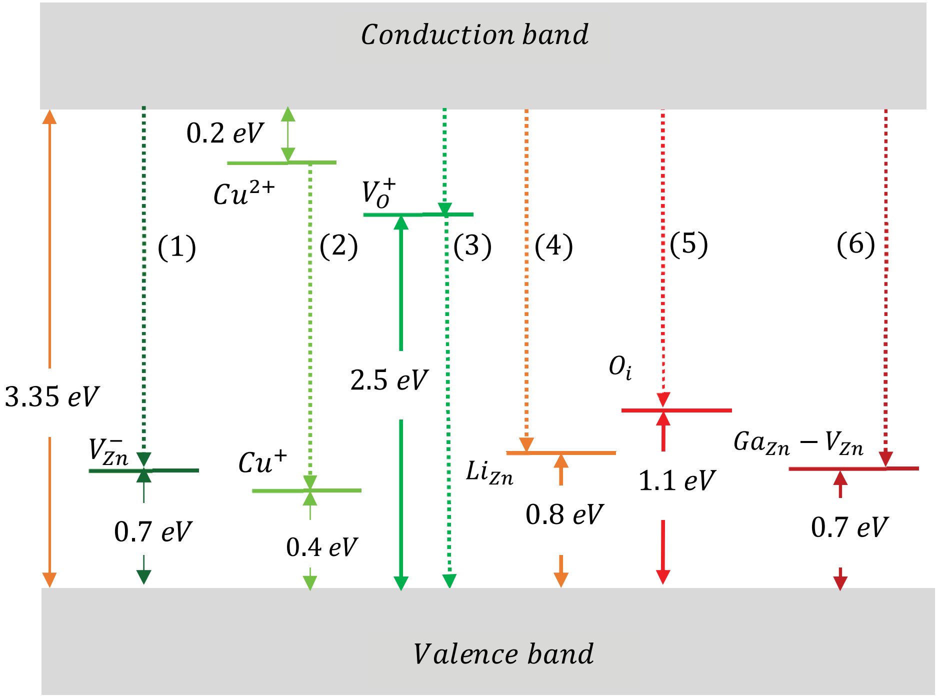

Figure 2.2. Electronic transitions of different defects in ZnO based on the Table 2.2 and the following references; (1) [84], (2) [20], (3) [45], (4) [85], (5) [72], (6) [86].

2.2. Ga-related defects

Ga atoms preferably occupy into the Zn sites and induce substitutional defects (Ga_{Zn}) in ZnO. Moreover, Ga could accommodate either octahedral interstitial site (Ga_i^O) or tetrahedral interstitial site (Ga_i^T). The formation energies of Ga_i^O and Ga_i^T are much higher than Ga_{Zn} and their concentrations are negligible in equilibrium conditions [87]. The substitutional defects act as shallow donors in ZnO and have a (+/0) thermodynamic transition level at 3.0 eV above the valence band maximum [24].

Zinc vacancies and oxygen interstitials can easily be formed in ZnO grown at O-rich conditions. Theoretical studies have shown that Ga_{Zn} donors can interact with acceptor-like defects (V_{Zn} and O_i), forming the high concentration of $Ga_{Zn} - V_{Zn}$ and $Ga_{Zn} - O_i$ defect complexes due to the Coulomb interactions between donor and acceptor [24, 88]. The local atomic geometry of $Ga_{Zn} - V_{Zn}$ and $Ga_{Zn} - O_i$ defect complexes are shown in Figure 2.3. These defects act as acceptors and are electrically active in ZnO.

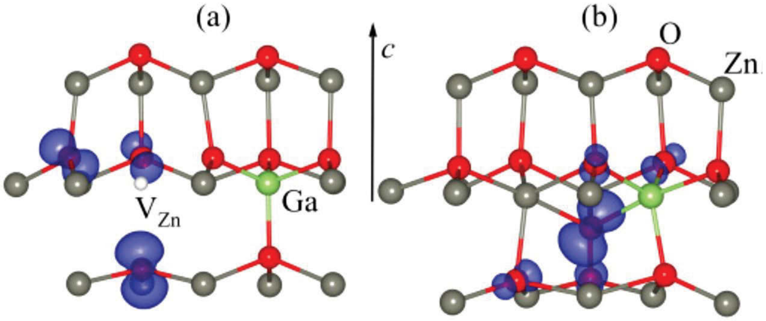

Figure 2.3. Local atomic geometry for (a) $Ga_{Zn} - V_{Zn}$ and (b) $Ga_{Zn} - O_i$ complexes in Ga-doped ZnO [24]. Both complexes acting as deep acceptors and electrically active in ZnO.

Under O-rich conditions, $Ga_{Zn} - V_{Zn}$ acceptors complexes have significantly lower formation energy than Ga_{Zn} donors below 2.8 eV Fermi energy (Figure 2.4 (a)) and are responsible for appreciable compensation. The formation energy of $Ga_{Zn} - O_i$ is higher than $Ga_{Zn} - V_{Zn}$, indicating the less contribution of $Ga_{Zn} - O_i$ in Ga-doped ZnO. In O-poor conditions, the formation energies of these defect complexes are increased by ~6.7 eV (Figure 2.4 (b)), indicating that the compensation mechanism is less pronounced. Several experimental and theoretical predictions have shown that $Ga_{Zn} - V_{Zn}$ and $Ga_{Zn} - O_i$ acceptors have binding energies of ~0.75 and ~0.66 eV, respectively above the valence band maximum [24, 78]. Yamada et el. and Tsay et al. have reported that the electrical conductivity, as well as the carrier concentration significantly decreases at high Ga doping concentration when samples were grown at O-rich conditions [89, 90].

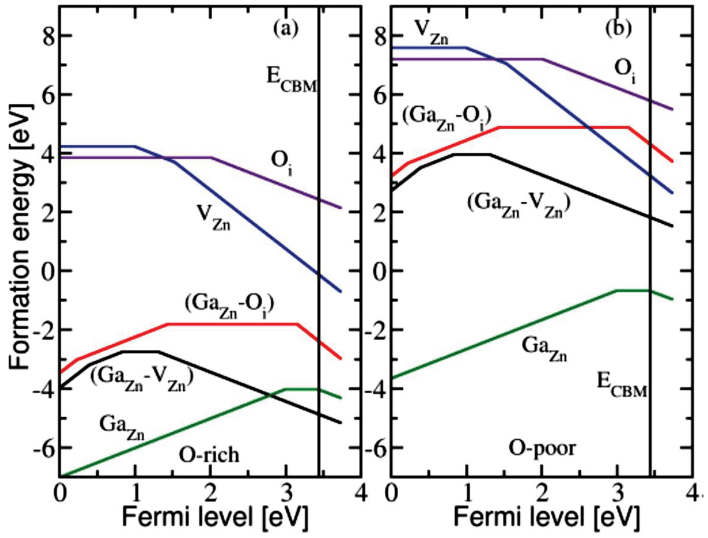

Figure 2.4. Formation energies of Ga-related defects as a function of the Fermi energy in (a) O-rich and (b) O-poor conditions. The zero value indicating the valence band maximum and slopes showing the defect charge states [24].

The optical signatures of group III elements in ZnO are highly controversial. Park et al. observed a yellow emission band around 2.0 eV in Ga-doped ZnO nanowires [91], but they cannot successfully explain the chemical origin of this emission band. A broad red emission band has been reported in Ga-doped ZnO by several research groups [79, 86] and is responsible for Ga-related acceptor complexes ($Ga_{Zn}-V_{Zn}$ and $Ga_{Zn}-O_i$). Alternatively, Jiang et al. reported that the yellow and red emissions are originated from Ga-related complexes, especially V_O-Ga_{Zn} donor complexes [80]. Zhang et at. observed the blue, green, yellow and red emissions at different Ga doping concentrations in ZnO. They reported that these emissions attributed to defects at different energy levels [29]. He et al. reported that heavily Ga-doped ZnO shows the near-infrared emission attributed to Ga_{Zn}-related complexes in ZnO [81]. As an optical signature, group III elements also show bound excitons at low temperature [23, 92, 93]. A summary for peak positions and ionisation energies of these excitons are presented in Table 2.3. Most commonly observed donor-bound excitons in ZnO are I_4 and I_6 lines at 3.3628 eV and 3.3608 eV, respectively. The I_4 line is attributed to H donors, which can easily be incorporated into ZnO nanostructures during growth. The I_6 line is due to Al donors. The I_8 and I_9 lines are attributed to Ga and In impurities, respectively. Yang et al. reported that Ga donors also show an ionised donor bound exciton (I_I) and a donor-acceptor pairs line (I_{DAP}) at ~3.321 eV in Ga-doped ZnO [94]. The chemical origin of $I_5, I_7,$ I_{10} and I_{11} lines are still unknown in ZnO. Look et al. proposed that the chemical origin of I_9 line is N-related complex [95], whereas Mayer et al. suggested that the origin I_9 is In [23].

Bandgap engineering of ZnO can be achieved by alloying with Group III elements. First principle calculations and experiments have shown that Ga donors interact with acceptor-like defects, producing the abundance of defect complexes, especially Ga_{Zn}-O_i and Ga_{Zn}-V_{Zn} pairs, which lead to the significant reduction of bandgap and carrier concentration in ZnO [24, 88]. Kim et al. reported that Ga dopants can increase the bandgap of ZnO, making it more suitable for plasmonic applications [26]. Ginting et al. reported that the bandgap of ZnO nanorwires is not significantly changed with Ga doping up to 3 at% [96]. Zhang et al. observed a remarkable decrease of ZnO bandgap with Ga doping in both the PL and EL experiments [29]. A significant decrease in the bandgap has been reported for ZnO doped with In [97], conversely, the bandgap widening for In-doped ZnO has also been reported [98]. These above results indicate that the bandgap engineering in ZnO doped with group III elements is a controversial issue.

Table 2.3. Summary of bound exciton lines, their emission energies and ionisation energies (taken from the references [23, 92, 93]).

Line	Energy position (eV)	Ionisation energy (meV)	Exciton type	Chemical origin
I_o	3.3727	53.0	D^+X	Al
I_1	3.3718	54.6	D^+X	Ga
I_2	3.3674	63.2	D^+X	In
I_3	3.3665	63.2	D^+X	In
I_4	3.3628	46.1	D^oX	H
I_5	3.3615	50.0	D^oX	-
I_6	3.3608	51.6	D^oX	Al
I_7	3.3600	54.1	D^oX	-
I_8	3.3598	54.6	D^oX	Ga
I_9	3.3567	63.2	D^oX	In
-	3.3574	20.4	A^oX	Na
I_{10}	3.3551	72.6	D^oX	-
-	3.3539	24.3	A^oX	Li
I_{11}	3.3484		D^oX	-

ZnO doped with group-III elements (Al, Ga and In) has also been recognised as low optical loss plasmonic materials [27, 99]. Several theoretical and experimental studies have shown that these materials have a low optical loss in the visible and near infrared regions compared to conventional plasmonic metals (Ag and Au) [26, 27, 99]. As shown in Figure 2.5, ZnO doped with group III elements shows a low optical loss in the visible and near infrared regions. It has also been reported that the plasma frequency can be tuned by incorporating Ga into the ZnO [26]. The high optical loss of traditional metals in the visible and infrared regions is the main limitation for the improvement of plasmonic devices. These alternative plasmonic materials have the promise to overcome this major issue and provide greater flexibility in designing of plasmonic devices with moderate magnitude of permittivity and loss factor [99].

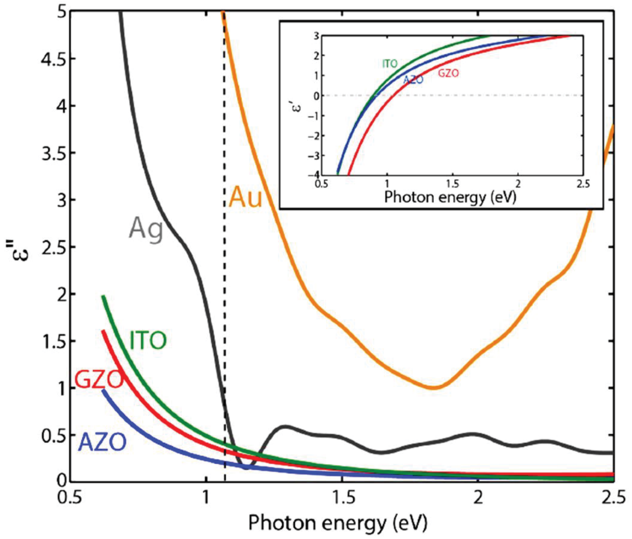

Figure 2.5. Comparison of optical loss (imaginary part of permittivity) among Al-doped ZnO (AZO), Ga-doped ZnO (GZO), In-Sn-O (ITO), Au and Ag. Oxide materials showing the low optical loss compared to the conventional metals [26].

2.3. Li-related defects

Li can easily release its valence electron and preferably occupies into Zn site (Li_{Zn}), which acts as an acceptor in ZnO. Alternatively, Li may diffuse into the interstitial site (Li_i), which behaves as a donor. Li-related pair complexes ($Li_{Zn} + Li_i$) can also be formed under O-rich conditions [9]. Figure 2.6 (a) - (b) shows the local atomic geometry of $Li_{Zn} + Li_i$ complexes [75]. In both the O-rich and Zn-rich conditions, the formation energies decrease for Li_{Zn} and increase for Li_i with increasing the Fermi level. In 100% O-rich conditions, the $Li_{Zn} + Li_i$ pair complexes have the lowest formation energies than Li_{Zn} and Li_i defects (Figure 2.6 (c)) [100]. Density function theory calculations find a (0/-) acceptor level located at ~$E_V + 0.8\ eV$ [9, 100]. EPR experiments have shown that Li has two acceptor states at 850 meV and 150 meV above the valence band maximum [101].

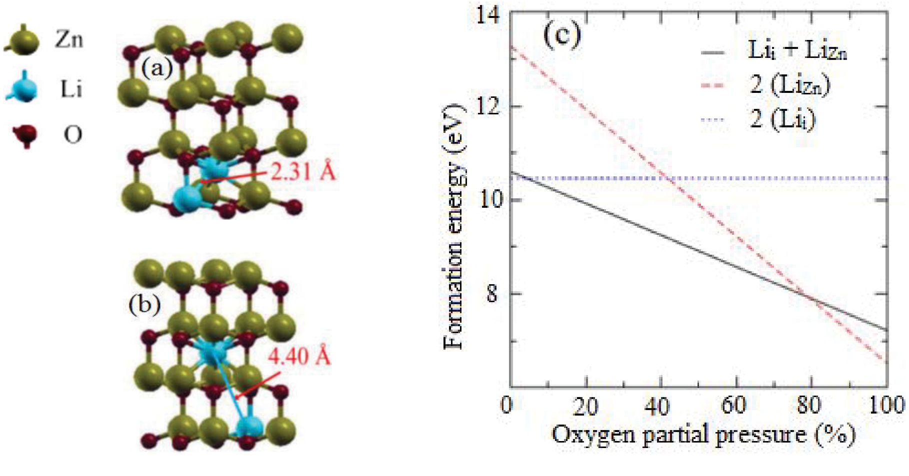

Figure 2.6. The local atomic geometry of $Li_{Zn} + Li_i$ pair complexes for (a) nearest and (b) well separated from each other [75]. (c) Formation energies of $Li_{Zn} + Li_i$ pair complexes as a function of oxygen partial pressure in 100% O-rich conditions [100].

The optical properties Li-related defects have been studied by several research groups [73, 101, 102] but is still a debatable subject. In the near-band-edge region, the low-temperature emission spectrum of Li-doped ZnO shows a bound excition line at 3.3539 eV [76, 93]. A broad yellow emission band in the ~1.9 -2.2 eV energy range is commonly observed in Li-doped ZnO (Table 2.2 of section 2.1). Several research groups have suggested that a deep Li_{Zn} acceptor level at 0.8 eV above the valence band maximum is responsible for this yellow emission band in Li-doped ZnO [73, 102]. Alternatively, Sahu et al. reported that the 2.10 eV yellow emission band has been attributed to $Li_{Zn} + Li_i$ pair complexes when the component species (Li_{Zn}, Li_i) are close to each other (Figure 2.6 (a)). Zhang et al. reported that an emission band peaking at 3.0 eV attributed to Li_{Zn} acceptor [74], while Sahu et al. reported that the $Li_{Zn} + Li_i$ pair complexes are responsible for the ~3.0 eV emission peak when the component species (Li_{Zn}, Li_i) are away from each other. Mayer et al. have also been reported an emission peak at 3.0 eV in Li-doped ZnO. They assigned this peak as a donor-acceptor pair (DAP), which is due to the Li-related shallow acceptor state [76].

2.4. Cu impurities

Cu is a common impurity in ZnO and favourably occupies substitutionally the Zn site (Cu_{Zn}), which acts as an acceptor leading to the p-type conductivity and ferromagnetism [15, 17]. Hunag et al. reported that Cu has three charge states, i.e. $Cu_{Zn}^{+}\ or\ Cu^{3+}(3d^8 4s^0)$, $Cu_{Zn}^{0}\ or\ Cu^{2+}\ (3d^9 4s^0)$ and Cu_{Zn}^{-} or $Cu^{1+}\ (3d^{10} 4s^0)$ [103]. These defects have higher formation energies than native defects of ZnO in Zn-rich conditions and have lower formation energies in O-rich conditions [103]. When Cu doping concentration increases in ZnO, the Cu^{1+} leads the p-type conductivity and the Fermi level would shift toward the conduction band until the Cu^{2+}/Cu^{1+} charge transfer level (CTL) as a result of charge neutrality [104]. First principle calculations have shown that the Cu-doped ZnO is ferromagnetic when Cu defects stay in ZnO as Cu^{3+} and Cu^{2+} charge states, while this material is found to be nonmagnetic when Cu impurities stay in ZnO as Cu^{1+} configuration [103]. The position of Cu^{2+}/Cu^{1+} (0/-) CTL is still a matter of great controversy. Wardle et al. estimate the 0/- CTL at 1.0 eV above the valence band maximum [105], while Yan et al. calculated the 0/- CTL at 0.7 eV above the valence band maximum [106]. Electrical measurements on Cu-doped ZnO reveal that the 0/- CTL lies 0.2 eV below the conduction band minimum [107]. Admittance spectroscopy and photoluminescence experiments have shown that Cu has two acceptor levels at $E_c - 0.17$ and $E_v + 0.4\ eV$ [20, 108].

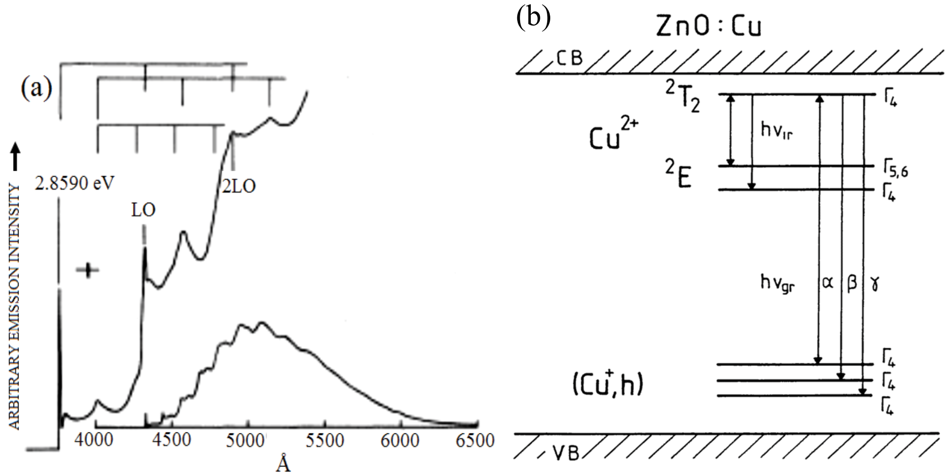

Figure 2.7. (a) Structured green luminescence band from ZnO (containing 4 ± 2 ppm Cu) at 1.6 K. The enlarge portion displaying the zero phonon line at 2.8590 eV [67]. (b) A schematic diagram of different transitions in Cu-doped ZnO in the hole representation, also displaying transition providing the α-, β- and γ-exciton lines [109].

As an optical signature, Cu impurity shows a green emission band consisting of a periodic fine structure separated by 72 meV (Figure 2.7 (a)) [20, 67] and also exhibits three excitonic emissions (also known as α-, β- and γ- zero phonon lines) originating from its three valence states (Figure 2.7 (b)) [109]. This structured green luminescence band is attributed to an internal transition of a hole within the Cu acceptors at low temperature [67]. The electronic transition that responsible for the structured green emission band is given in the Figure 2.2 of section 2.1. The energy level of Cu^{2+} state is located at 0.2 eV below the conduction and the position of Cu^{+} is 0.4 eV above the valence band maximum [20]. The Cu luminescence centres are not always optically active in the ZnO nanostructures [110]. Grace et al. and McCluskey et al. observed the structured green emission band in bulk ZnO crystals when ZnO samples were annealed at 900-1000 °C under ambient environment [68, 110]. They reported that the structured green emission band is due to the conversion of Cu^{1+} to Cu^{2+} as a result of the lowering of the Fermi level upon annealing. Reynold et al. reported that the fine structure in the green emission of ZnO is attributed to a transition of two shallow donors (30 meV and 60 meV below the conduction band) to V_{Zn} acceptors [22]. So, the fine structure in the green luminescence band depends not only on Cu impurity but also on the crystal quality of ZnO nanostructures and the position of the Fermi level. These inconsistent results highlight the fact that the nature of Cu acceptors in ZnO and its role on the optical properties is still highly controversial.

Although, the theoretical and experimental studies have shown diverse insights into the electronic structures, formation energies and energy levels of native defects and impurities in ZnO, the nature of these defects and their roles on the physical properties ZnO are still controversial issues. The rich defect chemistry of ZnO has a crucial impact on optoelectronic properties and has not yet been thoroughly investigated in the framework of novel applications.

2.5 Growth of doped ZnO nanowires and films

Doped ZnO nanostructures have been studied extensively over the past few decades not only for their exciting optical, electrical and magnetic properties but also for their future diverse technological applications. Many oxide and nitride nanostructure materials doped with various elements have been grown and characterised such as ZnO, CdO, TiO, ITO, and GaN. Among the variety of oxide nano-materials, hexagonal wurtzite ZnO has a rich family of nanostructures such as nanowires, nanorods, nanobelts, nanodiscs, nanosprings, nanosheets, nanoribons, nanofibers, nanoflowers. Among them, one-dimensional ZnO nanowires/nanorods doped with group III and group I elements have attracted a great deal of attention due to their unique physical properties, which make them potential for nanoscale optoelectronic devices. Various methods have been developed for the synthesis of doped ZnO nanostructures such as rf magnetron sputtering [111], vacuum arc plasma evaporation [112], thermal evaporation [113], metal-organic chemical vapour deposition [114], electron beam evaporation [115], sol-gel method [116], pulse laser deposition [117] and hydrothermal [118]. This section focuses on vapour phase transport and spray pyrolysis methods for the deposition doped ZnO nanostructures.

2.5.1. Vapour phase transport method

Vapour phase transport (VPT) is a widely used method for the growth of doped ZnO nanostructures. This technique is comparatively simple and cost-effective than other chemical synthesis methods. Moreover, the dimensions and alignments of nanowires can be controlled by varying growth parameters such as temperature, pressure, gas flow rate and catalysts. The mechanism of one-dimensional crystal growth was first reported by Wagner and Ellis in 1964 [119]. Figure 2.8 illustrates a schematic diagram of nanorods growth mechanism.

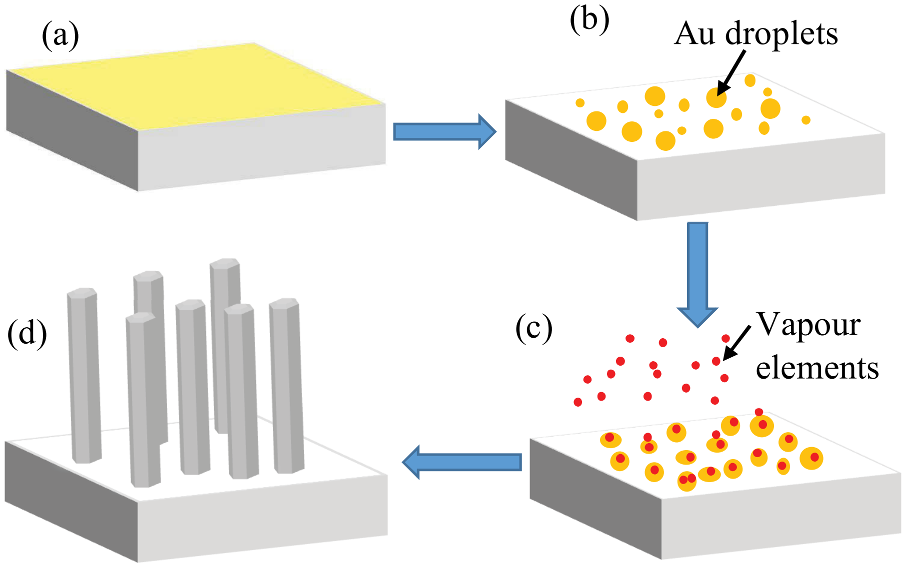

Figure 2.8. Schematic diagram of nanowires growth process. (a) Sputtering of Au catalyst. (b) The formation of Au droplets at high temperature. (c) Precursor vapour elements siting on Au droplets. (d) Grown nanorods perpendicular to the substrate.

In the VPT growth technique, the growth of nanorods occurs on stable metal catalysts such as Au, Ni, Ga, Cu, and Sn. At a high temperature above the melting point, the metal catalyst is converted into liquid alloy droplets (Figure 2.8 (b)). The formation of growth species is accomplished by the carbothermal reduction of oxide powder. The vapour phase of growth elements is transported from the source and diffused into catalyst alloy droplets (Figure 2.8 (c)). In order to obtain the minimum free energy, the growth elements will precipitate at the interface of the liquid alloy and solid substrate. One-dimensional nanorods are formed by the nucleation and crystal growth of vapour species (Figure 2.8 (d)). The diameter of nanorods depends on the size of the catalyst liquid droplets. The growth of nanorods will continue as long as the supply of the vapour phase of growth species is maintained.

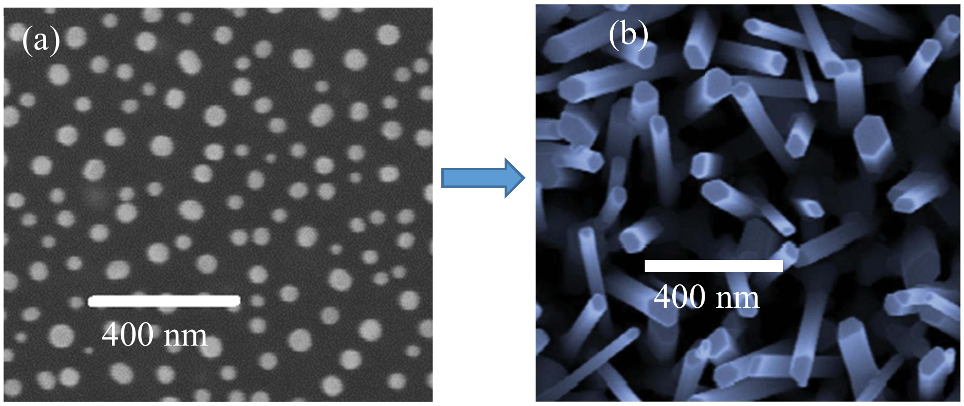

Figure 2.9. (a) SEM image of a gold-coated substrate annealed at 950 °C. (b) A typical SEM image of Ga-doped ZnO nanorods grown at 950 °C in this work.

Figure 2.9 (a) shows a typical gold coated a-plane silicon substrate annealed at 950 °C and Figure 2.9 (b) ZnO nanorods were obtained from 20 minutes of deposition time. The evaporated Zn vapour from source materials condensed and supersaturated with catalyst alloy droplets. ZnO nanorods are produced by the diffusion of supersaturated Zn species form the vapour-liquid interface to liquid-solid interface.

In the catalyst-free VPT method, the source material in vapour phase is condensed to produce various nanostructures including nanowires, [120] nanorods [121] and other complex structures [122, 123]. However, it is difficult to control the alignment, geometry, and location of nanowires without catalysts. Figure 2.10 shows some nanostructures grown by catalyst-free VPT method under certain growth conditions in this work.

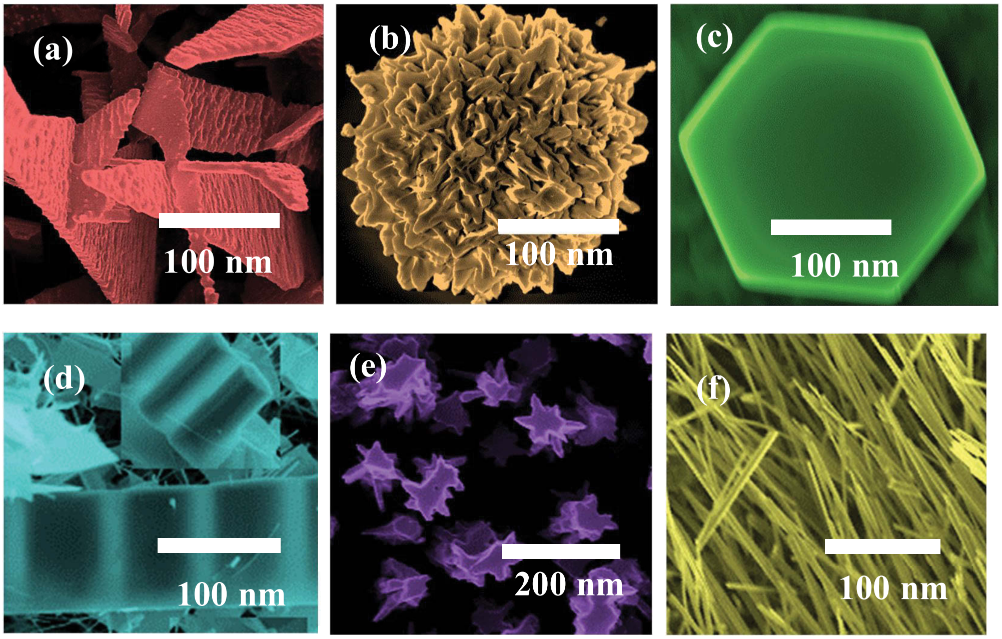

Figure 2.10. Catalyst-free various ZnO nanostructures; (a) nanosheets, (b) nanoflower, (c) nanodiscs, (d) nanoribons, (e) nanostars and (f) nanofibers grown by vapour phase transport method under various growth conditions in this work.

The self-catalytic VPT [124] is also a widely used method to grow ZnO nanowires. This method has the potential for the fabrication of ZnO nanowires without the contamination of catalytic components [125]. Before starting the self-catalyst growth of ZnO nanowires, a sputtering machine is used to deposit a thin seed layer of ZnO onto the substrate. This seed layer acts as a catalyst for growing ZnO nanowires. Figure 2.11 displays ZnO nanowires grown by a self-catalyst VPT method in this work. In this method, tapered diameter nano/microrods were produced. The tapered nanowires are not uniformly distributed on the substrate and the diameter of deposited nanowires is varied from several hundred nanometres to several micrometres along their length.

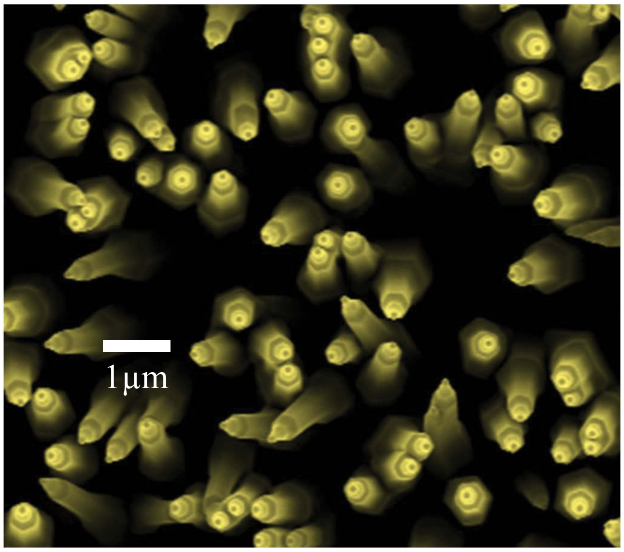

Figure 2.11. ZnO nano/microwires grown by a self-catalyst vapour method in this work. A thin seed layer of ZnO is spin coated on the Si substrate for growing ZnO nanowires.

Table 2.4. Survey on growth temperature, substrate, catalyst, carrier gases and PL emission for Ga-doped ZnO nanostructures grown by the vapour phase transport method.

Substrate	Temperature (°C)	catalysts	Ar : O_2 gases (sccm)	PL/CL peak (eV)	Ref.
GaN	1100 °C	Au	50 : 1	3.26-3.96 (UV-BL)	[29]
GaN	930 °C	Au	50 : 1	2.44 (GL), 3.23 (YL)	[91]
Si	1000 °C	Au	500 : 0	3.24 (UV)	[25]
sapphire	930 °C	Au	40 : 1	3.31-3.18 (UV)	[28]
ITO	1100 °C	-	10 : 1	3.35 (UV)	[126]
Sapphire	920 °C	GaZnO	50 : 0.2	3.35 (UV), 2.42 (GL)	[127]
Glass	600 °C	GaZnO	54 : 0.8	3.29 (UV), (GL-YL)	[128]
Si	700 °C	ZnO	200 : 30	3.26 (UV), 2.48 (GL)	[129]
Sapphire	1050 °C	ZnO	NH_3:Ar 10:80	-	[130]
Si	1100 °C	Catalyst-free	-	3.17 (UV), 2.38 (GL), 2.21 -	[131]
Glass	600 °C	ZnO	54:0.8	3.27(UV), White	[132]

The main factors that affect the growth of nanorods are temperature, catalysts, and types of substrate and carrier gases.

Growth temperature

ZnO nanorods are grown from the vapour phase of Zn atoms at a high temperature of about 950°C. The growth temperature significantly affects the dimension of ZnO nanorods. The diameter and length of ZnO nanorods decrease with increasing temperature. In the VPT method, the substrate temperature of about 700 °C is suitable for well-aligned ZnO nanorods [133]. At high temperature, the catalysts can diffuse into nanorods, leading to an increase of impurity concentration in ZnO. This impurity can degrade the optical properties of nanostructures [134, 135].

Catalysts

The most commonly used catalysts are metal nanodroplets of Au, Cu, Co and Sn for growing ZnO nanostructures. The proper selection of a catalyst is very important in this method. This is because the size of catalyst droplets determines the dimension and alignment of nanorods [125]. Among various catalysts, Au is chemically inert and easy to deposit onto the substrate and has widely been used to grow well-aligned ZnO nanorods. Recently Hung et al. and Hsu et al. fabricated vertically aligned ZnO nanowires on Ga:ZnO catalyst [127, 128].

Types of substrates

For the growth of well-aligned nanowires, the preference of substrate is also important to maintain the crystal lattice mismatch between nanorod and substrate. To grow ZnO nanorods, various kind of substrates have been used including sapphire [28], silicon [136], ZnO film [137], GaN [138], ITO [126] and ZnO coated glass [139]. Among them, Si is the most commonly used substrate in high-temperature VPT growth due to its availability and high thermal stability. From the aspect of lattice mismatch, ZnO film and GaN are better substrates to grow ZnO nanorods due to their similar crystal structure and lattice parameters. Moreover, the production of p-type GaN and p-type Si are much easier than p-type ZnO. The p-type GaN and Si substrates are preferred for the fabrication of ZnO nanorod-based optoelectronic devices.

Carrier gases

The standard gases used for growing ZnO nanorods in the VPT method are argon, oxygen and nitrogen (Table 2.4). The rate of nitrogen flow remarkably influences the morphology and optical properties of ZnO nanorods [133]. The diameter of ZnO nanorods was found to decrease with increasing N_2 gas flow rate [133]. The nitrogen gas flow can also change defect structure in ZnO nanorods [140]. The oxygen gas flow rate has a strong effect on the structural properties of ZnO nanorods [141]. Yang et al. reported that the oxygen-related defects in ZnO nanorods arise due to the presence of oxygen gas during growth [142].

2.5.2. Spray pyrolysis method

Spray pyrolysis is a simple cost-effective technique among the solution-based synthesis methods for the synthesis of ZnO nanostructures. This technique has some advantages including ease of handling, safety, cost-effective, high growth rates and large area deposition. Moreover, it is easy to produce doped ZnO nanostructures with precise physical properties. The spray pyrolysis is a widely used method for the deposition of thin films.

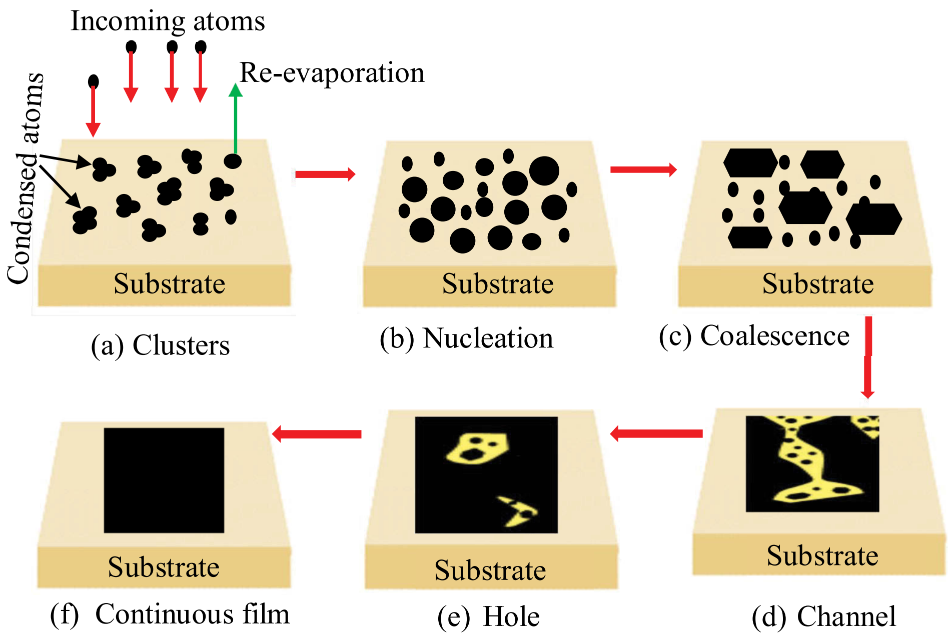

Figure 2.12. Schematic diagram for different stages of thin film growth.

In the spray pyrolysis method, thin films are grown by spraying the solution of deposited materials onto a hot substrate. In this method, three-dimensional island films are formed by different stages such as condensation, nucleation and crystal growth [143, 144]. In the condensation process, the incoming atoms interact with the substrate surface either elastically or inelastically. Some atoms collide with the substrate surface and attach elastically. The rest of the atoms lose their kinetic energy by striking the substrate inelastically and become thermally stable with the substrate. An atom adsorbed by the substrate surface is typically known as adatom. The adatoms interact with other adatoms on the substrate surface to form a cluster of atoms by collision and some atoms evaporate from the substrate surface (Figure 2.12 (a)). In the nucleation process, two or more clusters are combined to form nuclei (Figure 2.12 (b)). Volmer and Becker successfully explained the nucleation mechanism of thin film growth [145, 146]. Due to the rapid increase of nuclei, they convert to irregular hexagons or spheres also known as coalescences and cover the substrate (Figure 2.12 (c)). In channel and hole stages, the secondary nuclei began to grow to fill up the void space in the film (Figure 2.12 (d)-(e)). The continuous film is produced by the filling of channels and holes with secondary coalescences (Figure 2.12 (f)). Pashley et al. successfully explained the different stages (coalescence, channel and crystal growth) of thin film growth [144, 147]. The ideal films are free from gaps or voids. It is difficult to grow the ideal films in practical deposition methods. Normally, the films do not get enough time for crystallisation during the growth. The post-growth annealing is used to recrystallize the films. The suitable annealing environment causes the diffusion and migration of host atoms to produce the crystallise film.

The main growth parameters that affect the deposition of a film in the spray pyrolysis method are substrate temperature, deposition time and annealing temperature. The substrate temperature used in the spray pyrolysis method is in the range of 200 – 500 °C. The substrate temperature controls the movement of incoming atoms on the substrate surface. Higher movement of atoms leads to the formation of crystalline films while lower movement of atoms results in amorphous films. The electrical resistivity of the pyrolytic film was found to increase above 400 °C substrate temperature [148]. The optical and electrical properties of ZnO films largely depends on the thickness of the film. The thickness can be varied by changing the deposition time. Rao et al. reported that the electrical conductivity increases while the transparency decreases with increasing film thickness [149]. ZnO films grown at low substrate temperature show poor crystal quality. To improve the morphology and physical properties of ZnO films, post-growth treatment has been adopted in different annealing environments such as air [150], argon [150], and oxygen [151] environments. Hydrogen [152], oxygen [153] and nitrogen [154] plasma treatments have also been performed on ZnO films. Different post-growth treatments have been performed for different purposes. For example, the hydrogen plasma treatment significantly increases the carrier density and also enhances the efficiency of ultraviolet emission [152].

2.6. Light emitting devices based on doped ZnO

ZnO-based homojunction LEDs are less common compared to heterojunction LEDs due to the difficulty in realising stable p-type ZnO. Various dopants have been used to obtain doped ZnO-based p-n homojunction LEDs. For example, Chu et al. reported ZnO-based homojunction LEDs on ZnO films doped with p-type Sb and n-type Ga fabricated by standard photolithography techniques [155]. They reported that the p-type is evident from the rectifying behaviour of I-V curve (Figure 2.13 (a)) and the EL spectra show weak near-band-edge emission with a broad red emission at room temperature (Figure 2.13 (b)). However, they were not able to confirm the p-type conductivity using Hall measurements. Another ZnO films-based homojunction (p-type Sb-doped ZnO/n-type Ga-doped ZnO) using molecular beam epitaxy was reported by Yang et al. (Figure 2.14 (a)) [156]. The current-voltage characteristics (Figure 2.14 (b)) showed rectifying behaviour with high shunt resistance of about 161 kΩ and turn on voltages of 6V. The EL spectra of the device, Figure 2.14 (c), exhibited ultraviolet emission with heat-induced redshift. While several p-type ZnO based homojunction LEDs have been reported, comprehensive studies to improve the understanding of ZnO-based homojunction LEDs are limited.

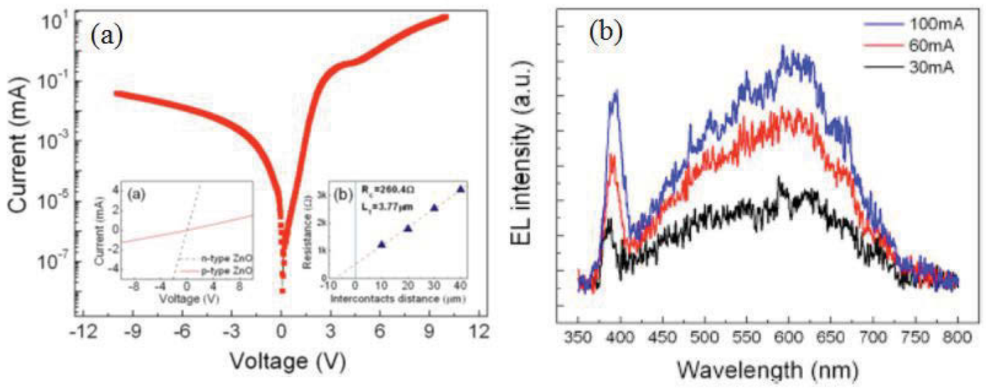

Figure 2.13. (a) Current-voltage characteristics and (b) room temperature EL spectra at different currents of p-type Sb-doped ZnO/n-type Ga-doped ZnO homojunction [155].

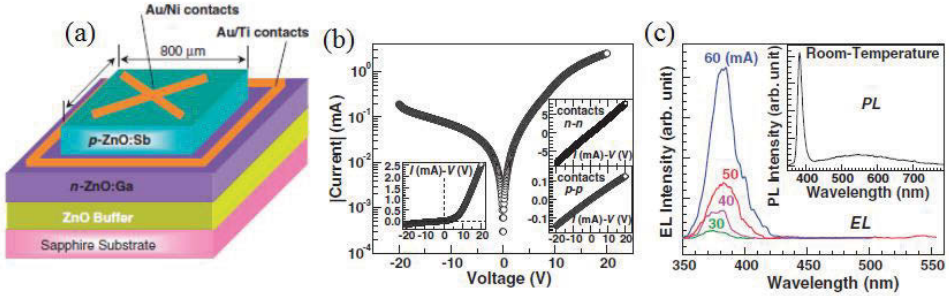

Figure 2.14. (a) Schematic of LDE structure, (b) current-voltage characteristics and (c) room temperature EL spectra at different currents of p-type Sb-doped ZnO/n-type Ga-doped ZnO homojunction [156].

In the upcoming digital and multimedia age, efficient visible colour light emitting devices have drawn much attention due to meet the requirement of high brightness mobile appliance and displays. ZnO can be a potential candidate for efficient multicolour light emitting diodes in the visible region since its various point defects act as sources of different visible emissions. Table 2.5 shows that the visible emission colours from different Ga-doped ZnO-based LEDs are different. In most of the devices, the near-band-edge is absent in EL spectra and the native point defects play a dominant role on the luminescence properties of LED devices. These LEDs also show the inconsistency between EL and PL emission peaks. Recently, experimental observation of tunable electroluminescence in the visible emission (green to red) was reported in an individual micrometre-sized Ga-doped ZnO rod (Figure 2.15) [80]. The light is emitted under high Joule heating conditions, which is not stable. This Ga-doped ZnO microrod-based EL device was reported to have a questionable high injected current of 96 mA from a single micrometre-sized rod. The exact Ga doping concentration in these devices is ambiguous. ZnO-based LEDs with improved light extraction efficiency in the visible and ultraviolet regions are still required.

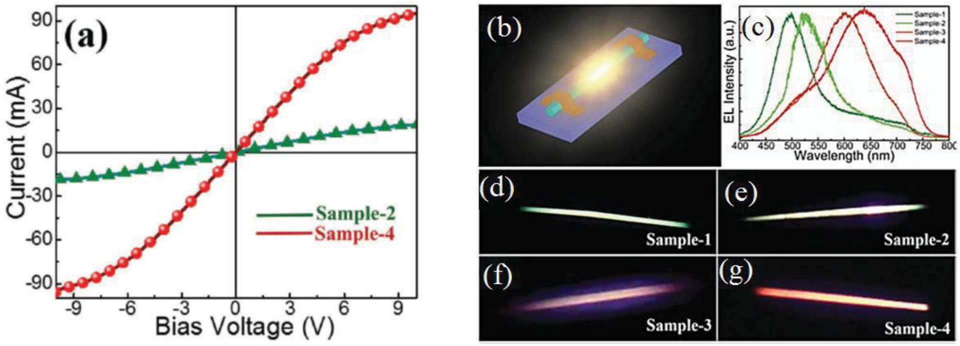

Figure 2.15. (a) I-V characteristics, (b) EL device structure, (c) tunable EL emission and (d) – (g) photographs of EL emissions of a single Ga-doped ZnO microrod-based EL devices [80]. The weight ratio of ZnO:Ga_2O_3:C in the source materials are 10:1:11 (sample-1), 9:1:10 (sample-2), 8:1:9 (sample-3) and 5:1:6 (sample-4).

Table 2.5. Survey on emission colours and fabrication methods for Ga-doped ZnO-based heterojunction light emitting devices.

LED structure	Fabrication method	Emission colour		Ref.
		PL peak (eV)	EL peak (eV)	
n-GaZnO NRs/p-Si (2 at% Ga)	Hydrothermal	3.26 (UV) 2.17 (YL)	_	[157]
n-GaZnO NRs/p-GaN (2 at% Ga)	Hydrothermal	3.22 (UV) 2.0 (GL)	2.38 (GL)	[158]
n-Ga$_x$Zn$_{1-x}$O NWs/p-GaN (0< x <0.66)	VPT	3.2-2.9 (UV-BL)	3.29-2.6 (UV-BL)	[29]
n-GaZnO MWs/p-GaN _	CVD	3.17-3.35 (UV)	3.35-3.2 (UV)	[159]
n-GaZnO NWs/p-GaN (1.12 at% Ga)	MOCVD	3.23 (UV) 2.48 (GL)	2.48-2.06 (white)	[138]
n-GaZnO NWs/p-SbZnO _	MBE	3.25 (UV) 2.38 (GL)	3.24 (UV) 2.05 (YL)	[155]
n-GaZnO film/i-ZnO/p-Si (1 at% Ga)	CVD	3.34 (UV) 3.06 (YL)	2.48-1.7 (GL-YL)	[160]
n-GaZnO NWs/p-Si (1 at% Ga)	Hydrothermal	3.26 (UV) 2.15 (YL)	_	[161]
n-GaZnO film/SiO$_2$/p-Si (1 at% Ga)	Magnetron sputtering	3.31 (UV) 3.06 (YL)	2.6-2.06 (OL-white)	[162]
n-GaZnO NWs/p-Si (80 wt% Ga)	Hydrothermal	3.26 (UV) 2.48 (GL)	2.55 (GL), 2.13 (YL), 1.85 (RL)	[129]
n-GaZnO NWs/p-GaN (8.1 at% Ga)	Hydrothermal	3.26 (UV) 2.0 (YL)	_	[163]

The large exciton binding energy (60 meV) of ZnO can allow the efficient excitonic emission in the ultraviolet region. Group III elements can be the effective n-type dopants for the carrier-mediated tuning of excitonic emission in ZnO to fabricate efficient UV and blue light emitting devices. For example, colour-tunable LED in the UV-blue region based on Ga-doped ZnO nanowire arrays was reported by Zhang et al. [29]. The Ga-doped ZnO nanowire arrays were grown by a vapour phase transport method on p-type GaN, and the gaps between the nanowires were filled with the insulating poly (methyl methacrylate) (PMMA) to fabricate the devices (Figure 2.16 (a)) [29]. The devices exhibited an increasing trend of the forward current with Ga doping (Figure 2.16 (b)) and displayed multicolour (UV to red) emissions, which was tuned by varying Ga concentration in ZnO nanowires (Figure 2.16 (c)) [29]. Another colour-tunable LED in the UV region based on an individual Ga-doped ZnO microrod was reported (Figure 2.17) [159]. The device was fabricated by spin coating of PMMA on the p-GaN followed by transferring a microrod across the boundary between PMMA and p-GaN [159]. The device exhibited almost similar current-voltage characteristics as reported by Zhang et al. but different light emission behaviour with Ga doping [159].

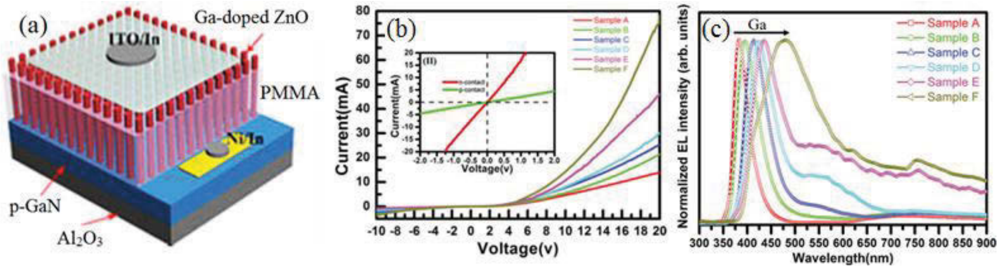

Figure 2.16. (a) LED structure, (b) I-V characteristics and (c) tunable EL emission of $Ga_xZn_{1-x}O$ nanowires/p-GaN LEDs [29]. Sample A ($x = 0$), B ($x = 0.04$), C ($x = 0.13$), D ($x = 0.28$), E ($x = 0.44$), F ($x = 0.66$).

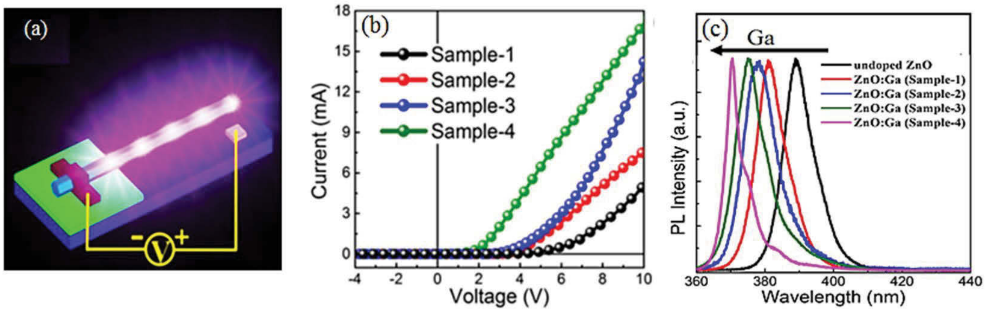

Figure 2.17. (a) LED structure, (b) I-V characteristics and (c) tunable EL emission of an individual Ga:ZnO microrod/p-GaN LEDs [159]. The weight ratio of ZnO:Ga_2O_3:C in the source materials are 10:1:11 (sample-1), 9:1:10 (sample-2), 8:1:9 (sample-3) and 7:1:8 (sample-4).

ZnO-based heterojunction LEDs are most common. Variety of materials have been used as p-type layers to fabricate ZnO-based heterojunction LEDs. For example, electroluminescence was reported for p-Si/Ga-doped ZnO nanowires [129]. Ga-doped ZnO nanowires were grown by hydrothermal technique on ZnO thin film seed layer of 400 nm. The devices exhibited traditional rectifying behaviour with high turn-on voltage of 15 V and displayed green emission (Figure 2.18 (a)-(b)), but the emission was nonuniform, as shown in Figure 2.18 (c). A p-type PEDOT was used to fabricate p-PEDOT/n-Ga-doped ZnO nanorods LED device, which exhibited an improvement of the forward current with a low turn-on voltage of 10 V and displayed the white light emission (Figure 2.18 (d) - (e)) [129]. Similar white light emission but a different turn-on voltage of 1 volt were reported in p-GaN/n-Ga-doped ZnO nanowires junction fabricated by MOCVD [138]. An orange-white light emission LEDs based on Ga-doped ZnO films/p-Si was reported, but the emission was nonuniform and weak (Figure 2.19 (a)-(b)). A SiO_2 current blocking layer between the p-Si and n-Ga:ZnO significantly improves the light extraction efficiency, despite the decreased series resistance (Figure 2.19 (b-c)).

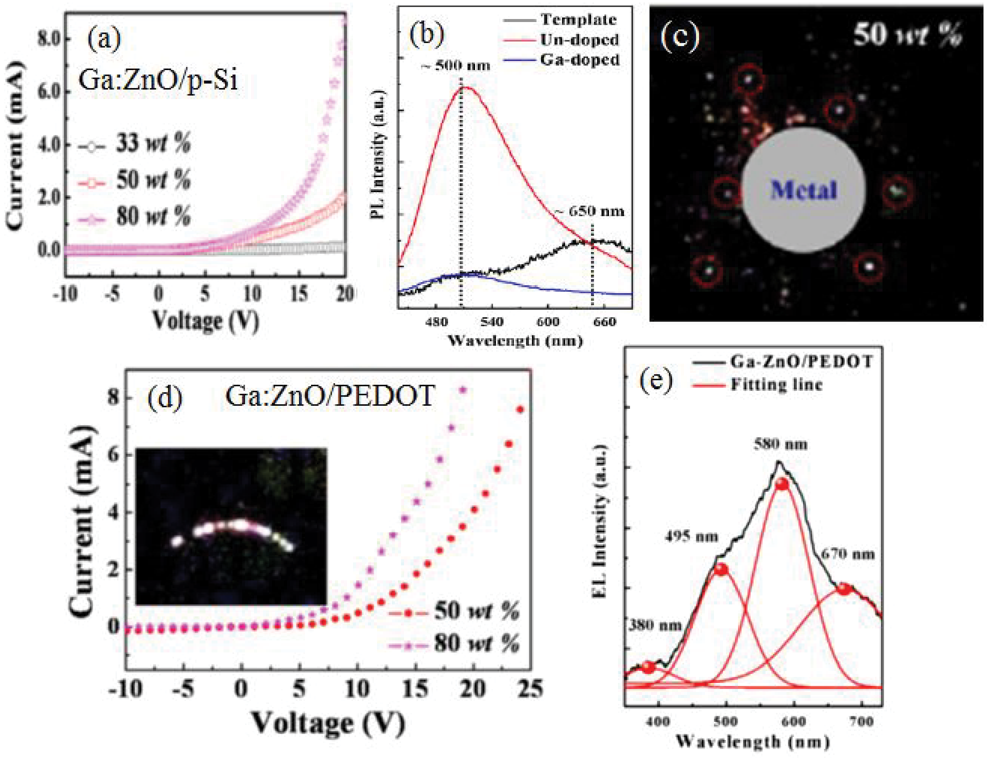

Figure 2.18. (a) Current-voltage characteristics, (b) PL spectra showing green emission and (c) photograph of Ga-doped ZnO nanowires/p-Si LEDs. (d) current-voltage characteristics showing the decrease of turn-on voltage for n-Ga-doped ZnO nanowires/p-PEDOT and (e) EL emission from the n-Ga-doped ZnO nanowires/p-PEDOT LED.

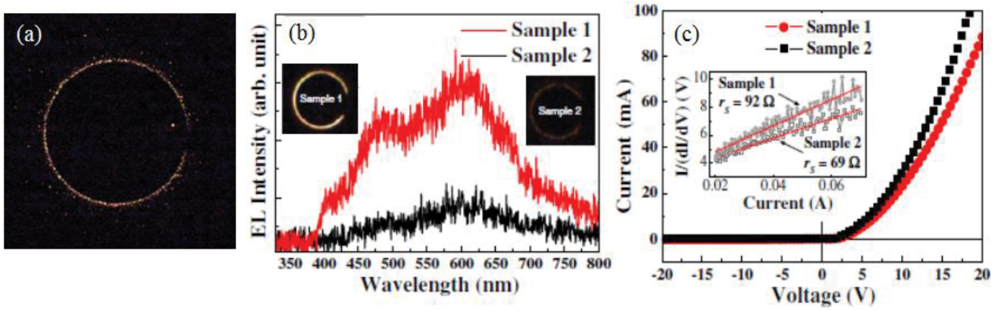

Figure 2.19. (a) Photograph of EL emission, (b) EL spectra and (c) current-voltage characteristics of n-Ga-doped ZnO/SiO$_2$/p-Si heterojunction.

A variety of heterojunction LED devices have been fabricated based on doped ZnO nanostructures (films, nanowires, nanorods, microrods), but their current-voltage characteristics and light emission colours were different. Different turn-on voltages and different emission colours are often obtained from the LED made with the same material, this is evidently a key issue in understanding the properties of LED devices based on doped ZnO nanostructures and their optimisation to achieve desired performance. One of the major problems with nanowire/nanorod-based LEDs is that some nanowires were partially covered by PMMA, resulting in the junction current non-uniformity and thus partially non-uniform electroluminescence. Another problem is that the light emission is due to the thermal heating effect in the junction. However, nanowires-based LED devices show higher light emission efficiency compared to thin films as they can act as waveguides in LED devices [32]. Comprehensive studies on the properties of doped ZnO nanostructures and their connection with the LED performance (including the role of dopants on the native defects and interfaces) are still needed.

Chapter 3

Experimental details

This chapter describes the major experimental techniques employed in this project. These techniques have been employed to grow and characterise oxide nanostructures as well as nanorod-based devices.

3.1. Spray pyrolysis method

Spray pyrolysis is one of the flexible and cost-effective deposition methods for the synthesis of high-quality ZnO thin films. This technique involves the spraying aqueous solution of desired materials onto a hot substrate in air environment. The single crystalline films are normally produced on the hot substrate by the decomposition process. The growth parameters (such as temperature, spray rate, source to substrate distance and deposition time) are crucial for the deposition of films. The main parts of this method are shadow mask, heater, spray nozzle, compressor and fume chamber.

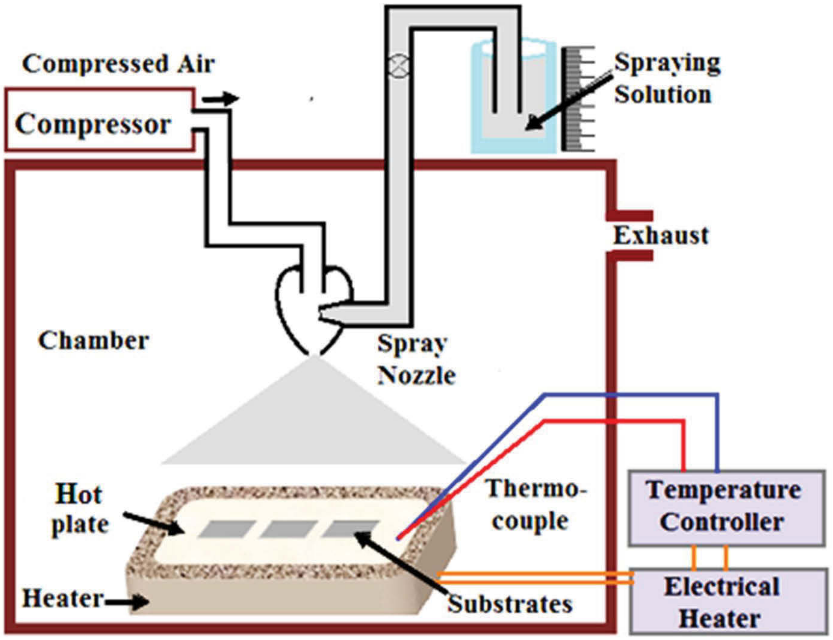

Figure 3.1. Schematic diagram for the experimental setup of spray pyrolysis technique.

A thin film of specific size and shape was obtained by preparing the specific pattern of shadow mask made of stainless steel. A mica sheet was cut as the same design of the mask and was placed between the substrate and mask to stop the spreading of the solution beyond the mask. The temperature of the hot plate was determined by a standard copper-constantan thermocouple attached to the plate. A capillary tube of the small bore was used to produce fine spray particles. A calibration chart was used to control the thickness of the film. This chart was obtained by plotting the deposition time as a function of film thickness before the synthesis of a sample.

3.1.1. Synthesis of Li-doped ZnO thin films

Microscopic glass slides were used to grow Li-doped ZnO films in this project. The substrate cleaning process depends on the nature of substrate. The glass substrate was cleaned ultrasonically using aqueous solution of sodium carbonate, nitric acid, acetone, isopropanol and deionized water, followed by nitrogen blow-dry. Pure ZnO and Li-doped ZnO thin films were grown by the spray pyrolysis technique at 1.5 mL/minute spray rate onto the glass substrate, which was kept 400°C. High purity (99.99%) $Zn(CH_3COO)_2.H_2O$ and $LiNO_3$ were diluted in methanol and distilled water at (1:1) ratio to form the 1.5M spray pyrolysis solution, which had stepwise Li doping concentrations of 0 to 4 at%. $Zn(CH_3COO)_2.H_2O$ and $LiNO_3$ are Zn and Li volatile precursors, which upon heating at 400°C decomposes to form Li-doped ZnO solid films. The chemical reactions for the deposition of pure and Li-doped ZnO films can be expressed as follows [164]:

$$\mathrm{Zn(COOCH_3)_2.H_2O} \xRightarrow{400\ ^\circ\mathrm{C}} \mathrm{ZnO} + 2\mathrm{CO_2(g)} \uparrow + 2\mathrm{CH_4(g)} \uparrow$$

$$\mathrm{Zn(COOCH_3)_2.H_2O} + \mathrm{LiNO_3} \xRightarrow{400\ ^\circ\mathrm{C}} \mathrm{ZnO{:}\,Li} + \mathrm{NO\ (g)} \uparrow + 2\mathrm{CO_2}$$
$$\uparrow + 2\mathrm{CH_4(g)}\ + 2\mathrm{O_2(g)} \uparrow$$

The thermal decomposition of fine droplet (aerosols) takes place in the close proximity to the heated substrate.

The schematic of spray pyrolysis method is shown in Figure 3.1. A suitable amount of spray solution (100 ml) was taken in a beaker. The cleaned substrate was put on the stainless-steel plate. The separation between substrate and nozzle head was maintained at 20 cm. Before starting deposition, the temperature of the hot plate was maintained at 400 °C for 10 minutes to obtain the similar temperature of the hot plate and substrate. The spray rate was maintained at 1.5 ml/minute. ZnO films of ~ 250 nm thickness were obtained for the growth time of 30 minutes.

3.1.2 Thin film thickness measurement

The thickness of the film was measured using the Newton's ring interference method. In this method, a plano-convex lens of radius R is used to produce interference patterns in the interface between the film and lens. Figure 3.2 illustrates the experimental arrangement for the determination of film thickness.

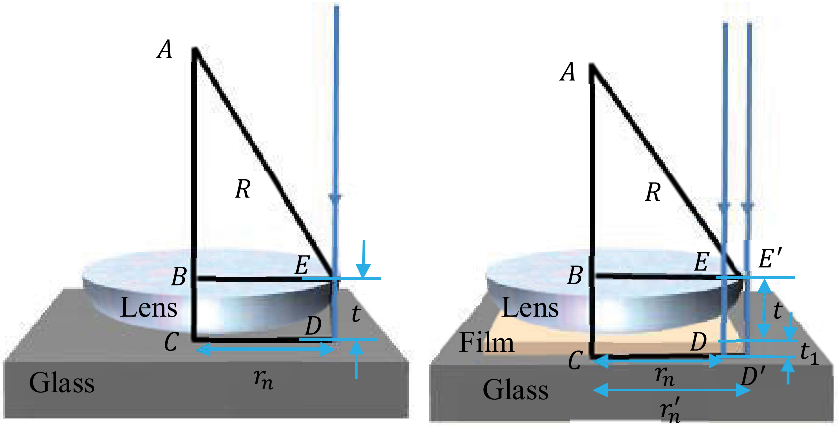

(a) (b)

Figure 3.2. Schematic diagram for the determination of film thickness. The film thickness was measured by producing the interference patterns between: (a) glass and lens and (b) film and lens.

If r_n $(= BE)$ be the radius of an interference pattern at point D and t $(= DE)$ be the thickness of the air film, it can be written from Figure 3.2 (a) as:

$$AE^2 = AB^2 + BE^2 = (AC - BC)^2 + CD^2 \Longrightarrow R^2 = (R - t)^2 + r_n^2 \tag{3.1}$$

By neglecting the t^2 term as the t is very small

$$t = \frac{r_n^2}{2R} \tag{3.2}$$

Now a film of thickness, t_1, was placed in between the lens and glass. So, the thickness of the air film was increased by t_1. It can be written form Figure 3.2 (b) as:

$$t_1 = \frac{r_n'^2 - r_n^2}{2R} \tag{3.3}$$

The value of t_1 was measured by measuring the radius of the nth Newton's ring and the radius curvature of the lens. An optical microscope was used for these measurements.

3.2. Vapour phase transport method

Vapour phase transport (VPT) is one of the most versatile methods for growing nano/microrods. This is a high-temperature method. The growth of nanostructures occurs from the vapour phase of the deposited material. So, the growth temperature depends on the vapour temperature of the deposited material. The main parts of the VPT method are furnace, quartz tube, rotatory pump, pressure gauge, gas controller system, stand and clamp, LabVIEW software, alumina boats and Type-T (copper-constantan) thermocouple.

A Lindberg/Blue M^{TM} 1100°C tube furnace was used in VPT method. The schematic of the vapour phase transport method is illustrated in Figure 3.3. The temperature range of this furnace is 30 - 1100 °C. This is a programmable single heating zone furnace made of nichrome wire coil of length 20 cm. The temperature ramp (up and down) and growth time were computer controlled. Two separate alumina boats were used to maintain the source material and substrate. A movable clamp holding the quartz tube was used to push the substrate and source materials inside the furnace. A rotatory pump was used to control the pressure inside the tube. To measure the pressure inside the tube, a pressure gauge was connected to the tube. Carrier gasses were controlled by a computer-controlled LabVIEW software.

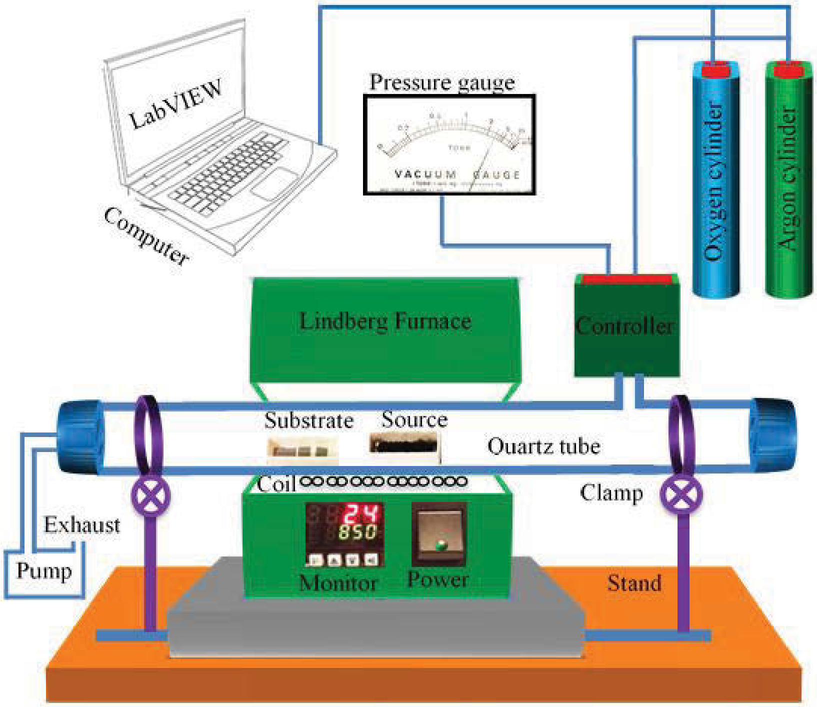

Figure 3.3. Schematic diagram of the vapour phase transport method.

3.2.1. Advantages of the VPT method

The VPT technique is one of the best methods for growing nanorods and has several advantages compared to other growth techniques.

1. A simple cost-effective nanowires growth technique capable to grow large area nanorod arrays sample up to 2 × 2 cm^2. The nanorods are uniformly distributed on the substrate.
2. The growth nanorods in this method are single crystalline, well aligned and perpendicular to the substrate.
3. The diameter and the length of nanorods can be easily controlled in this method. By varying the growth parameters, the diameter of the rod can be varied from 20 nm to 20 μm and length from 1 μm to 100 μm.
4. The doping concentration in the nano/microrods can be controlled by varying the ratio of source materials.
5. As VPT technique producing the large-area sample, this method can allow the fabrication of large-area optoelectronic devices.

3.2.2. Growth of Ga-doped ZnO nano/microrods

The a-plane silicon wafers and the sapphire substrates were used to grow undoped and Ga-doped ZnO nanorods. The Si substrate was cleaned ultrasonically using acetone, isopropanol and deionized water, followed by nitrogen blow-dry. A thin (3-5 nm) gold layer was coated onto the substrate using a Leica EM ACE600 sputtering machine (Figure 3.4). High purity (99.99%, Sigma Aldrich) powder of ZnO, Ga_2O_3 and graphite (0.25:0.75:1) was mixed in a glass bowl. The pressure inside the tube was set at 0.1 Torr by a rotatory pump. The source material was heated at 950°C under a constant flow of Ar/O_2 (20:6) gas during growth. Zn and Ga vapours were produced through the carbothermal reduction of ZnO and Ga_2O_3 powders and then reoxidised by oxygen gas to promote the fabrication of Ga-doped ZnO nanorods. Figure 3.5 shows the photograph of each step for the growth of nanorods. Different Ga concentrations in nanorods were achieved by adding different amounts of Ga_2O_3 powder to the source material with concentrations up to 1.4 at%. The Ga_2O_3 powder undergoes the following reactions inside the furnace at high temperature [165, 166]:

$$Ga_2O_3 + 2C \rightarrow Ga_2O + 2CO$$

$$Ga_2O_3 \rightleftharpoons Ga_2O + 2O_2$$

where Ga_2O is a volatile metal oxide. The Ga_2O vapour can be easily transported to the deposition zone by the carrier gas (Ar) and react with CO as [167]:

$$Ga_2O + CO \rightarrow 2Ga + CO_2$$

The Zn metal particles are produced by the following reactions [168]:

$ZnO + C \rightarrow Zn + CO$ and

$ZnO + CO \rightarrow Zn + CO_2$

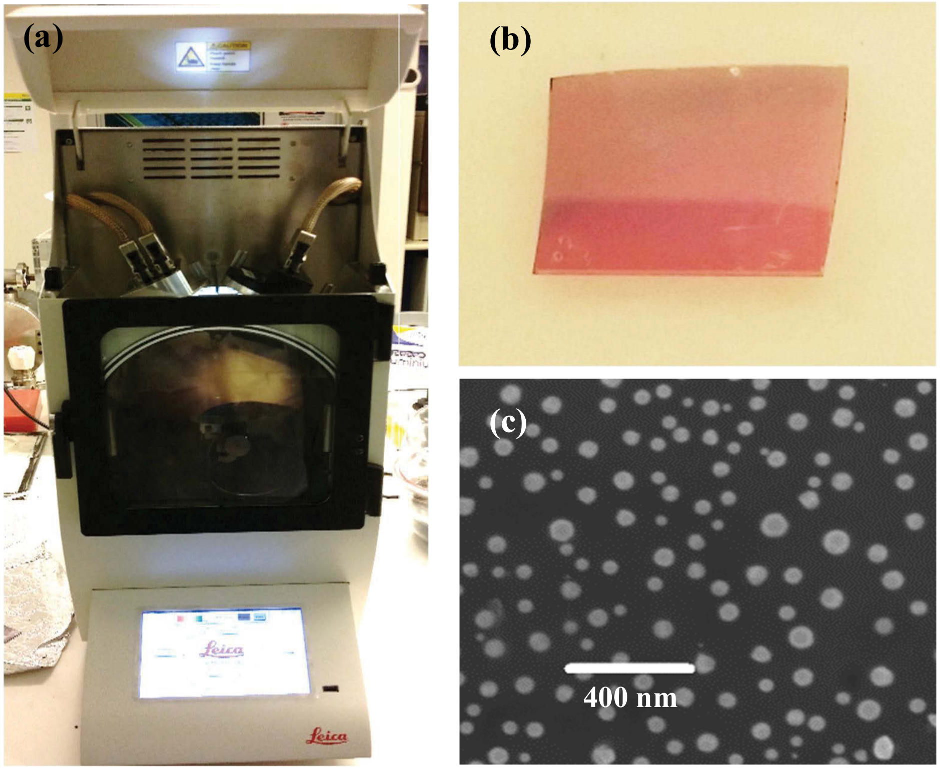

Figure 3.4. (a) Photograph of a Leica EM ACE600 sputtering machine. This is a simple programmable sputtering machine in which the sputtering parameters can be adjusted by a simple program. The sputtering parameters used in this experiment were chamber pressure (= 1.5 x 10^{-5} mbar), current (= 15 mA), the substrate-target distance (= 3 mm), Ar pressure (= 9 x10^{-3} mbar). (b) Photograph of a gold coated sapphire substrate. (c) SEM image of Au coated substrate annealed at 950 ^{o}C showing Au droplets of size ranging from 20 to 60 nm.

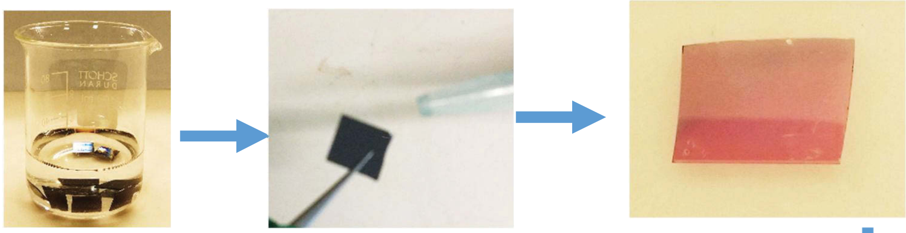

(a) Cleaning

(b) N_2 blow dry

(c) Au coating

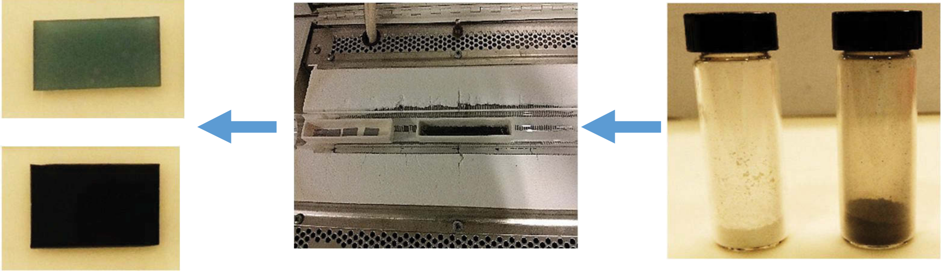

(f) As grown samples

(e) Substrates and source materials in the furnace

(d) Powder mixture

Figure 3.5. Photographs of different stages for the growth of Ga-doped ZnO nanorods. (a) Substrate cleaning ultrasonically using acetone, isopropanol and deionised water. (b) Nitrogen blow-dries. (c) Au coated sapphire substrate. (d) Mixed powder of ZnO and Ga_2O_3 with graphite (Grey colour) and without graphite (white colour). (e) Two separate alumina boats containing the substrate and source materials in the furnace. (e) Grey (on the sapphire substrate) and black (on the silicon substrate) colours Ga-doped ZnO nanorods samples.

To grow undoped and Ga-doped ZnO microrods, a self-catalyst VPT was used. High purity (99.99%) $Zn(CH_3COO)_2.H_2O$ was diluted in methanol and deionised water at (1:1) ratio to form the catalyst solution. A spin coater was used to deposit a thin layer of ZnO on the Si substrate. A short time (10 minutes) annealing produce the fine particles of ZnO catalyst on the Si substrate. These particles of ZnO act as a catalyst for the growth of nano/microrods. The ZnO coated Si substrate was placed on the top of an alumina boat containing premixed powder. At 1000 ºC, the quartz tube with source material was pushed at the centre of the furnace and was maintained at a constant temperature of 1050 °C for 5 minutes at the oxygen-rich environment and then quickly removed from the furnace. Zn and Ga vapours were produced through the carbothermal reduction of ZnO and Ga_2O_3 and then reoxidised by the oxygen gas to assist the fabrication of Ga-doped ZnO microrods. In this method, the tapered nano/microwires were produced. The dimension of microrods was controlled by growth time.

3.3. Fabrication of nanorod-based LEDs

Undoped ZnO and Ga-doped ZnO nanorods were used for the fabrication of light emitting diodes. Figure 3.6 shows the schematic of each step of LED fabrication. For the fabrication of nanorod-based LEDs, the nanorods were grown on p-type Si substrate using vapour phase transport method (Figure 3.6 (a)). After growing nanorods, the PMMA was coated using a spin coater at 2000 rpm rotation speed. As shown in Figure 3.6 (b), the nanorods were dipped under PMMA solution after coating. The gaps between nanorods were filled by this PMMA solution. A reactive ion etcher was used to produce exposed nanorods tips (Figure 3.6 (c)) by removing the PMMA from the top surface. To optimise the etching thickness of PMMA, a plot of etching thickness vs time was adopted by keeping the oxygen flow rate constant. The etching thickness of PMMA was measured using a J.A. Woollam V-VASE ellipsometer and scanning electron microscope. An Edwards E306 sputtering system was used to deposit indium-tin-oxide (ITO) layer on exposed nanowire tips (Figure 3.6 (d)). The thickness of ITO layer was ~200 nm. A shadow mask was used to control the device's dimension.

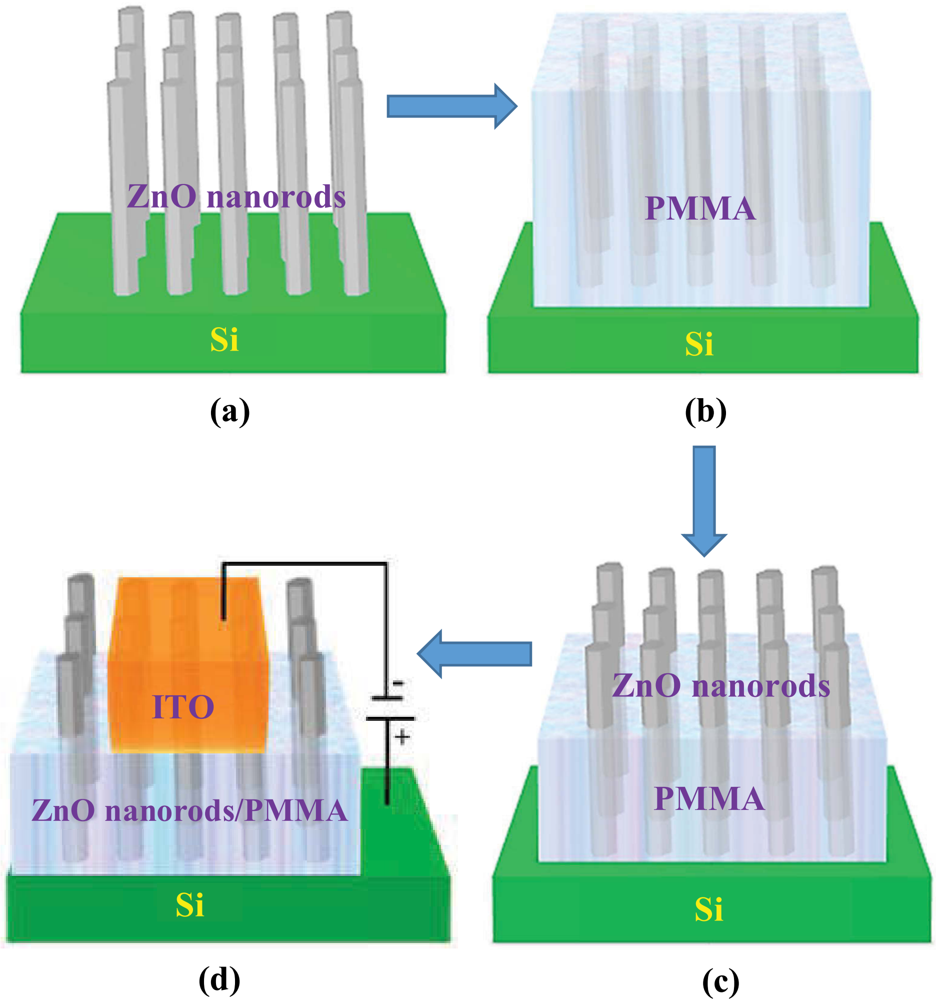

Figure 3.6. Schematic illustration of ZnO nanorod-based LED fabrication process. (a) As-grown nanorods on the p-Si substrate. (b) The PMMA coating on as-grown nanorods. (c) Exposed nanorods tip after oxygen plasma etching. (d) Deposition of ITO layer (yellow colour) on the exposed nanorods tips.

3.4. Structural and morphological characterisation

X-ray diffraction

The structural parameters were calculated from x-ray diffraction data. A Siemens D5000 X-ray diffractometer was used to characterise doped ZnO nanostructures. The diffraction data were collected within the range of $2\theta = 15 - 60$ degrees. The Cu-K_α radiation of wavelength 1.54059Å was used for this measurement.

Raman Spectroscopy

The Raman spectroscopy was used to characterise the crystal structure of doped ZnO nanostructures. The samples were excited by the 633 and 458 nm laser lines. The room temperature Raman spectra were collected using Renishaw and LabRAM HR800 spectrometers.

Scanning electron microscopy

A Zeiss Supra 55VP SEM was used for the morphological analysis of doped ZnO nanostructures. A high-accelerating voltage between 5-30 keV was used to collect the images of nanostructures. The elemental analysis was performed using Zeiss Evo LS15 scanning electron microscope (SEM) attached with an Energy Dispersive X-ray (EDX) of model Bruker SDD EDS Quantax 400.

Transmission electron microscopy

A transmission electron microscope (TEM) was used to determine the morphology and crystal structure of doped ZnO nanostructures. For these analyses, nanostructures were transferred from the substrate onto a 400 mesh Cu grid. TEM imaging and selected-area electron diffraction (SAED) were performed using an FEI Tecnai T20 TEM at 200 keV.

Atomic force microscopy

An atomic force microscope was used to characterise the surface properties (roughness and crystal size) of doped ZnO nanostructures. The surface morphology and root-mean-square roughness of doped ZnO nanostructures were characterised by a Nanoscope IIIa Dimension 3100 Scanning Probe Microscope (Digital Instruments) in non-contact mode.

X-ray photoelectron spectroscopy

An X-ray photoelectron spectroscopy (XPS) was used to characterise the electronic and chemical state doped ZnO nanostructures by analysing the kinetic energy distribution of the ejected electron from nanostructures. XPS spectra were collected in the 90-1500 eV energy range from the Australian Synchrotron laboratory.

3.5. Luminescence spectroscopy

The light emission from a material by the excitation of an electron is known as cathodoluminescence (CL). In the cathodoluminescence spectroscopy, the high-energy electrons supply to a material for the transition of the valence band electrons to the conduction band. In this process, the light can be emitted by the different recombination mechanisms. These emissions can be divided into two categories such as intrinsic and extrinsic [169]. The intrinsic emission is due to recombination via electron in the conduction and the hole in the valence band while the extrinsic emission is attributed to recombination of localised states in the bandgap. These localised states are donors, acceptors, deep level defects and bound excitons. The physical processes in CL system have been illustrated in Figure 3.7.

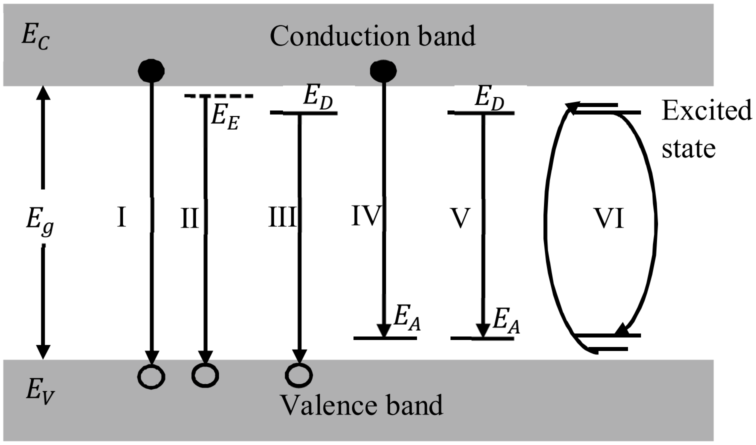

Figure 3.7. Schematic of recombination channels among electrons, holes and defect states in a semiconductor [169].

Channel-I occurs between the conduction band electron and the valence band hole, leading to an emission of a photon of energy equivalent to the bandgap. Channel II is excitonic recombination involving free and/or bound excitions. Channels III, IV, and V are originated from the transitions involving donor and acceptor states. Channel VI is originated from the excitation and radiative deexcitation of an impurity with incomplete inner shells, such as transition metal or rare earth ion.

3.5.1. Experimental setup of cathodoluminescence

The CL system mainly consists of ESEM, spectrometer, parabolic mirror and monochromators (Figure 3.8). An FEI quanta 200 ESEM is equipped with an electron gun, the sample stage and parabolic mirror. The electron beam incidents on the sample through a tiny hole of 30 µm diameter in the centre of the parabolic mirror. This mirror collects the emitted light from a sample and sends to the spectrometer through an optical system. The position of a sample can be easily controlled by a computer-controlled sample stage. A Hamamatsu spectrometer consists of various grating configuration to obtain high-resolution spectra from a sample. This spectrometer is particularly used to examine the fine structure in the spectrum. A photomultiplier was connected to a monochromator for collecting partially resolved CL. The sample can be characterised from 300 K to 10K by this CL system with liquid nitrogen, liquid helium and SEM cold stage.

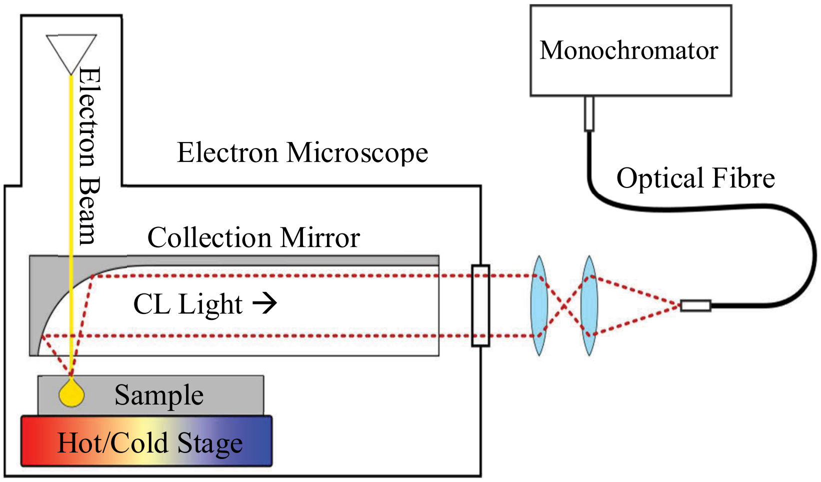

Figure 3.8. Schematic diagram of the experimental setup for CL [170].

3.5.2. Experimental setup of electroluminescence

The light emission properties of undoped and Ga-doped ZnO nanorods/p-Si LEDs were measured by an electroluminescence (EL) system as shown in Figure 3.9. A programmable power supply was used for the electrical excitation of nanorod-based LEDs. A collimator lens collects the emitted light from the LED and sends to the spectrometer. A QEPro ocean optics spectrometer was used for the collection of EL spectra. A computer-controlled OCEANVIEW software was used to analyse the EL spectra.

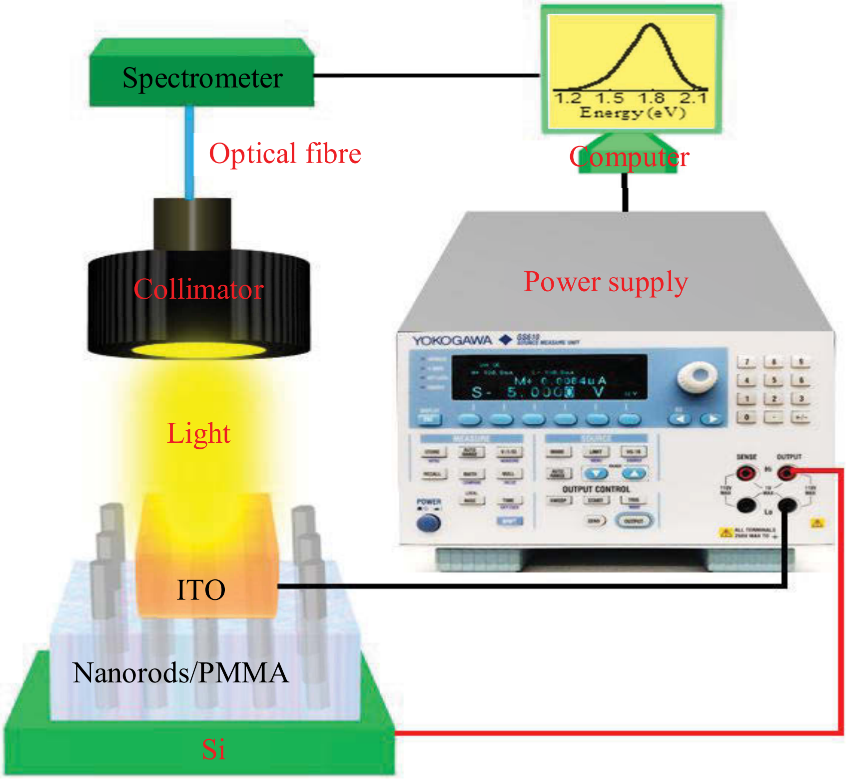

Figure 3.9. Schematic diagram for the experimental setup of EL.

3.5.3. CL calibration

The corrected CL data are important to estimate the following parameters of an emission peak:

1. To determine the real integrated intensities.
2. To calculate the FWHM and peak position of CL spectra.
3. To analysis the superimposed CL emission peaks.
4. To study the recombination kinetics of luminescence centres and types of recombination.

A known light source (tungsten and deuterium lamps) was used to obtain a system response curve (calibration curve) (Figure 3.10). The light was collected by placing the lamp at a suitable distance from the detector. The intensity of the system response curve can be expressed by the following formula:

$$I_{SR} = \frac{I_M - I_D}{I_C} \tag{3.4}$$

where I_M is the measured intensity, I_D is the intensity of dark counts and I_C is the calculated intensity. The calculated intensity can be expressed as [171]:

$$I_C = \frac{1}{\lambda^5} * \exp\left(A + \frac{B}{\lambda^2}\right) * \left(C + \frac{D}{\lambda} + \frac{E}{\lambda^2} + \frac{F}{\lambda^3} + \frac{G}{\lambda^4} + \frac{H}{\lambda^5}\right) \tag{3.5}$$

where $A = 41.35$, $B = 4887.34$, $C = 0.80$, $D = 446.24$, E= 308810.22, $F = 76184523.47$, $G = 6965711712.06$ and $H = 0$.

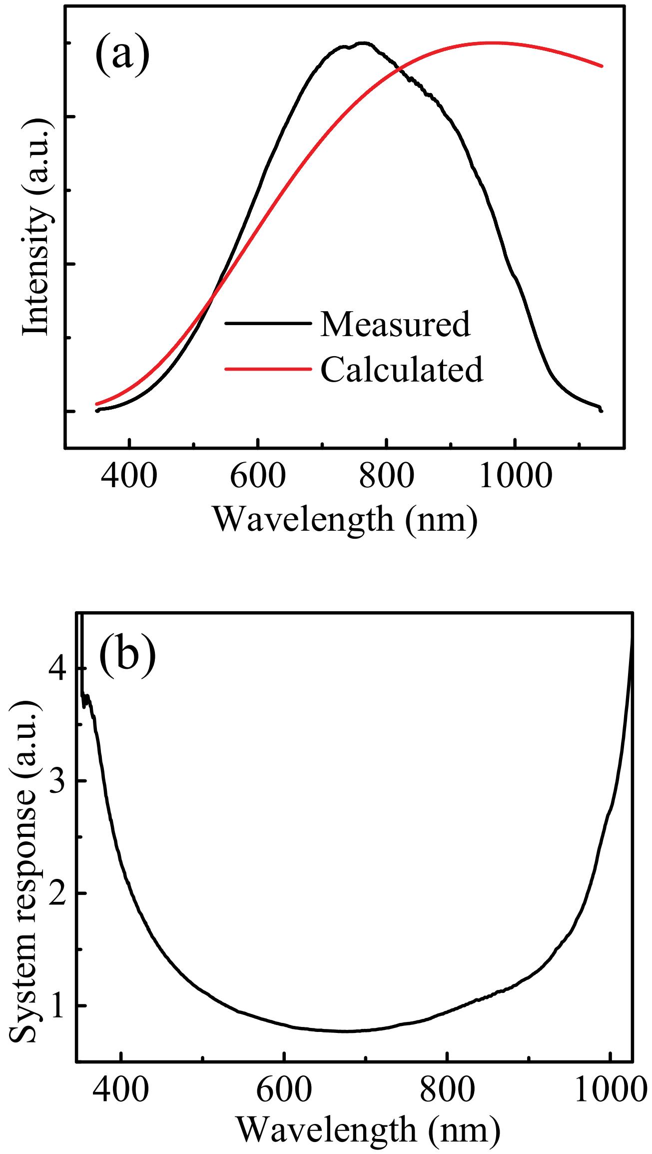

Figure 3.10. (a) The measured and calculated spectra for the tungsten filament quartz halogen lamp. (b) The total response curve obtained using equation (3.4).

The corrected CL data can be calculated using the following equation

$$I_{CL}(corrected) = \frac{I_M \times I_{SR}}{E^2} \tag{3.6}$$

where $E\ [= 1239.84/\lambda(nm)]$ is the photon energy in eV.

The high-resolution Hamamatsu CCD spectrometer gives CL intensity as a function of the pixel. A standard Hg lamp was used to convert pixel to wavelength. The NIST atomic spectral database of Hg lines was used to find the wavelengths of the corresponding pixels. Figure 3.11 (a) shows the Hg lines as a function of the pixel. The wavelength versus pixel plots give a straight line (Figure 3.11 (b)) with slope = 0.0532 nm and intercept = 356.797 nm. The formula for the conversion of the pixel to wavelength can be expressed as

$$\lambda = Intercept + (slope \times pixel) \tag{3.7}$$

In this project, the grating 1 of wavelength range 50 nm was used to investigate the fine structure in the near-band-edge spectra of undoped and Ga-doped ZnO nano/microrods. The calibration of intensity for grating 1 is not necessary because of its flat nature of spectral response curve for the small spectral range of about 50 nm.

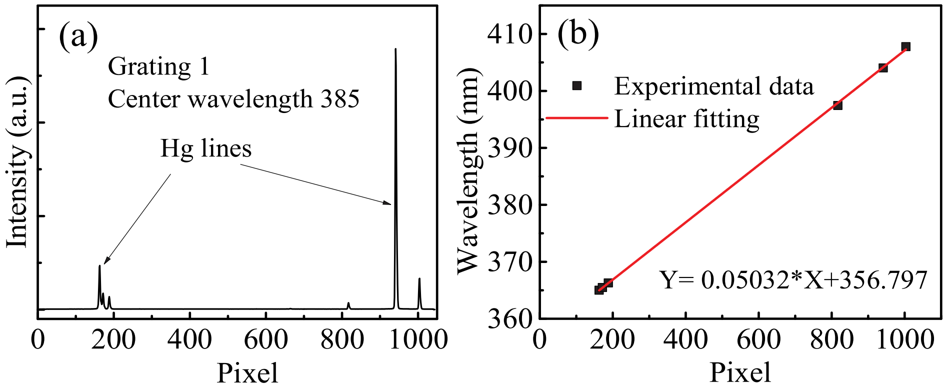

Figure 3.11. (a) CL intensity of Hg lines as a function of pixel. The spectrum was collected using Hamamatsu CCD spectrometer for grating 1 at 385 nm central wavelength. (b) The wavelength from the NIST chart as a function of pixel showing a straight line with slope = 0.0532 nm and intercept = 356.797 nm.

3.5.4. Simulation of CL generation depth

The CL is a powerful method for the analysis of defects along the depth of a sample from few nanometres to several micrometres, depending on the accelerating voltage for a given material. The CL generation depth is determined from the size of electron interaction volume inside the sample. Several models have been proposed to determine CL generation depth. The CL generation depth (R_{CL}) as a function of electron beam energy (E_B) is given by the Gruen range equation [169, 172].

$$R_{CL} = \frac{k}{\rho} E_B^Z \tag{3.8}$$

where k and Z are the function of atomic number and energy, respectively and ρ the density of a material.

Everhart and Hoff proposed a model to estimate CL generation depth as [169]:

$$R_{CL} = \frac{0.0398}{\rho} E_B^{1.75}\ (\mu m) \tag{3.9}$$

where the energy of electron beam and the density of material are expressed in keV and g/cm^3, respectively. This equation is derived for an accelerating voltage range of 5 - 25 keV and atomic number of 10 - 25.

Kanaya and Okayama proposed an expression, which is more general for the CL generation depth in a wide range of accelerating voltage and atomic number [169].

$$R_{CL} = \frac{0.0276 \times A}{\rho Z^{0.889}} E_B^{1.67}\ (\mu m) \tag{3.10}$$

where Z is the atomic number, and A is the atomic weight. E_B and ρ are expressed in eV and g/cm^3. The shape of CL generation volume largely depends on the value of the atomic number. A spherical shape is found for an atomic number range of 15-40 and a hemispherical shape for the larger value of Z [169]. The number of generated electron-hole pairs is given by a generation factor (G) as [169].

$$G = \frac{E_b(1-\gamma)}{E_i} \tag{3.11}$$

where γ is the portion of energy loss due to the backscattered electrons and E_i is the required average energy for the formation of electron-hole pairs. The value of E_i can be estimated from the bandgap $(E_g\ )$ of a material: $E_i = 2.8\ E_g\ + M$, where the value of M varies in the range 0 – 1 eV depending on the type of material, but independent on E_b.

The distribution of luminescence centres along the depth of doped ZnO nanostructures was analysed by depth-resolved CL method. In this method, the accelerating voltage (V_a) and beam current (I_b) were varied by keeping the excitation power $(V_a I_B)$ constant. The aim of depth-resolved CL is that the luminescence spectra can be achieved from the various depth of a sample by keeping the number of generated electron-hole pairs constant. The CL generation depth of undoped and Ga-doped ZnO was obtained using the Monte Carlo CASINO simulation program (Figure 3.12). The key parameters used in this simulation are the electron beam energy $(E_B = 5 - 30\ keV)$, beam radius $(r_B = 6\ nm)$ and the number of electrons $(N = 1.5 \times 10^7)$. The atomic fraction of Ga, Zn and O were 5, 50 and 45%, respectively.

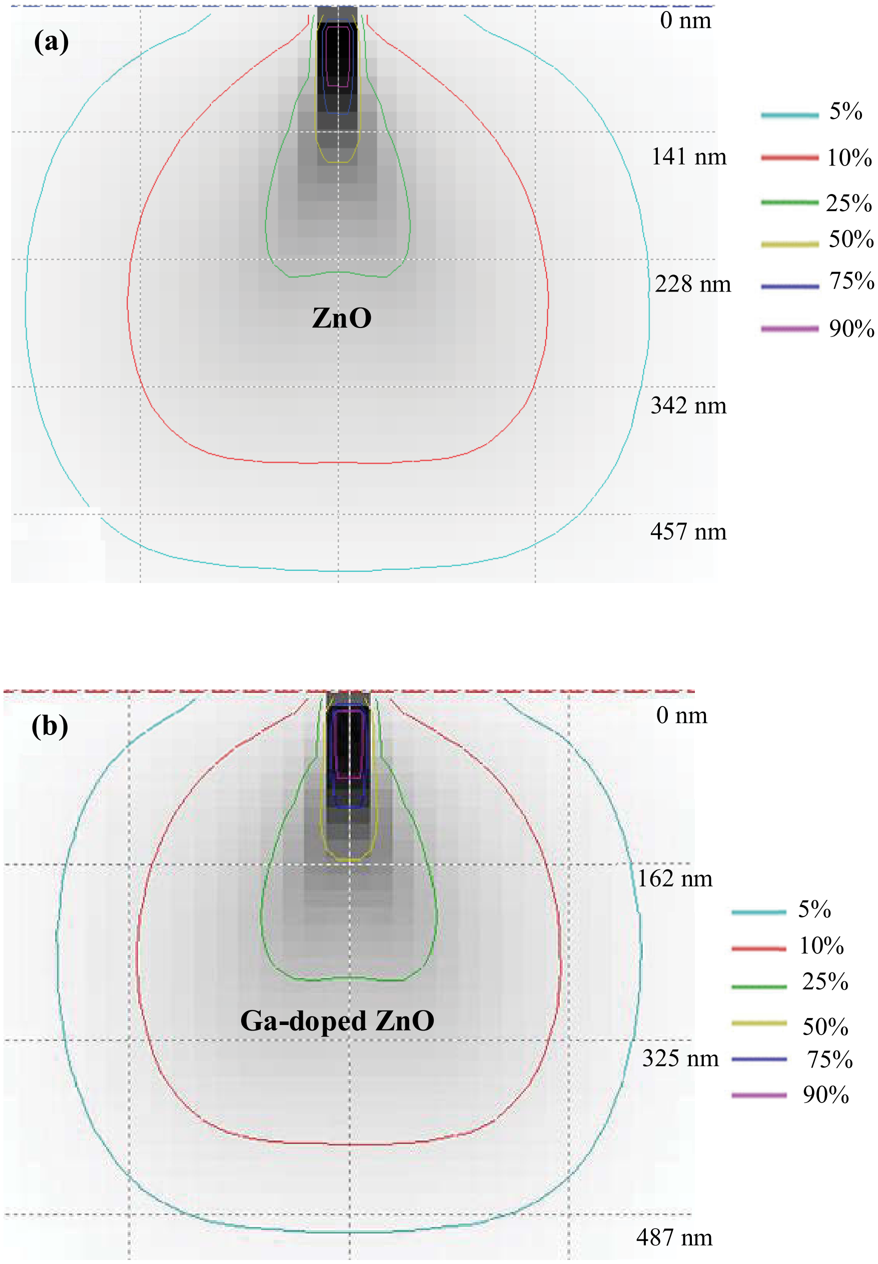

Figure 3.12. The electron beam interaction volume in (a) undoped and (b) Ga-doped ZnO at 10 keV.

Figures 3.12 (a)-(b) show the electron beam interaction volume of undoped and Ga-doped ZnO. The electron interaction volume increases with increasing energy of the incident electron beam. By varying the electron beam energy from 5 keV to 30 keV and considering 5% energy loss, the CL generation depth can be obtained from 50 to 2500 nm along the depth of a sample. The accelerating voltage was used between 5-20 keV, depending on the thickness of a sample.

3.5.5. Excitation density-dependent CL

The power-resolved measurements were carried out to study recombination kinetics of luminescence centres. In these measurements, the samples were excited by the different beam currents, while the accelerating voltage was kept constant. The integrated intensity of emission is determined by the Gaussian fitting of a spectral peak. The CL integrated intensity is related to the excitation power by the following relation [173]:

$$I_{CL} \, \alpha \, P_b^n \tag{3.12}$$

where I_{CL} and P_b are the integrated CL intensity and the excitation power, respectively. The index, n, is determined by plotting the log integrated intensity as a function the log excitation power and applying a linear fit. The value of n depends on recombination kinetics of luminescence centres. The power law exponent 'n' provides the nature of recombination mechanism in the film. The super-linear recombination kinetics is expected ($n > 1$) for excitonic and band-to-band recombinations, while the sub-linear relationship ($n < 1$) is expected for deep levels [173]. The exact value of n for deep levels significantly influences the saturation rate of recombination centres, depending on recombination lifetimes and carrier capture rate [173]. The radiative lifetime for excitons in ZnO is about 1 ns, while the characteristic recombination time of green emission varies in the range from 0.2 to 10 ns [44].

3.6. Electrical measurements

3.6.1. Current-voltage characteristics

Current-voltage (*I-V*) characteristics of a heterojunction LEDs provides several junction parameters such as the series resistance (R_s), shunt resistance (R_{sh}), threshold voltage (V_{th}), reverse saturation current (I_s), diode ideality factor (n), rectification ratio (I_F/I_R) and barrier potential $(\emptyset_b)$. The *I-V* characteristics of heterojunction LEDs can be expressed according to the diffusion-recombination model as [174]:

$$I = I_s\left(exp\left(\frac{qV}{nk_BT}\right) - 1\right) \tag{3.13}$$

where q is the charge of the electron, V is the bias voltage, k_B is the Boltzmann constant and T the temperature in Kelvin. The dark saturation current is given by the following equation:

$$I_s = AA^*T^2exp\left(-\frac{q\emptyset_b}{k_BT}\right) \tag{3.14}$$

where A is the device area and $A^*(= 32\ Acm^{-2}K^{-2})$ the Richardson's constant [175]. The value of $n\ (= (q/k_BT) * (dV/dln(I)))$ can be calculated from $ln(I)$ vs V plot. The $\emptyset_b$ can be calculated from the following relation;

$$\emptyset_b = \left(\frac{k_B T}{q}\right) ln\left(\frac{AA^* T^2}{I_s}\right) \tag{3.15}$$

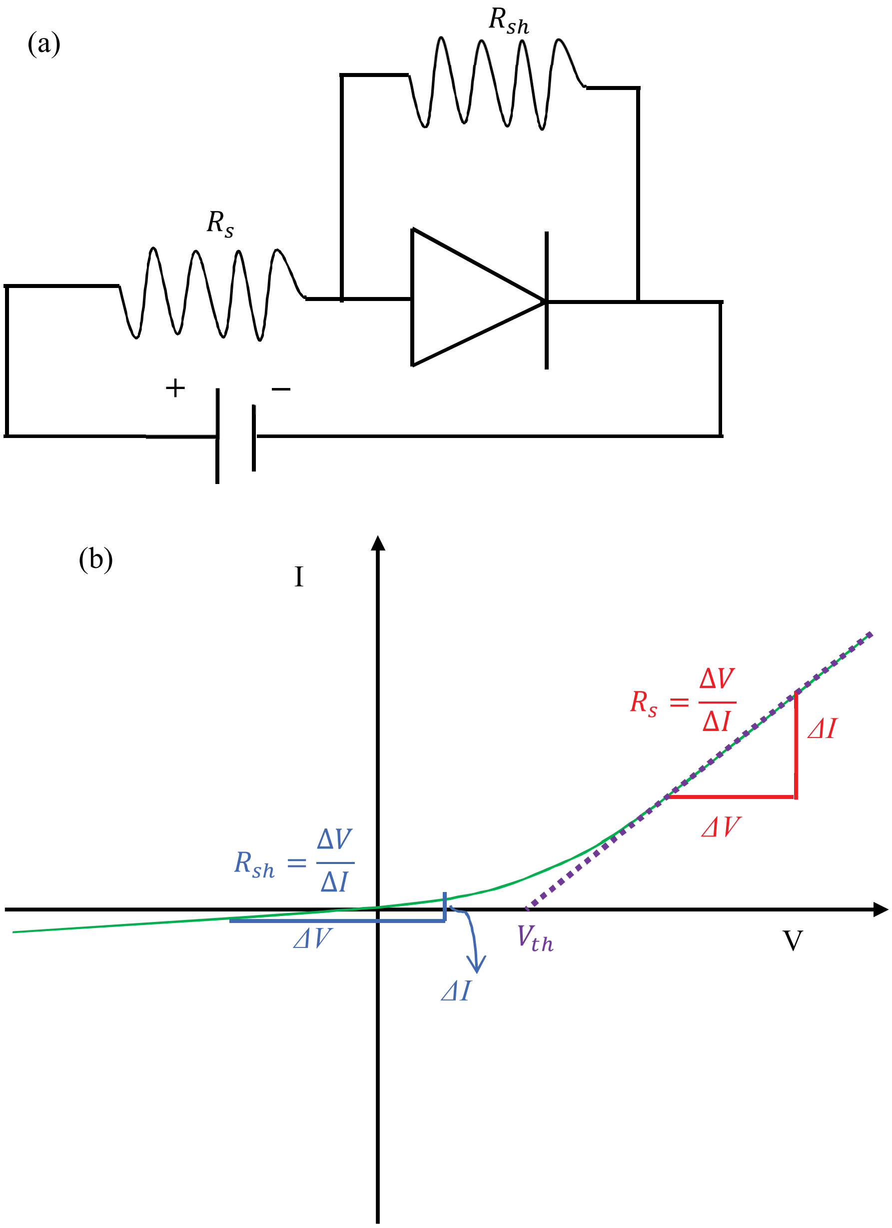

Figure 3.13. (a) Schematic diagram of one diode equivalent circuit consisting of a series resistance and shunt resistance was used to model the electrical characteristics of ZnO nanorod-based LEDs. (b) A typical I-V curve for a LED.

The *I–V* characteristics were analysed by using a one-diode equivalent circuit shown in Figure 3.13 (a). The series resistance (R_s), which arises from the resistance of the substrate and nanostructures, is determined from the linear region of the *I-V* curve in the high voltage region (Figure 3.13 (b)). The shunt resistance (R_{sh}), which represents parasitic leakage current through the heterojunction LED, is calculated using the slope at near-zero voltage region (Figure 3.13 (b)). The turn-on voltage of heterojunction LEDs is determined by extrapolation of the linear region of the *I-V* curve. A Yokogawa GS610 power supply was used to measure the *I-V* characteristics of ZnO nanorods/p-Si heterojunction LEDs.

Chapter 4

Li acceptors in ZnO

Resistive random-access memories have attracted a great deal of attention as emerging non-volatile data storage technologies. Li-doped ZnO is a promising system for potential applications in optoelectronic memory devices due to its high transparency to visible light and tunable optoelectronic properties by varying the doping level. This material exhibits various physical phenomena including ferroelectricity, magnetism, and p-type conductivity, depending on Li doping level. While several research groups have reported p-type ZnO using Li, there are still problems regarding the stability and reproducibility of the p-type conductivity. In this chapter, the defect states produced by Li dopants and their role on the optoelectronic properties of ZnO are investigated.

4.1 Introduction

Recent interest in Li as a dopant in ZnO has been stimulated by its potential use as a *p*-type dopant as well as its ability to facilitate tuning of the colour of the ZnO luminescence [176, 177]. Previous studies on hydrothermally grown single crystals showed that Li dopants predominantly occupy the Zn lattice site and induce ~ 150 meV shallow and ~ 800 meV deep acceptor levels above the valence band maximum [9, 101]. The deep Li_{Zn} acceptor produces yellow luminescence band in the 1.9-2.2 eV energy range [170]. It has also been theoretically predicted that the transient shallow acceptor state is associated with a Li_{Zn} complex [100]. Li-doped ZnO has relatively long phonon lifetime (> 1 ps) in comparison with pure and doped

ZnO and that this material can be used as an efficient photocatalyst for the degradation of pollutants and bacteria in water [178]. Recent reports on the ferroelectricity [179] and *p*-type conduction of Li-doped ZnO [11] also illustrate the enormous potential applications of this material.

Several techniques suitable for fabrication of small as well as large area, functional ZnO films, such as pulsed laser deposition and sputtering, have previously been investigated [111, 117]. These ZnO films typically exhibit a green luminescence band, attributed to oxygen or zinc vacancies, depending on fabrication conditions [44]. However, these techniques pose difficulties in fabricating alloy films with controllable compositions due to differential sputtering rates of deposited materials. The spray pyrolysis method used in this study is an economically attractive, flexible technique, which is capable of precisely controlling the film composition. Using the improved atomizing system described in detail in the chapter 3, a series of pure and Li-doped ZnO films with bright visible luminescence were grown successfully. This study demonstrated for the first-time that ZnO films exhibit multi-coloured emissions of blue, green and yellow, which can be tuned by varying the Li concentration. The films fabricated by this method displays multi-coloured emissions, which could open the door of multi-coloured display applications.

The work in this chapter is aimed to investigate the effects of Li incorporation on the optical properties of spray pyrolytic Li-doped ZnO films and the luminescence tunability of ZnO mediated by Li doping. The nature of luminescence centres in Li-doped ZnO films and their strengths of electron-phonon coupling are also investigated by simulating the luminescence spectra within the framework of the Huang-Rhys model.

4.2 Structural properties of Li-doped ZnO films

Figure 4.1 shows the XRD patterns of the sprayed Li-doped ZnO films with nominal Li concentrations up to 4 at%. The diffraction scan was carried out within the Bragg diffraction angle (θ_B) of $25 \leq 2\theta_B \leq 65$ degrees using CuK_α radiation. The XRD patterns reveal that the films possess a wurtzite structure. The XRD (002) peak is enhanced relative to other diffraction peaks after the Li doping, this is consistent with an improvement of crystal quality of the deposited film. This result can be due to heterogeneous nucleation being facilitated in the presence of Li^+ ions in the ZnO structure [180]. This could also be due to a slight orientation redistribution of grains [181]. The diffraction angle and full width at half-maximum of diffraction peak have not been significantly changed with increasing Li-doping concentration in the ZnO film.

The crystalline size, *D,* as determined by Scherrer's formula:

$$D = \frac{k\lambda}{\beta_{hkl} cos\theta} \tag{4.1}$$

here k is the shape factor ($k = 0.89$) [182] and λ the wavelength ($\lambda = 1.54059$ Å) and β_{hkl} the instrumental corrected broadening. The β_{hkl} for each diffraction peak can be calculated using the following equation:

$$\beta_{hkl}^2 = \beta_{measured}^2 - \beta_{Instrumental}^2 \tag{4.2}$$

The integral width β was calculated, after correction for instrumental XRD broadening, yielding a crystallite size of 37 ± 2 nm for the undoped and Li-doped ZnO films.

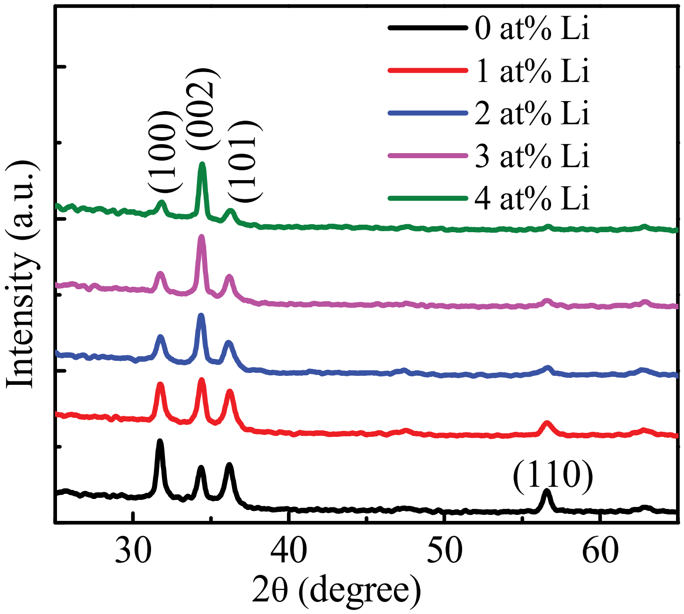

Figure 4.1. XRD patterns of the Li-doped ZnO films with nominal Li concentrations of 0, 1, 2, 3 and 4 at%, showing the *c*-axis growth orientation increased with Li doping concentration into the ZnO film.

The lattice constants a and c of undoped and Li-doped ZnO films for (002) orientation can be calculated using the following expressions:

$$a = \frac{\lambda}{\sqrt{3\, sin\theta_B}} \tag{4.3}$$

$$c = \frac{\lambda}{sin\theta_B} \tag{4.4}$$

The interplanar spacing (d) is calculated using the Bragg's diffraction relation:

$$2dsin\theta_B = n\lambda \tag{4.5}$$

where, n is the diffraction order. The values of d have been calculated for the first-order diffraction.

The unit cell volume (V) of the films can be calculated by the following equation:

$$V = 0.866 \times a^2 \times c \tag{4.6}$$

The values of interplanar spacing, lattice constants and unit cell volume are presented in Table 4.1. It is observed from Table 4.1 that the values of interplanar spacing, lattice constants, unit cell volume have not been significantly changed with Li doping concentration in the range of 0 - 4 at%. In the lower doping range, the unchanged value structural parameters are expected since Zn and Li atoms have similar sizes (74 Å Vs 76 Å).

Table 4.1. The lattice parameters, unit cell volume, grain size and interplanar spacing of Li-doped ZnO films.

Li (at%)	Lattice constants (nm)		Unit cell volume $(nm)^3$	Grain size (nm)	Interplanar spacing (Å)	
	a	c			(100)	(002)
0	0.3245	0.5211	0.0475	35	2.809	2.606
2	0.3254	0.5196	0.0476	39	2.818	2.598
3	0.3246	0.5205	0.0475	36	2.811	2.602
4	0.3243	0.5208	0.0475	39	2.809	2.604

For the (002) preferred growth direction, the texture coefficient, $TC_{(hkl)}$, can be calculated using Harris method [183]:

$$TC_{(hkl)} = \frac{I\ (hkl)/I_o\ (hkl)}{(1/N)\sum I\ (hkl)/I_o\ (hkl)} \tag{4.7}$$

where $I\ (hkl)$ is the measured intensity of reflection, $I_o\ (hkl)$ is the corresponding standard intensity from the JCPDS data card No-05-0664 and N is the number of reflections observed in the XRD pattern. Figure. 4.2 shows the calculated values of texture coefficient for (002) orientations of Li-doped ZnO films as a function of Li doping concentration. The texture coefficient for (002) orientation of undoped ZnO is found to be 0.85. As shown in Figure 4.2, the value of texture coefficient is found to increase from 1.4 to 1.8, when Li doping concentration increase from 1 to 4 at%, indicating the enhanced (002) direction with increasing Li doping.

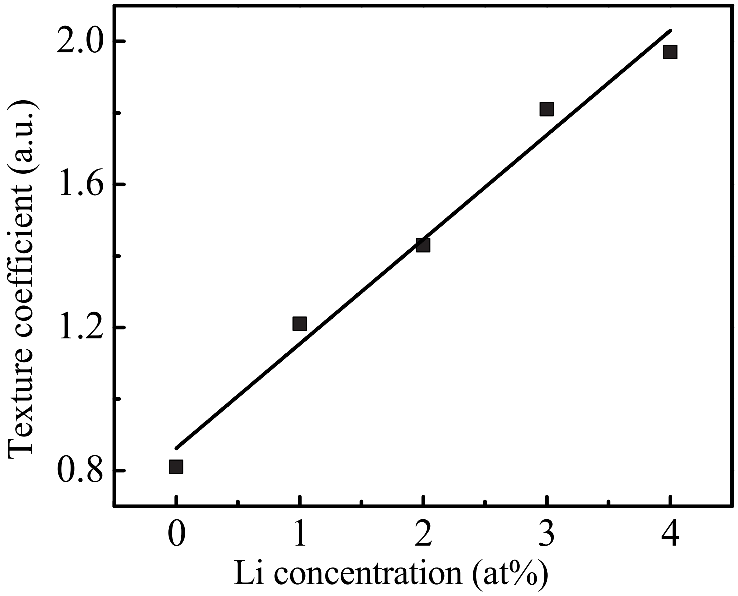

Figure 4.2. The texture coefficient as a function of Li doping concentration, showing the increasing trend with increasing Li.

The film surface morphology was also studied by the non-contact mode atomic force microscopy. Figures 4.3 (a) - (b) show the AFM images of undoped and 4 at% Li-doped ZnO films. The AFM images reveal that the surface of the films is reasonably smooth. Both the undoped and Li-doped ZnO films have root mean square (RMS) roughness of order ~ 10 nm for a surface area of 5×5 μm^2. The Li doping ($0 \leq \text{Li} \leq 4$ at%) has no significant influence on the surface morphology of the film.

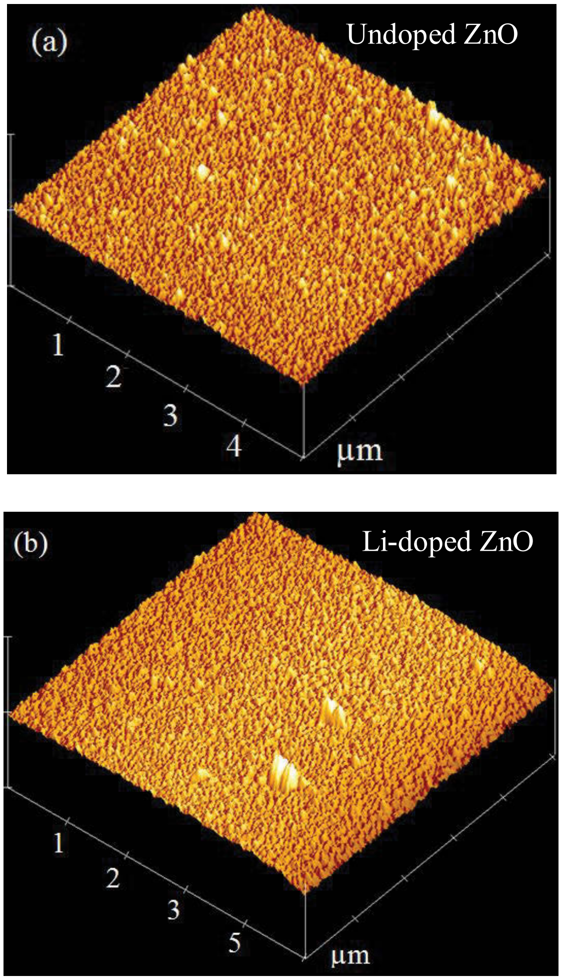

Figure 4.3. (a) - (b) AFM images of undoped and 4 at% Li-doped ZnO films showing a root-mean-square roughness of 10 nm for a surface area of 5×5 μm^2.

4.3. Optical properties of Li acceptors in ZnO

4.3.1. Li-related emissions in ZnO

Figure 4.4 (a) shows the CL spectra at 80 K of 0, 1, 2, 3 and 4 at% Li-doped ZnO films. The spectrum of the pure ZnO film exhibits a weak near-band-edge emission at 3.32 eV and an intense green luminescence (GL), which decreases dramatically with the incorporation of Li. This symmetrical GL peak at 2.43 eV has been attributed to zinc vacancy (V_{Zn}) [44], which is a deep acceptor in ZnO. The spectra of the Li-doped ZnO films are dominated by two visible emissions centred at 1.90 eV (yellow luminescence, YL) and 3.00 eV (blue luminescence, BL), which both have been attributed to Li acceptors and/or acceptor complexes in ZnO [74, 170].

Figure 4.4 (b) shows the CL integrated intensity of UV, BL, GL and YL emissions as a function of Li doping concentration. With increasing the Li concentration, the YL and BL intensities monotonically increase whereas the V_{Zn}-related GL at 2.43 eV decreases and becomes negligible at 4 at% Li. This observation is consistent with Li dopants occupying the Zn lattice site, leading to a decrease in the concentration of V_{Zn} defects. On the other hand, Li interstitial in ZnO can act as a donor, increasing the conductivity of ZnO films [184]. The Li-doped ZnO films fabricated in this project are, however, electrically insulating. This also suggests most Li dopants are incorporated at Zn vacancy sites, consistent with the interpretation of the optical characterization results. Incorporation of 4 at% Li leads to complete quenching of the GL in the Li-doped ZnO film, which exhibits strong Li-induced YL and BL emissions as the Li luminescence centres become abundant and dominate the radiative recombination.

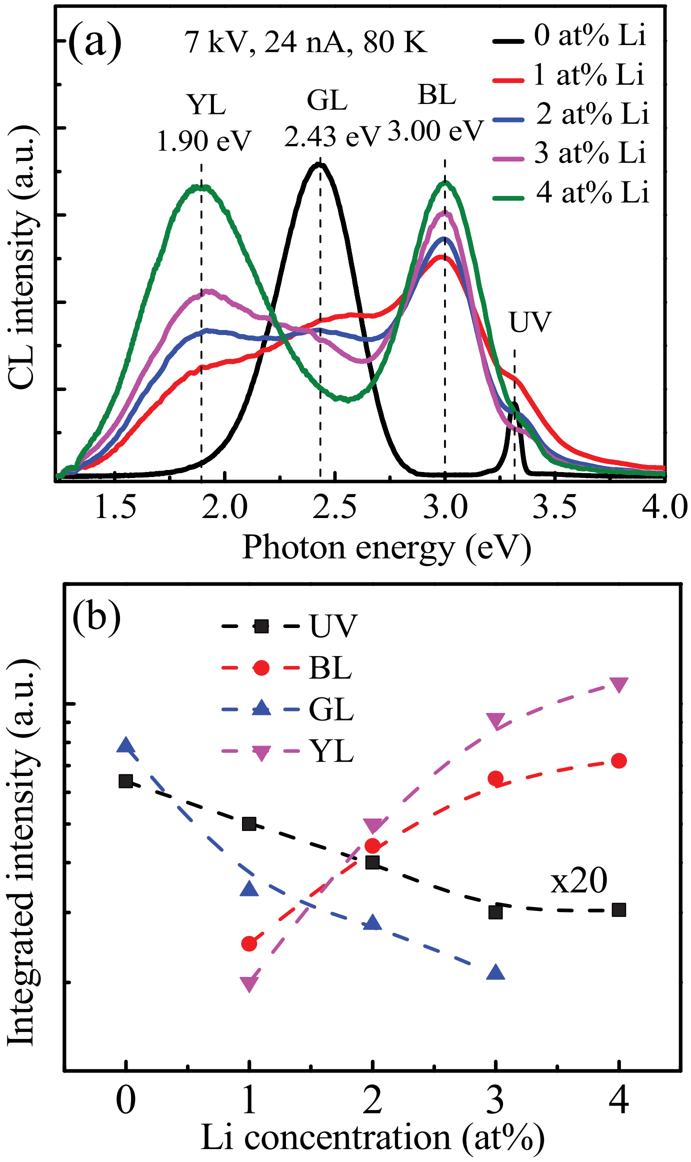

Figure 4.4. (a) CL spectra at 80 K of the Li-doped ZnO films with different Li concentrations showing YL, GL and BL emissions. The YL and BL, which are absent in the undoped ZnO film, arise from the incorporation of Li dopants. (b) The integrated intensities of UV, BL, GL and YL luminescence with Li doping concentration. The intensity of the BL and YL emission increases, while the intensity of the UV and GL decreases with increases Li doping concentration in ZnO.

4.3.2. Recombination kinetics in Li-doped ZnO

To examine the kinetics of the observed visible emissions in Li-doped ZnO, the films were characterised using the power density-resolved CL analysis. In this analysis the beam current was varied in the range from 0.24 to 34 nA while the acceleration voltage was kept constant at 7 kV, corresponding to a CL generation depth of 370 nm [170]. Figures 4.5 (a)-(d) show the CL spectra of 0, 2, 3, and 4 at% of Li-doped ZnO films at different electron beam currents from 0.42 to 34 nA. The CL intensity for all films increases with increasing electron beam current without significant change of peak position and width.

Figure 4.5 (e) shows the Gaussian fitting of UV, BL, GL and YL emissions for 2 at% Li-doped ZnO film. These peak parameters were obtained from the spectral profiles of the undoped ZnO (which exhibits only the GL emission with a peak of 2.43 ± 0.04 eV, FWHM = 0.45 ± 0.03 eV), whereas the 4 at% Li-doped ZnO displays distinct YL (E_{YL} = 1.90 ± 0.04 and FWHM of 0.60 ± 0.03 eV) and BL peaks (E_{BL} = 3.00 ± 0.04 eV, FWHM = 0.38 ± 0.03 eV). To overcome the uncertainty in the spectral fitting, these parameters were constrained in the curve fitting of all other CL spectra.

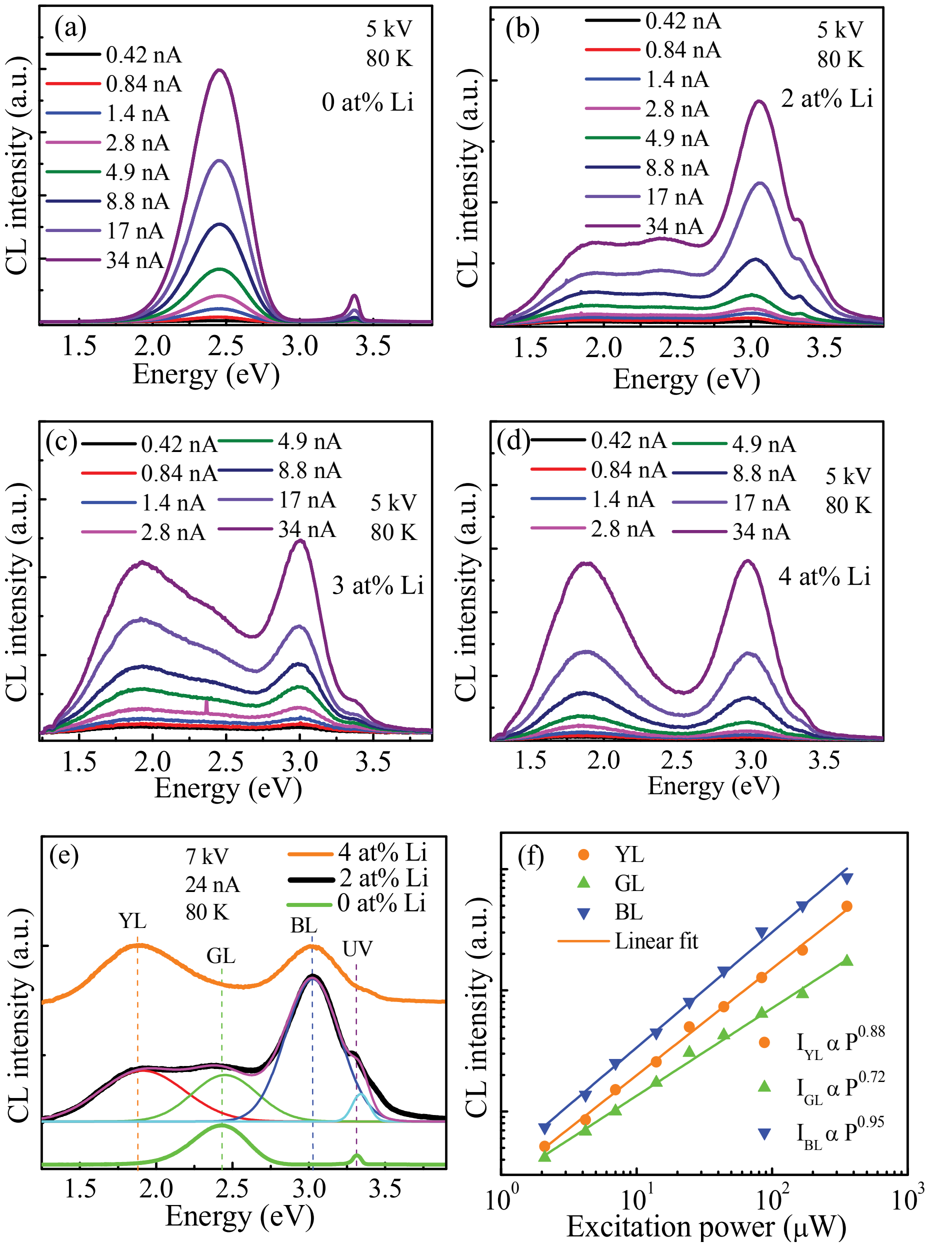

Figure 4.5. The CL spectra of (a) 0 at%, (b) 2 at% (c) 3 at% and (d) 4 at% Li-doped ZnO films at different electron beam currents. (e) The Gaussian fitting of UV, BL, GL and YL emission in 2 at% Li-doped ZnO film. (f) Log-log plots of the integrated intensities of the ZnO GL and Li-induced (2 at% Li) YL and BL at 80 K as a function of excitation power. The solid lines are the power law ($I_{CL}\ \alpha\ P_b^n$) fit to the experimental data.

Figure 4.5 (f) displays the integrated intensities of the YL, GL and BL emissions as a function of the electron beam excitation power. As shown in Figure 4.5 (f), the CL intensities follow the power law ($I_{CL}\ \alpha\ P_b^n$), where I_{CL} and P_b are the integrated intensity of the emission band and the CL excitation power, respectively [173]. The power law exponent 'n' provides the nature of recombination mechanism in the film. The super-linear recombination kinetics is expected ($n > 1$) for excitonic and band-to-band recombinations, while the sub-linear relationship ($n < 1$) is expected for deep levels [173]. The exact value of n for deep levels depends on the saturation rate of recombination centres, especially recombination lifetimes and carrier capture rate [173]. The radiative lifetime for excitons in ZnO is about 1 ns, while the characteristic recombination time of green emission varies in the range from 0.2 to 10 ns [44]. The exponent n of the 2 at% Li-doped ZnO film is found to be 0.88 ± 0.02, 0.72 ± 0.02 and 0.95 ± 0.02 for YL, GL and BL, respectively. The BL and YL emissions possess slower saturation rates (higher n values) than the GL band in the Li-doped ZnO films, even though the Li_{Zn} is known to possess a longer relaxation time [170]. This confirms the existence of abundant Li-related luminescent centres in the films and the success of producing Li radiative centres in ZnO films even at a low deposition temperature of 400°C.

4.3.3. Depth-resolved characteristics of Li acceptors

The depth-resolved CL spectra were collected to examine the distribution of Li acceptors along the depth of the Li-doped ZnO films. For these measurements, the constant power method was employed [185]. For this work the accelerating voltage (V_a) was varied in the range of 2-10 kV while the electron beam current (I_b) was adjusted to keep the electron beam power ($\mathrm{P_B = V_a I_B}$) constant. Figure 4.6 (a) shows the CL spectra of 2 at% Li-doped ZnO film at different accelerating voltages. These spectra were acquired with a constant power (20 μW), while the accelerating voltage was varied from 2 to 10 kV, corresponding to the CL generation depth from 40 to 700 nm as deduced by Monte Carlo stimulation CASINO [186].

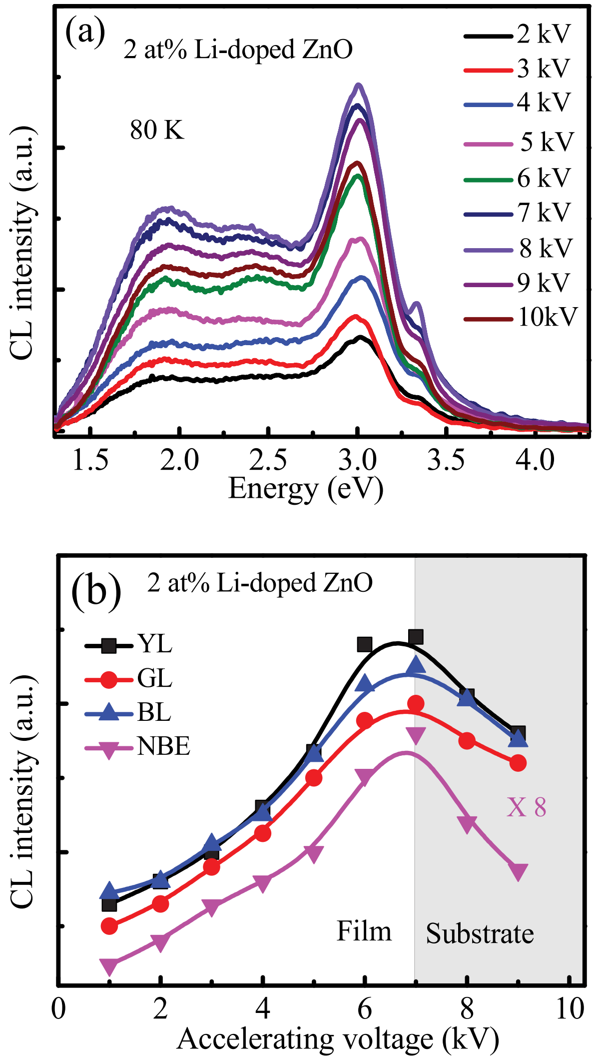

Figure 4.6 (a) CL spectra of 2 at% Li-doped ZnO film at different accelerating voltages, V_a = 2 to 10 kV. The electron beam current was adjusted in order to keep the excitation power constant, $P_B = 20\,\mu W$. (b) The variation of CL integrated intensity as a function of accelerating voltage. The CL integrated intensity of YL, GL, BL and NBE are determined from the Gaussian fitting described in the previous section.

Figure 4.6 (b) shows the variation of the CL integrated intensity of UV, BL, GL and YL emissions as a function of accelerating voltage. It is seen that the integrated intensity of these emissions increases with increasing accelerating voltage and show a maximum value at around 7 kV corresponding to the CL generation depth of 370 nm. The intensity of emissions is started to decrease after 7 kV. The increase of intensity is due to the increase of nonradiative defects density with increasing depth. On the other hand, the decrease of the NBE intensities indicates that a part of the emissions is being reabsorbed by the film. The absorption is due to the pronounced band tail that is resulted from the structural disorder caused by the inhomogeneous strain as well as point and extended defects [187].

4.3.4. Properties of Li luminescence centres in ZnO films

To investigate the nature of the luminescence centres responsible for the YL, GL and BL emissions in the Li-doped ZnO films, these emission peaks were modelled based on the Huang-Rhys model [188], in which the phonon coupling strength of the band-to-defect state transitions is examined. The zero-phonon line (ZPL) and phonon coupling characteristics of the YL, GL and BL recombination centres were modelled using longitudinal optical phonon scattering (E_{LO} = 72 meV). The key parameters used in the simulation are: the Huang-Rhys factor (S) that reflects the electron-phonon coupling strength and the line shape broadening parameter (γ) that reflects the FWHM of the phonon side band.

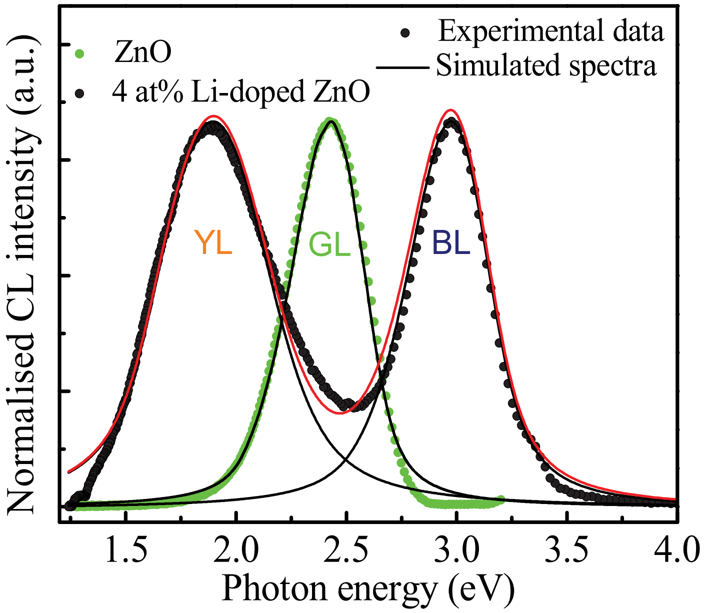

Figure 4.7 Normalised CL spectra of the ZnO and 4 at% Li-doped ZnO films at 80 K with the simulated profiles using the Huang-Rhys model. The characteristic parameters of the three visible luminescent bands, namely YL, GL and BL, are presented in Table 4.2.

The CL intensity according to the Huang-Rhys model can be expressed as [188, 189]:

$$I\,(\hbar\omega) = (\hbar\omega)^3 \exp(-S) \sum_{n=0}^{\propto} \frac{S^n}{n!} \Gamma(\hbar\omega - E_{ZPL} + n\hbar\omega_i) \tag{4.8}$$

where $\hbar\omega$ is the energy of emission band, $\hbar\omega_i$ is the vibronic level spacing, E_{ZPL} is the ZPL energy, n is the number of phonons and Γ is the line shape function. Using the equation above the YL, GL and BL peak profiles are simulated using the parameters presented in Table 4.2. The modelled spectra are displayed as solid curves in Figure 4.7, which show excellent fits to the experimental CL data at 80 K (solid circles).

Table 4.2. Parameters for the YL, GL and BL centres in the Li-doped ZnO films deduced from the modelling of the vibronic spectra based on the Huang-Rhys model.

Emission	**Zero phonon energy, E_{ZPL} (eV)**	**Huang-Rhys factor (S)**	**Broadening factor, γ (eV)**	**Defect assignment**	**Defect energy (meV)**
Blue	3.20 ± 0.02	3.1 ± 0.04	0.20 ± 0.03	Li_{Zn}	150 ± 20
Green	2.80 ± 0.02	6.2 ± 0.05	0.14 ± 0.03	V_{Zn}	550 ± 20
Yellow	2.52 ± 0.02	7.2 ± 0.08	0.28 ± 0.03	Li_{Zn}	830 ± 20

From the simulated spectra of the ZnO and Li-doped ZnO films, the energies of the YL, GL and BL centres are found to be 150 ± 20, 550 ± 20 and 830 ± 20 meV above the valence band maximum, respectively. The Huang-Rhys factors for the GL and YL in the pyrolytic Li-doped ZnO films are slightly smaller than those fabricated by high-temperature chemical vapour deposition [102, 190], presumably due to lower crystallinity. Previous theoretical and experimental studies showed the existence of both Li_{Zn}-related shallow (150 – 350 meV) and deep (850 – 950 meV) acceptor levels [101, 191]. The energy of the BL centre in the Li-doped ZnO films obtained from the Huang-Rhys simulation is consistent with the shallow acceptor, thus it is tentatively attributed to Li_{Zn}. The presence of multiple luminescence centres in the Li-doped ZnO film associated with Li_{Zn} is thought to be due to the non-axial Li-O bonding, which leads to a hole being trapped at an oxygen ion axially or non-axially bounded to the Li ion [192].

4.4. Conclusions

Undoped and Li-doped ZnO films with bright visible luminescence were fabricated by the spray pyrolysis technique. The pyrolytic films exhibit multi-coloured emissions of yellow, green and blue, which can be tuned by varying the Li concentration. The V_{Zn}-associated green luminescence in the ZnO film can be medicated by Li dopants. Simulation of the cathodoluminescence spectra from the Li-doped films using the Huang-Rhys model reveals the energies of the luminescence centres and their electron-phonon coupling strength. The characteristic parameters of the visible luminescence centres obtained from the Huang-Rhys simulation of the CL spectra of the pyrolytic films are similar to the reported values for V_{Zn} and Li_{Zn} defects in ZnO films fabricated by high-temperature growth.

Chapter 5

Cu acceptors in ZnO nanorods

Transition metals in ZnO can offer the possibility of spintronics that can integrate both the magnetic and optical effects such as spin-polarised solar cells and spin light emitting diodes. Apart from spintronic devices, many transition metal impurities including Cu act as acceptors in ZnO and hence these dopants have the possibility to produce p-type conductivity. Both the p-type conduction and ferromagnetism in Cu-doped ZnO are controversial. In this chapter, the switching behaviour of Cu charge states and the role of Cu centres on the optoelectronic properties of ZnO are investigated.

5.1. Introduction

Cu is a commonly incorporated impurity up to the ppm level in II-VI semiconductors such as ZnS, ZnO and CdS and is known to form acceptor states within the bandgap. A large amount of work on Cu-doped ZnO exists concerning various aspects of its acceptor states and their possible role in green luminescence mechanism [20, 68, 193]. Cu dopants have also been theoretically predicted to favour spin polarisation and hole mediated ferromagnetism in ZnO-based diluted magnetic semiconductors [194]. Room temperature ferromagnetism of Cu-doped ZnO has been reported by different groups [17, 18], conversely the lack of ferromagnetism in some samples was also confirmed by other workers [19]. These inconsistent results highlight the fact that the nature of Cu acceptors in ZnO and its role in the optical and magnetic properties is highly controversial.

This work is aimed to investigate the switching behaviour of Cu charge state in ZnO nanorods by Ga doping. This switching behaviour of the Cu charge state could account for the often-contradictory interpretations of the luminescence and ferromagnetism properties of Cu-doped ZnO. To elucidate and predict the carrier mediated conversion of the Cu charge state in ZnO, several optical measurements and simulation of the characteristic Cu-related green luminescence band in ZnO nanorods fabricated the vapour phase transport method were performed. This growth method enables the manipulation of the electronic structure of ZnO nanorods by uniformly introducing Ga dopants substitutionally on Zn sites during the growth. The spectral simulation of the Cu-related GL enables the determination of the ZPL and phonon coupling strength of the Cu luminescence centre in ZnO.

5.2. Cu impurities in ZnO nanorods

Figure 5.1 (a) shows a secondary electron SEM image of Gallium doped ZnO nanorods containing 0.15 ± 0.06 at% Ga. Nearly all the nanorods are aligned along the (002) plane perpendicular to the substrate and possess hexagonal tip facets, indicating the nanorods are single crystal wurtzite. The nanorods typically have diameters of ~130 nm and lengths of ~ 450 nm. EDX elemental mapping was used to qualitatively evaluate the spatial uniformity of distributions of Ga and Zn in the nanorods. The EDX maps in Figure 5.1 (b) show uniform distribution of Ga and Zn along the Ga-doped ZnO nanorods.

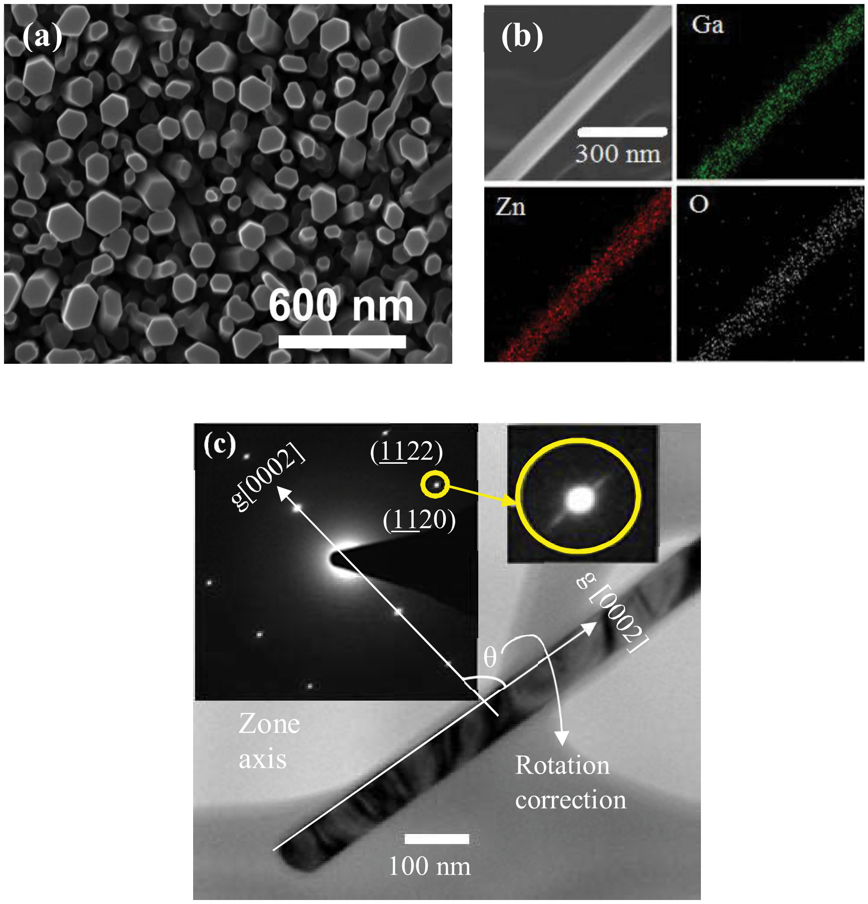

Figure 5.1 (a) A typical secondary electron SEM image of 0.15 at% Ga-doped ZnO nanorods showing vertically aligned nanorods with hexagonal well-faceted cross-section. (b) SEM image of an isolated nanorod which has been extracted from the substrate and its corresponding EDX elemental maps showing a generally uniform spatial distribution of Ga along the nanorod length. (c) TEM image 200 kV of a single Ga-doped ZnO nanorod and its corresponding indexed SAED patterns (inset). The diffraction streaks that extend in the direction perpendicular to the $g_{[0001]}$ reciprocal lattice vector confirms that the Ga-doped ZnO nanorod is grown along the *c*-axis orientation.

The crystal structure and orientation of the nanorods were also confirmed by SAED in a TEM. A typical TEM bright field image and SAED pattern of an isolated Ga-doped ZnO (001) nanorod are shown in Figure 5.1 (c). The dark bands in the TEM image are due to bend contour contrast arising from strain along the length of the Ga-doped ZnO nanowire while the high quality SAED patterns confirm the single-crystal nature of nanorods. The diffuse streaks seen superimposed on the Bragg diffraction spots that extend in the direction perpendicular to the g<0001> reciprocal lattice vector, shown in the zoomed-in image in the inset, confirms that the nanorod is oriented along the c axis.

Figures 5.2 (a) and (b) show the LA-ICP-MS spectra of undoped and Ga-doped ZnO nanorods. The raw signals for Ga, Cu and Zn were collected from a 100 μm diameter ablation crater in both undoped and Ga-doped ZnO samples where each point is the mean of 2 sweeps. Each sweep was run at 100μm/s with a laser fluence of 4.35J/cm^2 with a 35s laser warm up time followed by 10 s of wash out time to allow the signal drop to background values. The instrument was tuned to maximise signals for the Ga, Zn and Cu. The several undoped and Ga doped samples have been examined by LA-ICP-MS. NIST SRM 610 and 612 (National Institute of Standards and Technology, Gaithersburg, MD) were used to quantify the elements analysed by LA-ICP-MS [195]. The LA-ICP-MS analysis reveals a Cu concentration of ~ 30 ppm in both undoped and Ga-doped nanorods using the NIST 610 and 612 standard reference materials.

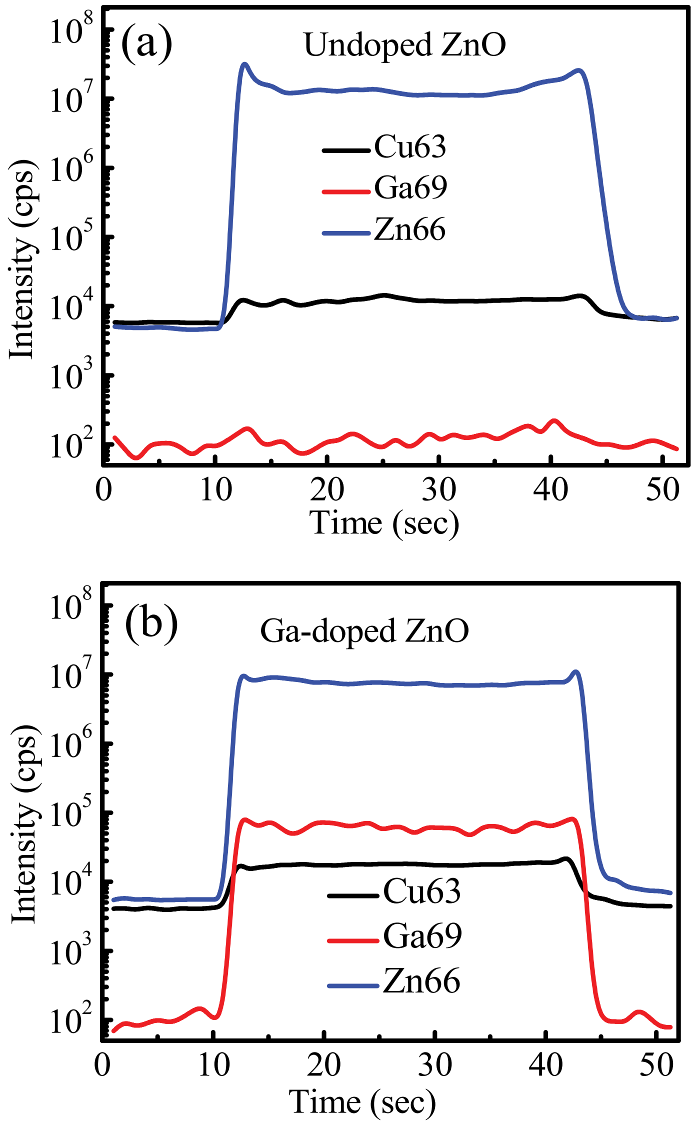

Figure 5.2 Time-dependent LA-ICP-MS spectra for (a) undoped and (b) Ga-doped ZnO nanowires showing the presence of Cu impurity in both undoped and Ga-doped ZnO nanorods.

The XRD patterns of undoped and Ga-doped ZnO nanorods are shown in Figure 5.3. The XRD peaks were found at 2θ = 31.88˚, 34.5˚, 36.32˚ and 47.64˚, which corresponding to the (100), (002), (101) and (102) crystallographic reflections, respectively for a hexagonal wurtzite ZnO. The lattice parameters are found to be a = 0.3244 nm and c = 0.5212 nm for undoped ZnO nanorods. No significant change of lattice parameters has been observed in the doping range of 0.15 - 0.4 at% Ga. The intensity of (002) peak is much stronger than other diffraction peaks. This result indicates that ZnO nanorods are preferably grown along the c-axis. No typical diffraction peaks corresponding to tetragonal Ga_2O_3 and cubic $ZnGa_2O_4$ phases are observed, indicating the formation pure hexagonal wurtzite structure of Ga-doped ZnO nanorods.

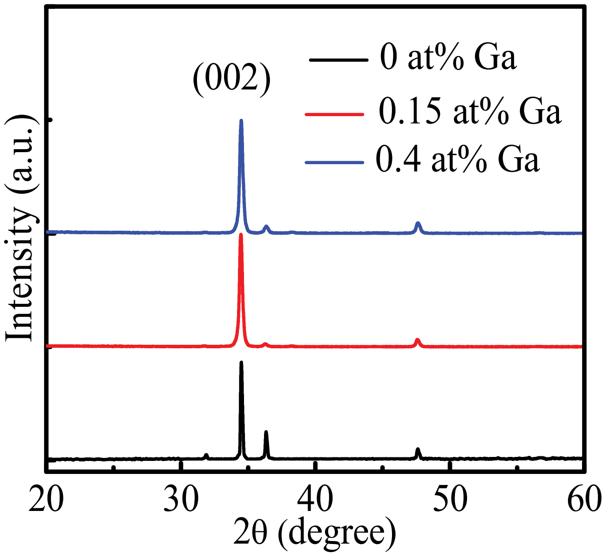

Figure 5.3. XRD patterns of the undoped and Ga-doped ZnO nanorods showing the preferential growth along (0002) orientation perpendicular to the substrate. The (101), (102) and (110) reflections are significantly weaker.

Figure 5.4 shows the Raman spectra of undoped and 0.4 at% Ga-doped ZnO nanorods. Both undoped and Ga-doped ZnO nanorods show 217, 301, and 437 cm^{-1} peaks. The dominant peak at 437 cm^{-1} is assigned to E_2^{high} mode, which is the active Raman mode in ZnO. The other peaks at 217 and 303 are assigned to E_2^{low} and $E_2^{high} - E_2^{low}$ modes, respectively. The intense Raman E_2^{high} mode is the signature of hexagonal wurtzite ZnO. The intensity of the E_2^{high} peak significantly enhances after Ga doping, indicating an improvement of crystal quality in ZnO nanorods. The higher crystallinity of the Ga-doped ZnO nanorods is attributed to the occupation of V_{Zn} defects by the substitutional Ga donors, which have a similar ionic size to the Zn^{2+} host cations [196].

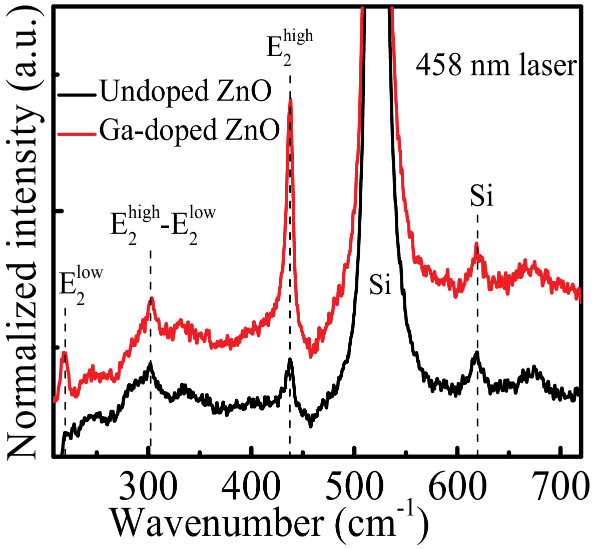

Figure 5.4. Raman spectra for undoped and Ga-doped ZnO nanorods, showing a substantial increase in the E_2^{high} mode after the Ga doping.

5.3 Luminescence of Cu acceptors mediated by Ga doping

5.3.1. Optical characteristics of Ga donors in ZnO

The near-band-edge PL spectra of the ZnO nanorods show free exciton (FX) and bound exciton (D^oX) emissions at 3.381 and 3.365 eV, respectively, together with their corresponding longitudinal optical (LO) phonon replicas (Figure 5.5 (a)). Figure 5.5 (b) shows high-resolution PL spectra with well-resolved bound exciton lines I_4 (due to H impurities) and I_6 (due to Al) [23]. For the Ga-doped nanorods, the NBE emission is dominated by the I_8 line at 3.364 eV attributed to excitons bound to neutral Ga_{Zn} donors [197]. I_1 has been assigned to ionized-Ga donor bound exciton [94]. These well-resolved free and bound excitonic emission lines suggest that the Ga-doped nanorods remain non-degenerate. Additionally, the strong I_8 line indicates that the Ga dopant atoms are incorporated in the nanorods by substituting Zn in the ZnO lattice.

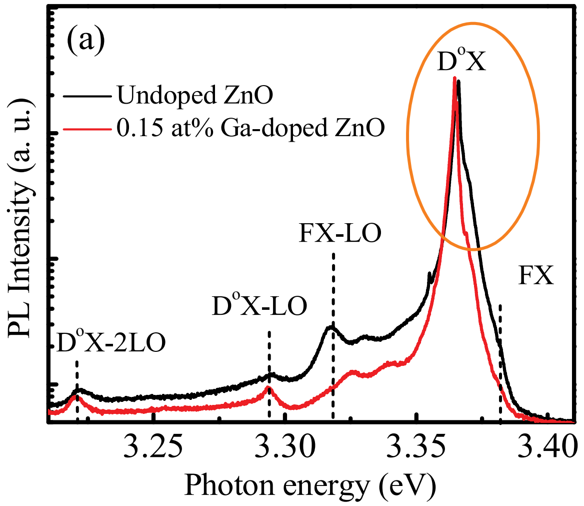

Figure 5.5. (a) Near-band-edge PL spectra of undoped and Ga-doped ZnO nanorods at 6K showing free exciton and bound exciton emissions.

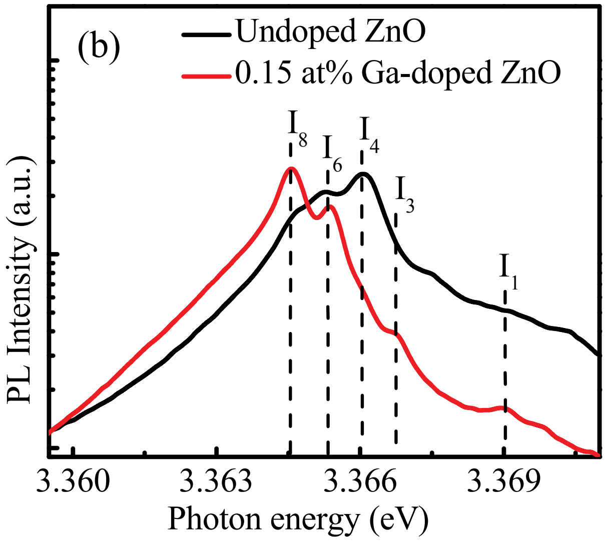

Figure 5.5. (b) Enlarged view of donor bound excitons (yellow circles in Figure 5.5 (a)) showing I_1 and I_8 lines which corresponding to the Ga_{Zn} donors as presented in the chapter 2.

5.3.2. Activating Cu acceptors in ZnO by Ga doping

The deep-level PL spectra of the undoped and Ga-doped ZnO nanorods at 6 K are depicted in Figure 5.6 (a). Comparison of the nanorods PL spectra before and after the Ga doping reveals: (i) the fine structured doublets emerges, with an energy spacing equal to the longitudinal optical phonon energy E_{LO} = 72 ± 3 meV, and (ii) the GL peak is red shifted by ~ 50 meV after 0.15 at% Ga doping. The symmetrical, unstructured GL band centred at 2.45 eV in undoped ZnO is attributable to zinc vacancies (V_{Zn}) [44]. The Ga-doped ZnO nanorods exhibit a sharp ZPL peak at 2.874 eV and a series of doublets whose energy positions match, within the experimental error of ± 20 meV, those reported in the literature for bulk Cu-doped ZnO [21] (see Table 5.1), indicating that the Ga doping activates Cu luminescence centres in the Ga-doped ZnO nanorods. The slight variations in the exact peak positions could also be due to tensile strain in the ZnO nanorods [198].

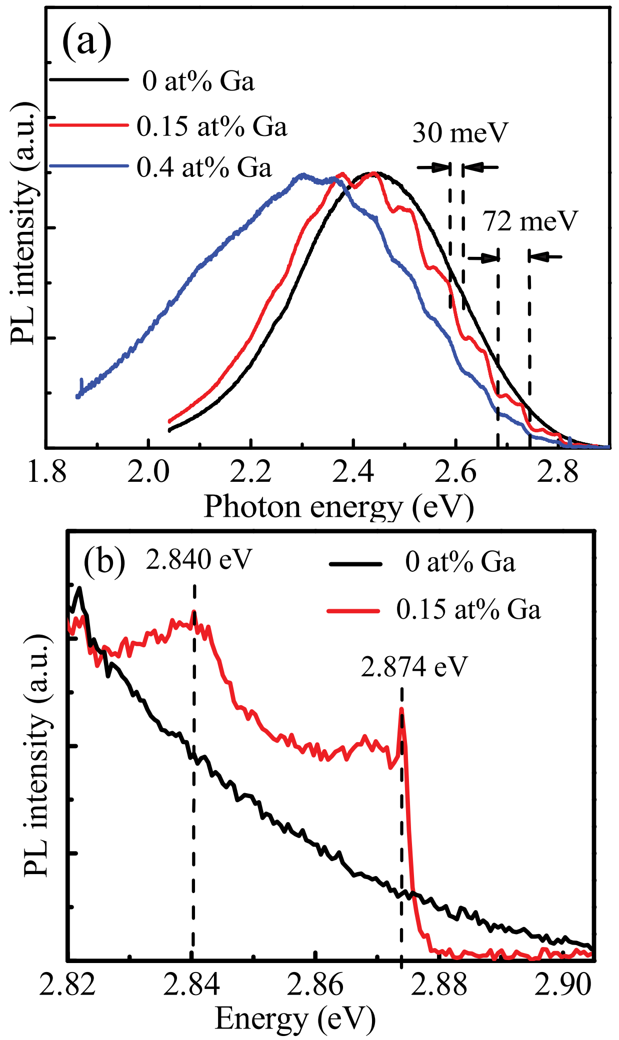

Figure 5.6. (a) Deep level emission of PL spectra for Ga-doped ZnO shows doublet fine structures with 72 ± 3 meV periodicity after Ga doping. The spacing of the doublet features is 30 ± 3 meV. (b) The sharp zero phonon lines at 2.874 and 2.840 eV.

Table 5.1. Peak energies of the zero-phonon lines and their replicas in ZnO bulk and nanorods. The doublet spacing is $a - b = 30 \pm 3$ meV and the LO-phonon replica separation is $a - a$ or $b - b = 72 \pm 3$ meV.

Line name	**ZPL-0a**	**ZPL-0b**	**1a**	**1b**	**2a**	**2b**
Cu-doped ZnO film (eV) (Ref [21])	2.8559	2.8245	2.7798	2.7565	2.7118	2.6840
Ga-doped ZnO nanorods (eV) (this work)	2.8739	2.8404	2.8003	2.7690	2.7271	2.6974

Line name	**3a**	**3b**	**4a**	**4b**	**5a**	**5b**
Cu-doped ZnO film (eV) (Ref [21])	2.6436	2.6218	2.5710	2.5446	2.5042	2.4808
Ga-doped ZnO nanorods (eV) (this work)	2.6541	2.6239	2.5839	2.5558	2.5100	2.4875

The most plausible explanation for the activation of Cu luminescence centres is the conversion of the Cu acceptor charge state from Cu^{2+} to Cu^{+} as the Fermi level is raised above the 0/- (Cu^{2+}/Cu^{+}) charge transfer level (located at 180 meV below the conduction band minimum) [20]. In the Ga-doped ZnO nanorods, the activated Cu^{+} centres provide the dominant recombination pathway, while the V_{Zn}-related GL emission is quenched as a result of Ga occupation at V_{Zn} sites. It is worth noting that the carrier concentration in these ZnO nanorods is expected to be several orders of magnitude lower than that in degenerate Ga-doped ZnO films ($n > 10^{20}$ cm^{-3})

[199]. Thus, the self-compensation effect by lowering the formation energy of V_{Zn} would be less pronounced in this case.

For non-degenerate ZnO nanorods, which are large enough to avoid quantum size effects, the carrier concentration can be estimated by [200]:

$$n = 2(m_e kT/2\pi\hbar^2)^{3/2}\exp[(E_f - E_c)/kT] \tag{5.1}$$

where m_e is the electron effective mass, E_f and E_c are the Fermi energy and conduction band minimum, respectively. The other symbols have their usual meaning. In order to activate the Cu^+ luminescence centre, the Fermi level must lie above the $Cu^{2+}(A^o)/Cu^+(A^-)$ (0/-) charge transfer level (CTL), which requires the carrier concentration in ZnO to be at least 6.2×10^{17} cm^{-3}. This value is calculated from equation (5.1) with $m_e = 0.29m_o$ (m_o is the rest mass) [201]. The Fermi level shift due to the Ga doping is confirmed by valence-band X-ray photoemission spectroscopy, showing an upward shift of 0.19 eV due to the Ga doping (see the section 5.4). The carrier concentration required for the Cu^+ activation is significantly lower than the value expected for ZnO doped with 0.15 at% Ga; however, at 6 K, most Ga donors are in the neutral state, as evidenced by the fact that the PL spectrum of the Ga-doped nanorods (see section-5.3.1) is dominated by the neutral-Ga donor bound I_8 rather than ionized-Ga donor bound I_1. Formation of acceptor-like defects due to self-compensation could also contribute to a reduction in electron concentration [88]. This result provides a physical picture of the structured GL in the Ga-doped nanorods: the Cu^+ state is stabilized by the rise in the Fermi level and can readily trap free holes from neighbouring oxygen atoms by the potential created by the additional electron in the ionized acceptor $Cu^+(3d^{10})$ state [109], which gives rise to the structured GL. The doublets in the Cu-related structured GL (with an energy spacing of 30 ± 2 meV, see Table 5.1) are due to the two kinds of energetically different holes that are transferred from the orbitals surrounding the oxygen atom to the 3*d* shell of copper [21]. The change in the chemical origin of the GL from V_{Zn} to Cu centres also accounts for the observed red shift in the GL before and after Ga doping. Further support for these assignments comes from the temperature dependence of the energetic positions for the structured and structureless GL bands (See section 5.3.3). The ZPLs and their phonon replicas of the structured GL remain unchanged in position with increasing temperature, characteristic of an internal transition within Cu centres.

5.3.3. Temperature dependence of Cu-related emission

The temperature dependent CL spectra of undoped and 0.15 at% Ga-doped ZnO nanorods are shown in Figure 5.7 (a)-(b). The undoped ZnO shows a symmetrical GL band in the temperature range of 10-135 K. As shown in Figure 5.7 (b), the fine structure in the GL band is gradually faded and disappeared after 85 K. This result indicates that the Cu luminescence centre active below 85 K temperature. The vertical line indicates the energetic position of the 6th phonon replica. The ZnO GL peak broadens and shifts to lower energy with increasing temperature attributed from the band shrinkage effect, whereas the position of the 6a line in Ga-doped ZnO remains unchanged at 2.420 eV (Figure 5.7 (c)). This result confirms the GL band in the Ga-doped nanorods originates from an internal transition in Cu centres.

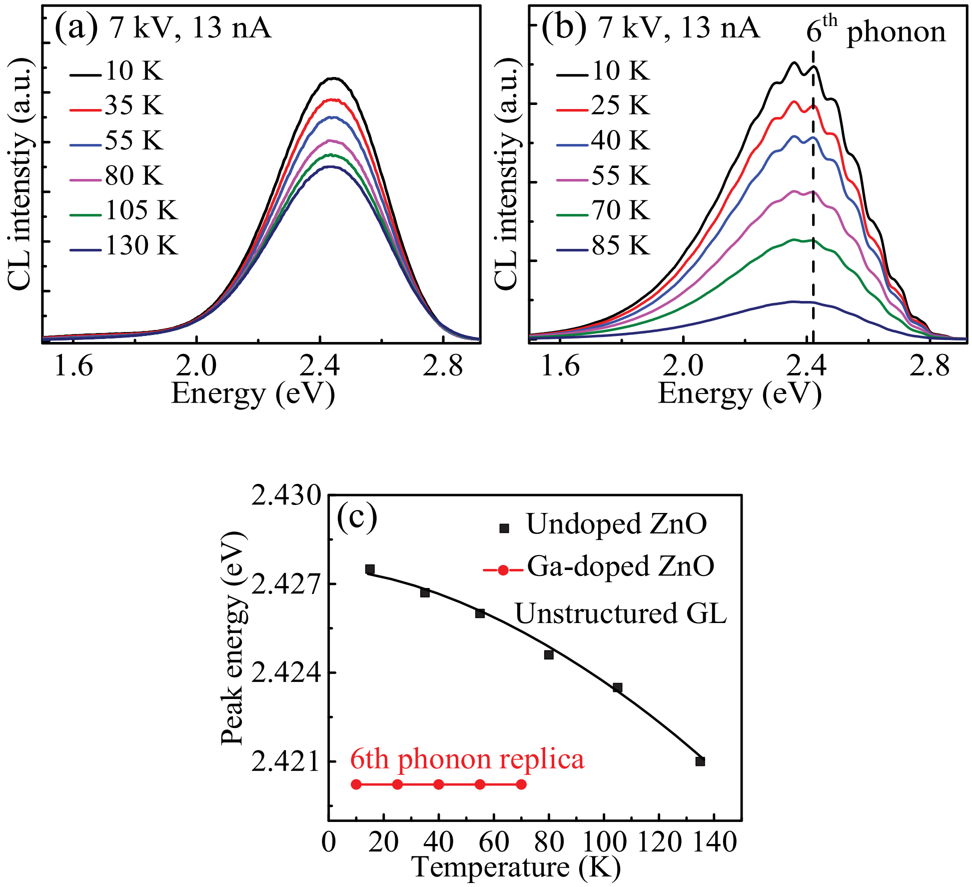

Figure 5.7. Temperature-resolved CL spectra of (a) undoped ZnO showing the symmetrical GL emission and (b) Ga-doped ZnO nanorods showing the structured GL band up to 70 K. (c) Peak positions of the ZnO GL band and the 6th phonon replica of the Ga-doped ZnO nanorods.

5.3.4. Kinetics of radiative recombination at Cu acceptors

To study the kinetic nature of the Cu-related GL band in the Ga-doped ZnO nanorods, this emission spectra were examined by the excitation power dependent CL measurements. In these measurements, the electron beam current was varied from 0.14 to 75.3 nA, while the accelerating voltage was kept constant at 7.5 kV

(Figure 5.8 (a)). The excitation power-dependent CL integrated intensities of Cu-related GL (Figure 5.8 (b)) are determined from Gaussian fitting. The parameters used in this fitting process are peak position, E_{GL} = 2.40 ± 0.03 and FWHM = 0.51 ± 0.03 eV. The integrated intensities (I_{CL}) agree with the power law ($I_{CL} \alpha P_b^n$), where P_b is the CL excitation power [173]. The value n is found to be 0.9 ± 0.02 for the Cu-related GL band in the Ga-doped ZnO nanorods. The index n $(= 0.72)$ for undoped ZnO has already been determined in the chapter 4 section 4.3.2. The structured GL possess slower saturation rates (higher n values) in ZnO.

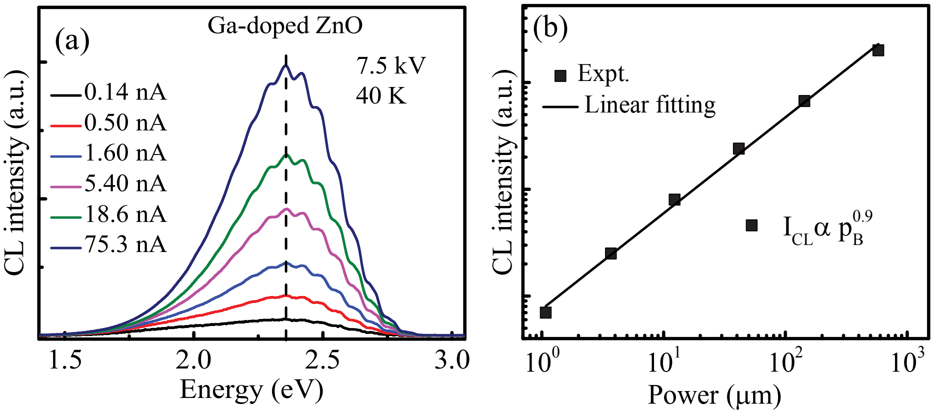

Figure 5.8. (a) CL spectra of structured green emission band of Ga-doped ZnO nanorods at different electron beam currents. (b) Log-log plots of the CL integrated intensities Cu-related GL emission at 10 K as a function of CL excitation power. The solid lines are the least square fitting of the power law ($I_{CL} \alpha P_b^n$) to the experimental CL data.

5.3.5. Depth-resolved characteristics of Cu acceptors

To study the distribution of Cu luminescence centres along the length of Ga doped ZnO nanorods. The depth-resolved CL spectra of Cu-related GL have been measured. In these measurements, the accelerating voltage was varied, while the electron beam current was adjusted to maintain the excitation power constant. Figure 5.9 (a) shows the CL spectra of structured green emission band of Ga-doped ZnO nanorods at different accelerating voltages. In this work the spectra were collected with a fixed power of 6 μW, while the accelerating voltage was changed from 2 to 15 kV, corresponding to the CL generation depth from 40 - 1600 nm as deduced by Monte Carlo stimulation CASINO [186].

Figure 5.9 (b) shows the CL integrated intensity as a function of accelerating voltages. No significant changes in the peak position and CL intensity with increasing accelerating voltage up to 8 kV corresponding to the 500 nm length of the nanorods, indicating that Cu impurities are uniformly distributed along the entire length of the Ga-dopped ZnO nanorods. It is observed that the CL integrated intensity of the structured GL emission decreases after 8 kV accelerating voltage. The decrease in intensity of the structured GL emission above 8 kV also indicates that the Cu luminescence centres are located within a 500 nm depth, which corresponding to the length of the nanorods.

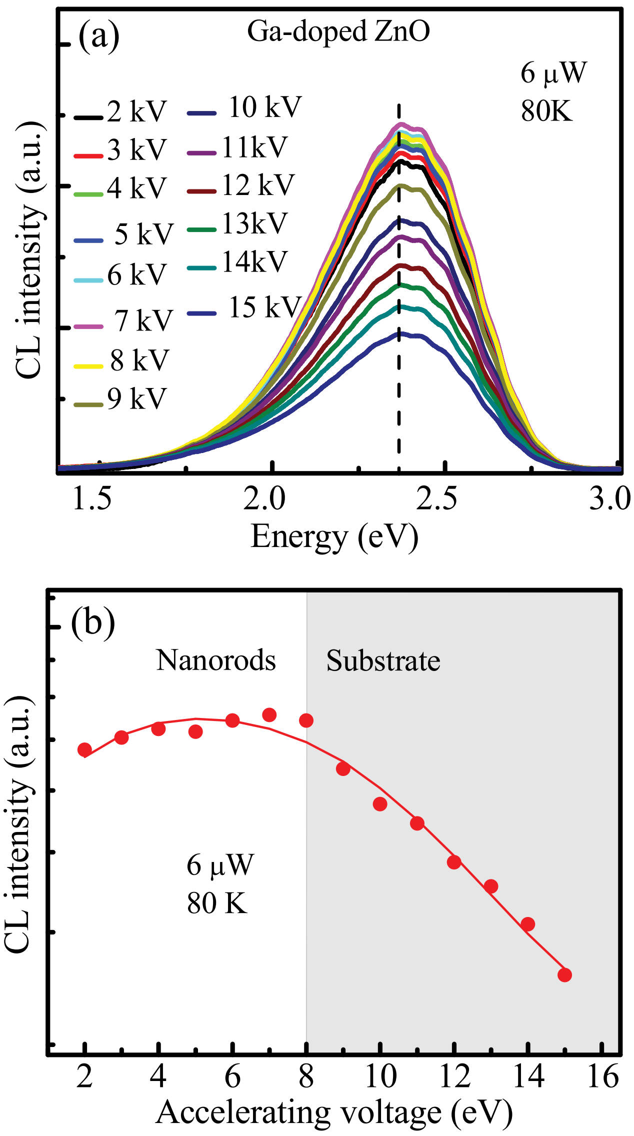

Figure 5.9. (a) CL spectra of structured green band of Ga-doped ZnO nanorods at different accelerating voltages. (b) Variation of CL integrated intensities of Cu-related green emissions as a function of accelerating voltages showing no significant changes CL intensity up to 8 kV, corresponding to the 500 nm length of the nanorods.

5.4. Valence band structure of Ga-doped ZnO nanorods

The valence band spectra of undoped and Ga-doped ZnO nanorods are presented in Figure 5.10 (a). The valence band spectra show three peaks at 10.85, 8.11 and 5.22 eV in both undoped and Ga-doped ZnO nanorods attributed to Zn 3d, mixed Zn 4*s*–O 2*p*, and O 2*p* states, respectively [202]. The use of the X-ray source minimizes surface band bending effects. The zero of the binding energy scale (E_F) is referenced to the Fermi edge of a clean Au gold in electrical contact with the spectrometer.

The occupancy of the Zn 3*d* state is not expected to change upon the Ga doping, thus the spectra are normalized to the Zn 3*d* peak at 10.85 eV binding energy. In the Figure 5.10 (b), the onset of valence band photoemission obtained from linear extrapolation of the leading edge of O 2*p* states are 3.13, 3.21 and 3.32 eV for the 0 at%, 0.15 at% and 0.4 at% Ga-doped ZnO nanorods, respectively. The bandgap is unchanged for low Ga doping concentration (see at the end of current section for bandgap analysis), the increase in ($E_F - E_V$) indicates that the Fermi level is raised towards the conduction band after the Ga doping.

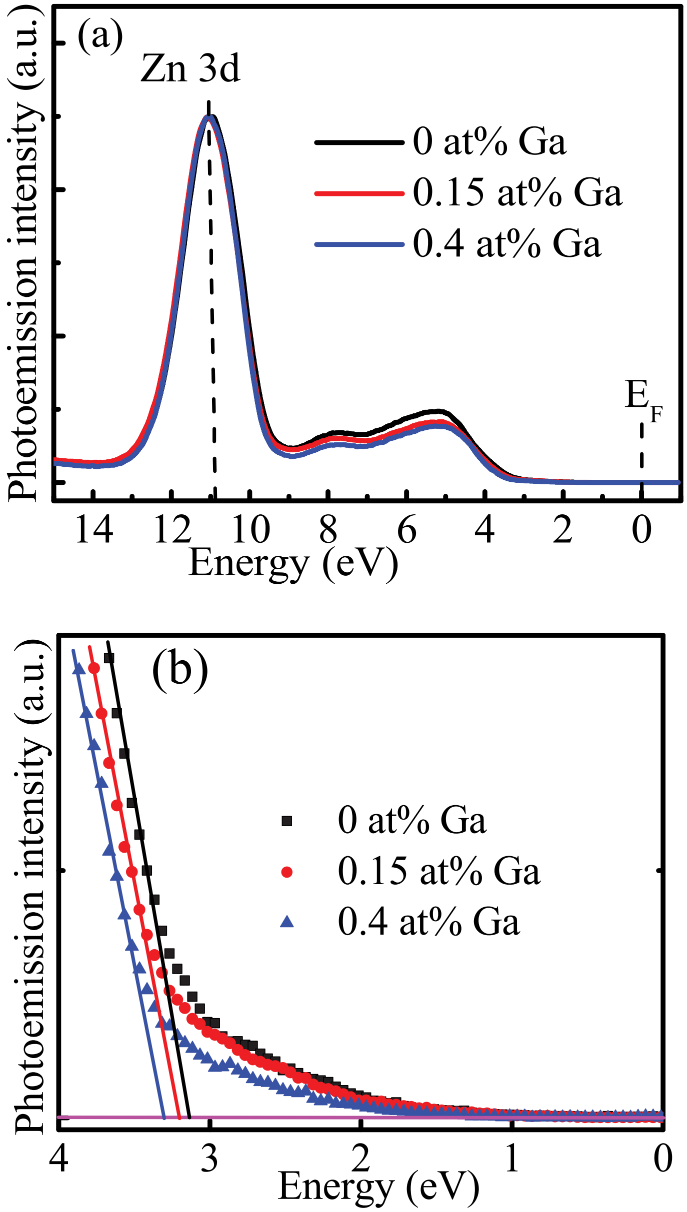

Figure 5.10. (a) Valence band spectra of the undoped and Ga-doped ZnO nanorods acquired using synchrotron radiation X-ray Photoelectron Spectroscopy. The onset of valence band photoemission extracted from linear extrapolation of the leading edge of O 2*p* states are 3.13, 3.21 and 3.32 eV for the undoped, 0.15 at% and 0.4 at% Ga-doped ZnO nanorods

The position of the Fermi level (E_F) for a nondegenerate ZnO is located below the conduction band minimum (E_c). The work function (φ) is the energy separation between the E_F and vacuum level (E_{vac}), while the ionisation energy is the difference between the valence band (E_v) and E_{vac}. The work function can be measured from the photoelectron yield spectroscopy. With the influence of the surface state, the work function can be expressed as;

$$\varphi = E_{vac} - (E_c + E_F) \tag{5.2}$$

For non-degenerate semiconductor, the $E_F - E_c$ is related to the carrier concentration (n) by the following relation [200]:

$$E_F - E_c = kT \ln\left(\frac{n}{N_c}\right) \tag{5.3}$$

where $N_c \left[= 2\left(\frac{2\pi m_e^* kT}{h^2}\right)^{3/2} = 3.91 \times 10^{18}\ cm^{-3}\right]$ is the effective density of state in the conduction band and m_e^* $(= 0.29\ m_o$ for ZnO [203]) is the effective mass of the electron and other symbols have their usual meaning.

The work function has a linear relationship with carrier density. Figure 5.11 shows photoelectron emission spectra at different Ga doping concentrations. The onset energy of the photoelectron emission intensity clearly exhibited a shift to the lower energy side with Ga doping in ZnO nanorods. The shift of the work function is mainly related to the increase of carrier concentration caused Ga doping in ZnO nanorods. This result clearly indicates that the Ga doping shifts the Fermi level toward the conduction band maximum.

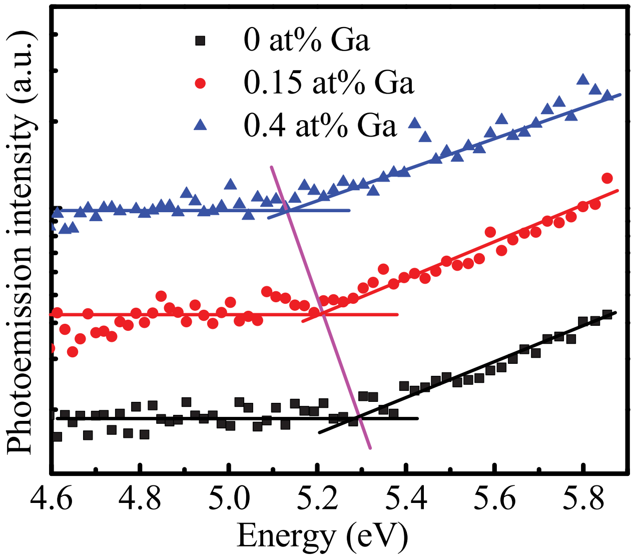

Figure 5.11. Photoemission yield spectra of Ga-doped ZnO nanorods at different Ga doping concentrations. The threshold energy for the photoelectron emission decreases with Ga-doping concentration.

Figures 5.12 (a) - (b) show the optical transmittance and reflectance spectra for Ga-doped ZnO nanorods at different Ga doping concentrations. The undoped ZnO is highly transparent in the infrared region, while the transparency decreases, and reflectance increases with Ga doping concentration. The Ga-doped ZnO show increased transmittance, simultaneously decreasing the reflectance in the visible and near infrared regions. The optimum transmittance for Ga-doped ZnO is 92% in the near infrared region (around 975 nm). In a transparent oxide material, the crystal orientation and zinc to oxygen ratio determine the transparency. The high transparency indicates that the nanorods possess excellent structural homogeneity and crystallinity. Both the undoped and Ga-doped ZnO nanorods show a sharp fall of transmittance in the ultraviolet region due to the onset of the fundamental absorption edge. Both undoped and Ga-doped ZnO nanorods show a dip at 600 nm is attributed to plasmonic absorption of Au nanoparticle catalyst.

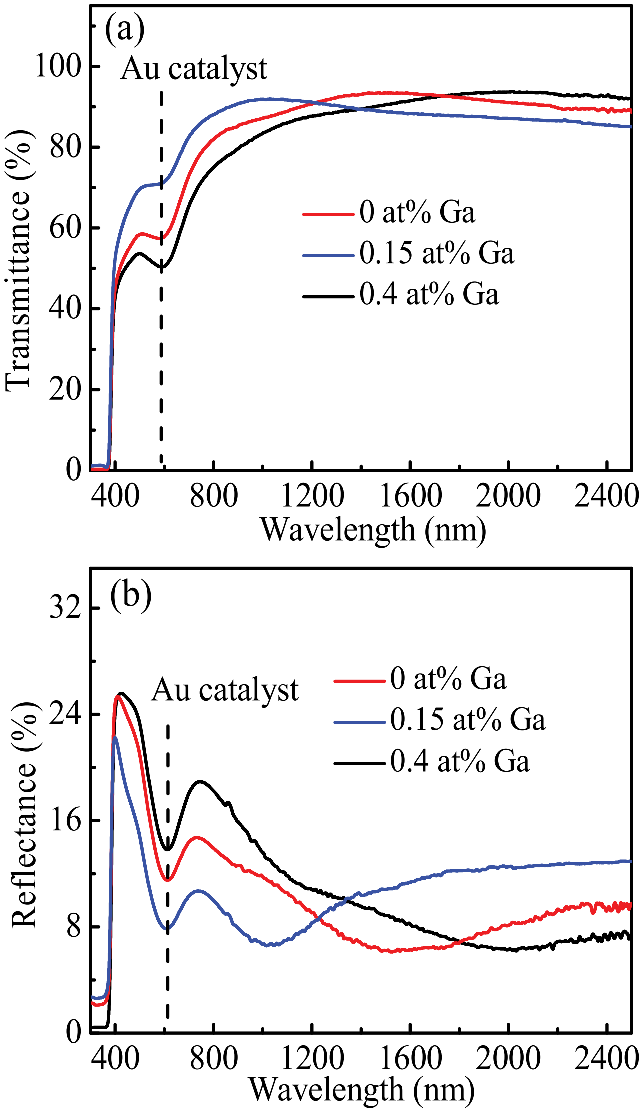

Figure 5.12. (a) Transmittance and (b) reflectance spectra of Ga-doped ZnO nanorods at different Ga doping concentrations. The undoped ZnO showing the maximum transmittance in the infrared region, while the Ga-doped ZnO exhibiting the optimum transmittance in the visible and near infrared spectral region.

This absorption edge corresponding to the excitation of electron from the valence band to conduction band. The optical bandgaps of undoped and Ga-doped ZnO nanorods are determined from the transmittance and reflectance data. The absorption coefficient (α) can be expressed in terms of the transmittance and reflectance as [182];

$$\alpha = (1/l)\, ln[(1-R)^2/T] \tag{5.4}$$

$$\alpha h v = A(hv - E_g)^m \tag{5.5}$$

where A is a constant, E_g is the bandgap and l the length of the nanorods. The exponent, m, determines the type of transition. The values of m = 1/2 and 2 correspond to the allowed direct and indirect bandgaps, respectively.

Figures 5.13 Tauc's plots for the determination of direct bandgap. The bandgap is determined from the extrapolation of the linear portion of the curves to hv axis. The intercept on the hv axis gives the bandgap. As shown in Figure 5.13, the bandgap is unchanged with 0.4 at% Ga doping into ZnO nanorods. This is because the ZnO nanorod remains nondegenerate up to this doping concentration. Ginting et al. reported that the bandgap of ZnO is not significantly changed up to 3 at% Ga doping concentration in the nanowires [96].

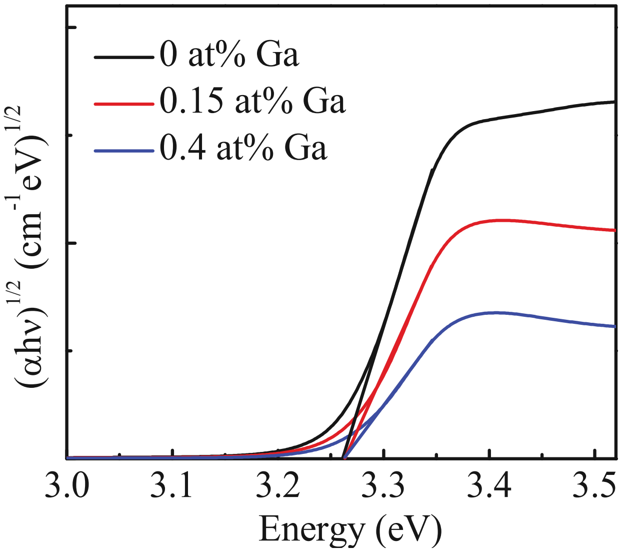

Figure 5.13. Tauc's plots for the determination of direct bandgap of undoped and Ga-doped ZnO nanorods showing unchanged bandgap after 0.4 at% Ga doping.

5.5. Cu-related emission in ZnO nanorods

To investigate the nature of the Cu luminescence centres responsible for the structured GL, the emission band was simulated using a multimode Brownian oscillator (MBO) model [204], in which the electronic transitions between the Cu ground and excited states was examined. The variables used in the MBO model are: the Huang-Rhys factor (S) that reflects the phonon coupling strength and the coefficient (γ_j) reflects the full width at half maximum of the LO-phonon side band. At $T \rightarrow 0$, the PL intensity according to the MBO model can be expressed as [204]:

$$I_{PL}(\omega) = \sum_{n=0}^{\infty} \frac{S^n \exp(-S)}{n!} \frac{(\gamma_{ZPL}+n\gamma_j)/2\pi}{(\hbar\omega-\hbar\omega_{eg}+n\hbar\omega_{LO})+(\gamma_{ZPL}+n\gamma_j)/2} \quad (5.6)$$

To simulate the GL spectra, a simplified MBO model was adopted. In this model only the LO phonon oscillator ($\hbar\omega_{LO} = 72\ meV$), was considered. The simulated spectra, displayed as solid curves in Figure 5.14, demonstrate the best fits with the following parameters: (i) $\hbar\omega_{eg1} = 2874\ meV$, $\hbar\omega_{eg2} = 2844\ meV$, $\gamma_j = 7.4 \pm 0.3\ meV$, $S = 6.55 \pm 0.04$ for the Ga-doped ZnO nanorods; and (ii) $\hbar\omega_{eg} = 2910\ meV$, $\gamma_j = 8.7 \pm 0.3\ meV$, $S = 6.75 \pm 0.04$ for the structureless ZnO GL. The simulated $\hbar\omega_{eg1}$ and $\hbar\omega_{eg2}$ values are consistent with the energetic positions of the ZPLs for the Ga-doped nanorods shown in Table 5.1. The Huang-Rhys factor of 6.55 for the Ga-doped ZnO GL is consistent with the literature value of Cu-doped ZnO [205]. This value is slightly smaller than the GL coupling strength in ZnO. Taking the ground energy of Cu^{2+} at 180 meV below the conduction band maximum [20], the activation energy of the excited state (Cu^{+}, h) state in the Ga-doped ZnO nanorods can be determined to be 390 meV from the simulated $\hbar\omega_{eg}$values.

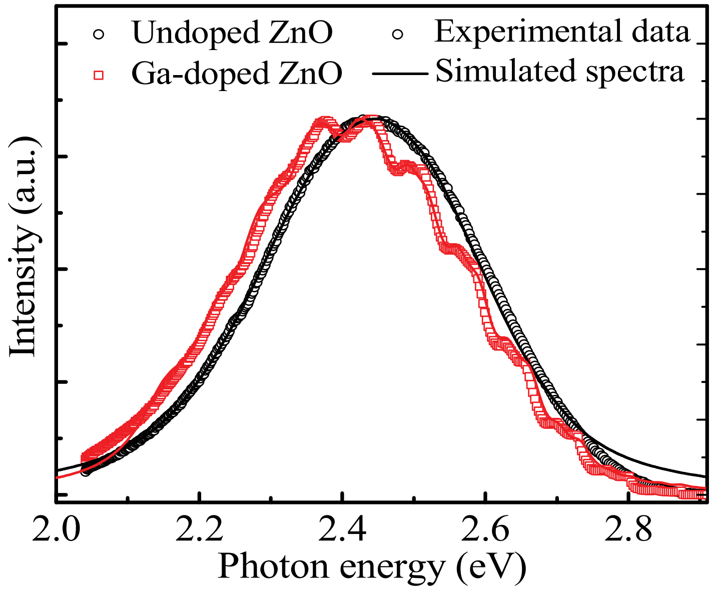

Figure 5.14. Theoretically generated GL bands (solid curves) for the undoped and Ga-doped ZnO nanorods using the MBO model. The open circles represent the measured spectra at 6 K. The best fit to the doublet fine structures in the Ga-doped nanorods is obtained using equation (5.6) with $\hbar\omega_{eg1} = 2874\, meV$, $\hbar\omega_{eg2} = 2844\, meV$ and $S = 6.55$.

Figure 5.15 depicts the electronic transitions involved in the Cu ground and excited states of the Ga-doped ZnO nanorods. With the Fermi level raised by the Ga doping, Cu is in its Cu^{+} state and acts as negatively charged ionized acceptor. This Cu^{+} state captures holes from the neighbouring oxygen, placing it in an excited state, (Cu^{+}, h) and the hole is then transferred to the 3d shell to form Cu^{2+} (3d^{9}). This charge transfer results the structured GL emission in the Ga-doped ZnO nanorods.

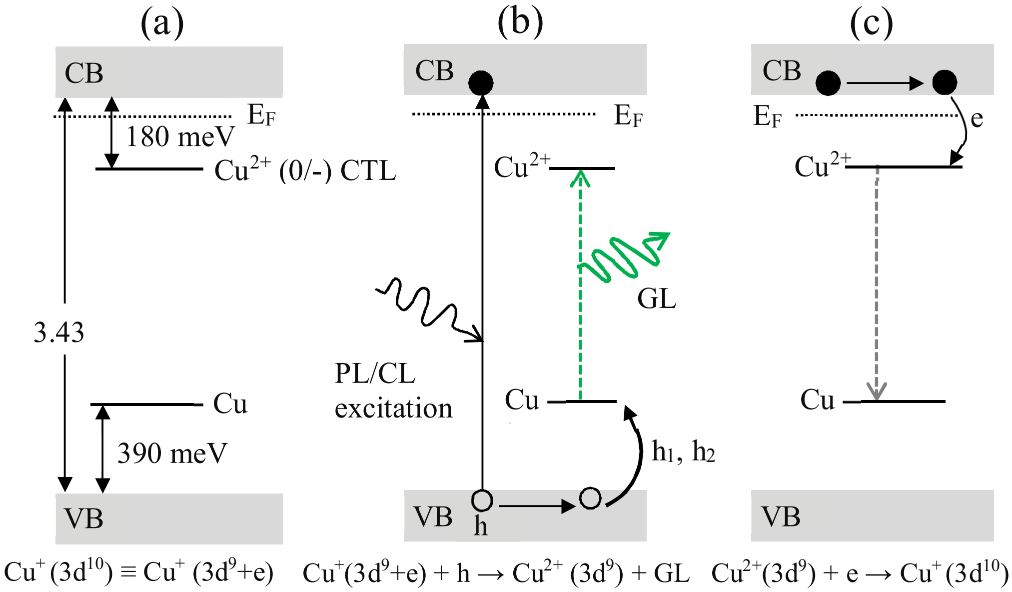

Figure 5.15. Schematic energy level diagram to illustrate the transitions involved between the Cu ground and excited states in Ga-doped ZnO nanorods. (a) Cu is in the Cu^+ ($3d^{10}$) state as the Fermi level is raised above the (0/-) CTL of Cu centres via the Ga donor doping, (b) Holes are captured by $Cu^+(3d^9+e)$ placing it in an excited state, which emits GL and relaxes to the $Cu^{2+}(3d^9)$ ground state, and (c) Cu^{2+} captures a free electron from the CB returning it to Cu^+ state.

5.6. Conclusions

The Ga-mediated switching behaviour of Cu acceptors in ZnO nanorods was studied. Using the vapour phase transport growth, Ga is *in-situ* incorporated substitutionally at Zn lattice sites in nanorods without compromising the crystal quality, producing Ga donor-bound exciton signatures in ZnO. The green luminescence band in Ga-doped nanorods displays a periodic fine structure separated by 72 meV, which consists of doublets with an energy spacing of 30 ± 3 meV. The emergence of the structured GL is due to the Cu^+ state being stabilized by the rise in the Fermi level above the 0/- (Cu^{2+}/Cu^+) charge transfer level as a result of Ga donor incorporation. From a combination of optical characterisation and simulation using the Brownian oscillator model, the doublet fine structures are shown to originate from two hole transitions with the Cu^+ state located at 390 meV above the valence band maximum.

Chapter 6

Bandgap engineering and doping of ZnO microrods

Bandgap engineering is an important strategy for tuning the optical and electrical properties of ZnO semiconductor and provides greater flexibility in designing advanced optoelectronic devices. Bandgap engineering can be obtained by the doping of different impurities into the host lattice. Among the n-type impurities, Ga dopants can improve the optical properties of ZnO, while maintaining its transparency in the visible spectral range for use in light emitting diodes. However, the presence of impurity phases such as Ga_2O_3 and $ZnGa_2O_4$ at high Ga doping levels is a challenging issue. This chapter investigates how the optical properties of ZnO microrods can be tuned by bandgap engineering.

6.1. Introduction

Bandgap engineering is a common practice for tuning the optical and electronic properties of technologically important oxide and nitride semiconductors currently used in a wide range of optoelectronic applications [29, 206]. Among the oxide semiconductors, ZnO can be optimised electrically and optically by the engineering of its bandgap for different technological applications. Various dopants have been used for tuning the bandgap of ZnO such as Mg [207], Cd [208], Be [209], Se [210], transition metals [211] and group III elements [29, 97, 212]. However, compared with ZnO thin films and nanowire ensemble arrays, research on tailoring the bandgap in a single ZnO nano/microrods for the use in practical devices is still at its infancy. Moreover, the physical mechanism responsible for the composition-dependent variation of bandgap is still unclear. Here, tapered ZnO microrods with an increasing Ga doping level gradient from their tip to base with an associated systematic redshift in their near-band-edge emission were grown by a self-catalyst vapour phase transport method. Systematic cathodoluminescence studies of these microrods supported by computational defect simulation are used to explain the Ga doping induced modification of the bandgap.

Among the current n-type dopants, Ga is recognised as one of the most effective dopants for controlling the optical and electrical properties of ZnO [25]. The experimental results indicate that Ga favourably occupies substitutionally the Zn site (Ga_{Zn}), which acts as a shallow donor of 55 meV binding energy [23]. The presence of Ga_{Zn} donors in ZnO produces Ga-bound excitons that show sharp luminescence lines at low temperature known as I_1 and I_8 lines [23, 94]. First principle calculations and experimental measurements have shown the Ga donors interact with acceptor-like defects at high Ga doping levels, producing the abundance of Ga-related defect complexes, especially Ga_{Zn}-O_i and Ga_{Zn}-V_{Zn} pairs in ZnO [24, 79, 88]. The formation of Ga_{Zn}-O_i and Ga_{Zn}-V_{Zn} complexes following compensation by V_{Zn} and O_i defects significantly reduces the band gap and carrier concentration in ZnO [88, 213].

The incorporation of Ga-dopants into the ZnO has shown either blueshift [159, 214] or redshift [28, 29] of the near-band-edge emission with spectral broadening. Different mechanisms have been proposed to explain the broadening of NBE emission at degenerate doping levels such as Burstein-Moss effect [159] and potential fluctuation of an impurity band [215]. In the Burstein-Moss broadening mechanism, the Fermi level is shifted above the conduction band minimum by filling the lower energy levels with electrons. In this case, the band gap energy is increased due to the indirect transition between the conduction band filled states and valence band acceptor states. In the potential fluctuation mechanism, the formation of localised states (band tail) in the bandgap occurs due to randomly distributed impurity ions at the degenerate doping level. These localized states can be regarded as the acceptor-like defects located above the valence band maximum and the wave functions of this impurity band overlap and eventually merge with the valence, results in a decrease of the bandgap [216].

The work in this chapter is aimed to investigate the effect of Ga impurity on the optical band structure of ZnO microrods. ZnO microrods with a graded distribution of Ga were fabricated by a self-catalyst vapour phase transport method at the O-rich condition. The diameter of this microrod varies from 1 to 7 µm from tip to base along the microrod length. As the diameter of the microrod increases from tip to base, the Ga-impurity concentration increases from 1.5 to 6 at% and the CL spectra exhibit a corresponding systematic redshift in the NBE along the microrod length, leading to Ga mediated output emissions. To establish the physical mechanisms associated with the large variation in the CL spectra along the length of the Ga-doped ZnO microrod, a series of correlative experimental analyses probing the chemical composition, crystalline structure, CL spectroscopy at different parts of the microrod were investigated. Density Function Theory (DFT) calculations for the formation of Ga-induced localized defect complexes were also performed to support the experimental results.

6.2. Tapered diameter Ga-doped ZnO microrods

Figure 6.1 (a) shows a typical SEM image of Ga-doped ZnO hexagonal microrods. The diameter of individually tapered microrod varies from 1 - 6 μm from the tip to base along with their length, which ranges from 50 - 150 μm. The decreasing of diameter forms with a series of regular facet along the microrod growth direction accompanied by a number of larger steps with a large reduction in the width of the microrod. The EDS line scans (Figure 6.1 (b), dotted line) across the width of the microrod along its length reveal that the Ga concentration gradually decreases as the diameter of the microrod tapers from base to tip. The Ga concentration ranged from 6 at% at its base to 1.5 at% at its tip.

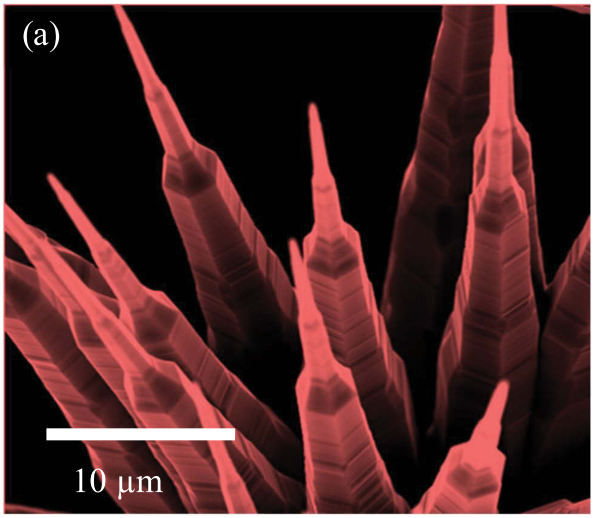

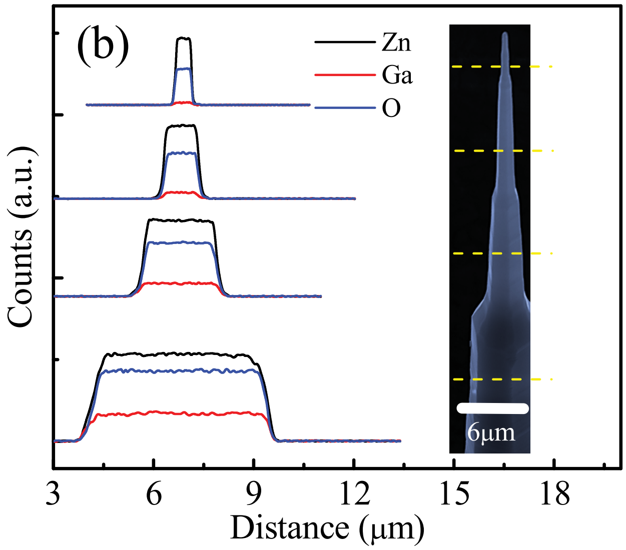

Figure 6.1. (a) A typical SEM micrograph of Ga-doped ZnO microrods displaying hexagonal cross section and the diameter increases from tip to base. (b) EDX spectra from a 5 kV line scan (dotted line) along the diameter from several parts of the microrod. The Ga concentration increases with increasing the diameter of the microrod.

TEM image of a single Ga-doped ZnO microrod acquired at 200 kV and its corresponding indexed SAED patterns from different points of the microrod (Figure 6.2). The diffraction streaks that extend in the direction perpendicular to the $g_{[0001]}$ reciprocal lattice vector confirms that the Ga-doped ZnO microrod is grown along the *c*-axis orientation.

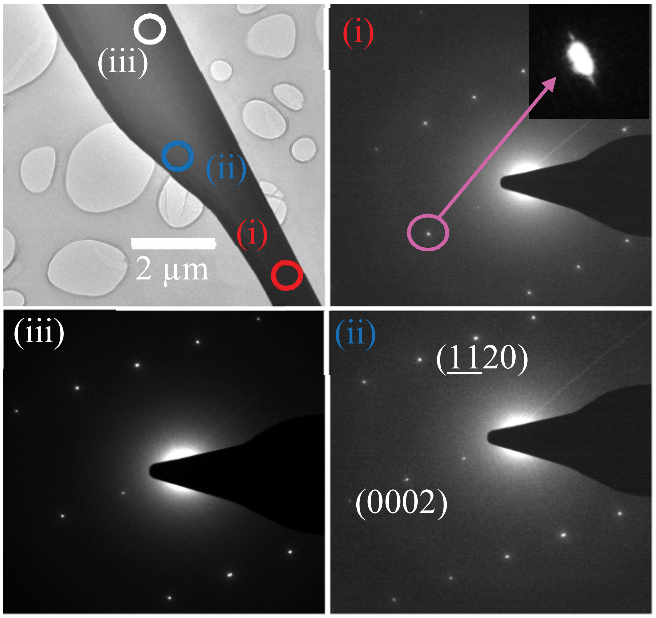

Figure 6.2. TEM image of a single Ga-doped ZnO nanorod acquired at 200 kV and its corresponding indexed SAED patterns from different points of the microrod. The diffraction streaks that extend in the direction perpendicular to the $g_{[0001]}$ reciprocal lattice vector confirms that the Ga-doped ZnO microrods are grown along the *c*-axis orientation.

The crystal structure and orientation of the different parts of the microrod were also confirmed by SAED in a TEM. The SAED patterns from different parts of an isolated Ga-doped ZnO microrod are shown in Figure 6.2 (i) – (iii). The high-quality SAED patterns confirm the single-crystal nature of microrods. The diffuse streaks seen superimposed on the Bragg diffraction spots that extend in the direction perpendicular to the g<0001> reciprocal lattice vector, shown in the zoomed-in image in the inset, confirms that the microrod is oriented along the c-axis. The TEM analysis reveals the similar growth direction in the different parts ((i) to (iii) in the TEM image) of the microrod, indicating unchanged crystallinity of ZnO microrod with increasing diameter and Ga concentration.

6.3. Luminescence properties of lightly Ga-doped ZnO microrod tips

The NBE CL spectra from the tip of a typical individual undoped ZnO microrod reveals the Al-related I_6 bound exciton ($D^\circ X$) emissions at 3.362 eV together with its corresponding longitudinal optical (LO) phonon replicas separated by ~70 meV (Figure 6.3 (a)). The undoped ZnO also shows poorly resolved bound exciton lines I_4 due to H impurities [23]. For the lightly Ga-doped microrods, the NBE emission is dominated by the I_8 line at 3.358 eV attributed to excitons bound to neutral Ga_{Zn} donors as well as an emission centred at 3.32 eV (Figure 6.3 (a)) [23, 94]. An emission line in the 3.30 - 3.32 eV energy range at 9 K in Ga-doped ZnO has previously been assigned to a donor-acceptor pair (DAP) due to a transition between neutral Ga_{Zn} donors to neutral V_{Zn} acceptor or other acceptor complexes [94]. The presence of the strong I_8 and I_{DAP} lines confirms that the Ga dopants are incorporated in the microrods by substituting Zn in the ZnO lattice.

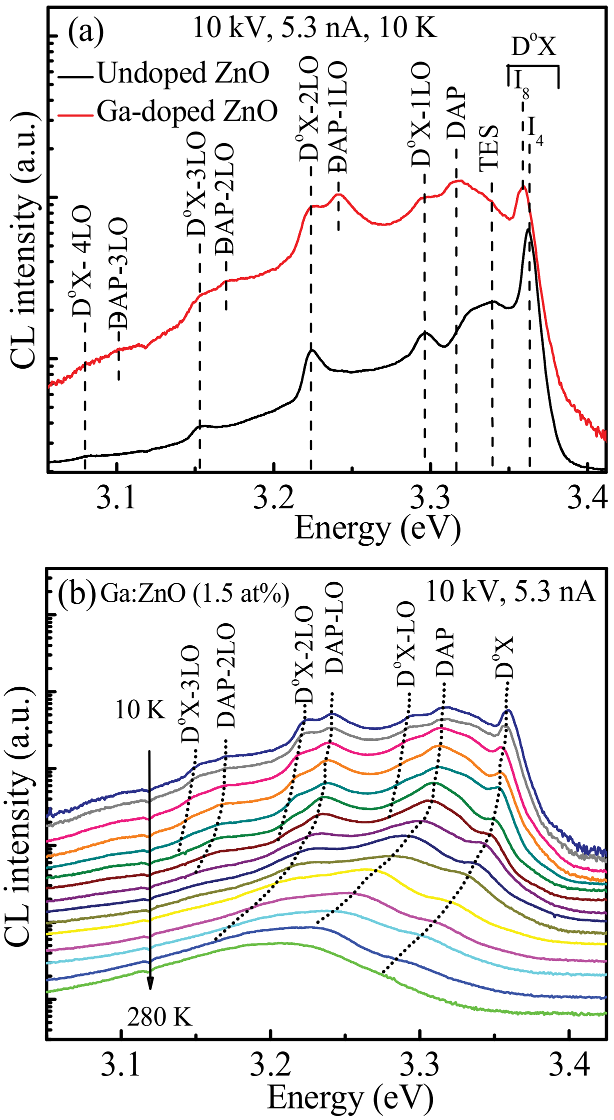

Figure 6.3. (a) NBE CL spectra collected at 10 K from the tip of an individual undoped and lightly Ga-doped ZnO microrod showing I_4 and I_8 line corresponding to the H and Ga impurities, respectively. (b) Temperature-dependent NBE CL spectra of individual Ga-doped ZnO microrod. DAP band showing a ~90 meV redshift when the temperature increases from 10 to 280 K.

The temperature-dependent NBE CL spectra collected from the tip of an individual Ga-doped ZnO microrod is illustrated in Figure 6.3 (b). The temperature-dependent DAP transitions energies are expected to shift in two different ways: (i) a blue-shift attributed to thermalization of Ga donors and (ii) a red-shift due to band gap shrinkage. As shown in Figure 6.3 (b), the I_{DAP} emission peak exhibit overall shift of 90 meV in the 10 - 280 K temperature range in Ga-doped ZnO microrod. Although the quantitative analysis is difficult for this small shifting, the qualitative behaviour of I_{DAP} is consistent with reported DAP recombination model [94].

6.4. Bandgap engineering in heavily Ga-doped ZnO microrods

Figure 6.4 (a) shows the CL spectra collected from the tip of the undoped ZnO and heavily Ga-doped ZnO microrods at 80 K. The undoped ZnO microrod consists of a near-band-edge emission at 3.35 eV and a defect-related green emission band at 2.43 eV, which is characteristic of O-rich grown ZnO microrod with a high concentration of V_{Zn} defects [44]. This defect band is quenched in the Ga-doped nanorods since V_{Zn} defects are passivated by Ga dopants [125]. The slight redshift in the near-band-edge emission is due to the fact that the peak is now dominated by the Ga-bound exciton emission, rather than the band tail state. Figure 6.4 (b) shows the CL spectra collected along the length of an individual Ga-doped ZnO microrod whose diameter varies from 1 to 6 μm from tip to base at 80 K. With increasing Ga doping concentration from tip to base, the microrod reveals that; (i) the UV emission peak shifts to lower energy and becomes stronger, and (ii) the full width at half maximum (FWHM) of the emission peak is also monotonically increased. As described in the previous section, the lightly Ga-doped ZnO microrod tips show a dominated emission line at 3.358 eV, which is well known as the exciton bound to Ga donors, the I_8 line. The I_8 line has not been shown in the heavily Ga-doped ZnO microrod due to the broadening of the emission peak at degenerate doping level [97].

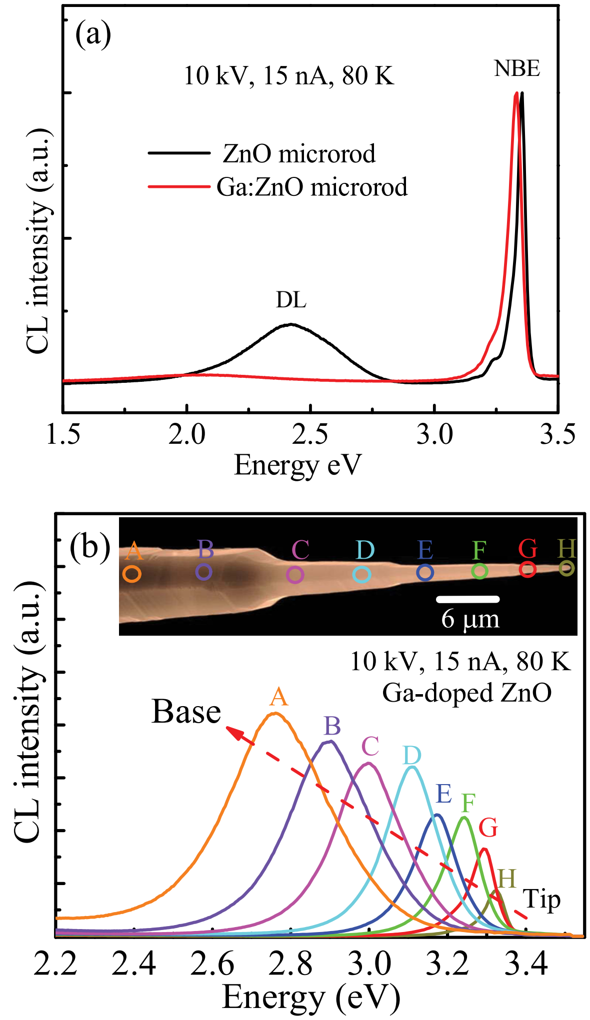

Figure 6.4. (a) CL spectra of undoped and heavily Ga-doped ZnO microrods at 80 K. The deep level emission is completely quenched in the Ga-doped ZnO microrod. (b) The NBE of individual Ga-doped ZnO microrod, displaying in the inset, showing a redshift ~ 0.6 eV as the Ga incorporation is increased from 1.5 at% at the tip to 6 at% at the base of the microrod.

As mentioned, the broadening of NBE emission can be caused by either the Burstein-Moss effect or the potential fluctuation of an impurity band. The redshift of UV emission in Figure 6.4 (b) strongly suggests that the broadening of the emission band in heavily Ga-doped ZnO microrod is due to the potential fluctuation of an impurity band rather than the Burstein-Moss effect [97]. Figure 6.5 shows the variation of the band potential fluctuation (σ) as a function of Ga concentrations.

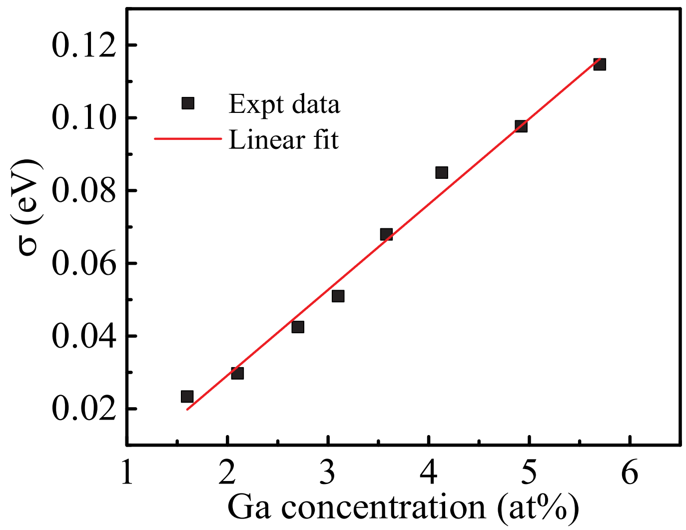

Figure 6.5. The band potential fluctuation, σ, as a function of Ga doping concentration showing the linear behaviour of potential fluctuation with Ga doping concentration.

The value of σ calculated from the experimental FWHM (ΔE) using the following expression [215]:

$$\Delta E^2 = (2\sigma\sqrt{ln4})^2 + (1.8kT)^2 \tag{6.1}$$

By neglecting the thermal broadening term,($(1.8kT)^2 = 5 \times 10^{-5}\ eV$), at 80 K, the ΔE is a linear function of σ. The thermal broadening is only effective at lower carrier concentrations less than 10^{17} cm^{-3} [217]. In heavily Ga-doped ZnO microrods grown at O-rich conditions, the $Ga_{Zn} - O_i$ and $Ga_{Zn} - V_{Zn}$ acceptor complexes are formed on the top of the valence band maximum. These localised states are developed by local strain resulted from the inhomogeneous distribution of charged impurity. At lower Ga doping level, the acceptor density of states is a discrete acceptor level. With increasing Ga doping concentration, the wave functions of the acceptors will overlap and results in a formation of an impurity band above the valence band maximum. This impurity band broadens with a further increase of Ga doping concentration and eventually merges with the valence band maximum, forming a band tail state [216]. The direct transition between the valence band tail state to conduction band leads to the redshift of CL emission peak. The near-band-edge emission increases in intensity from top to bottom of the microrod is due to the increase in the Ga doping concentration [214, 218].

6.5. Recombination kinetics of Ga-related emissions

To study the kinetics of observed emissions in Ga-doped ZnO microrods, the microrods are examined by the excitation power density-dependent CL analysis. In this analysis the electron beam current was varied from 0.1 to 7.8 nA, while the acceleration voltage was kept constant at 10 kV, corresponding to a CL generation depth of 800 nm.

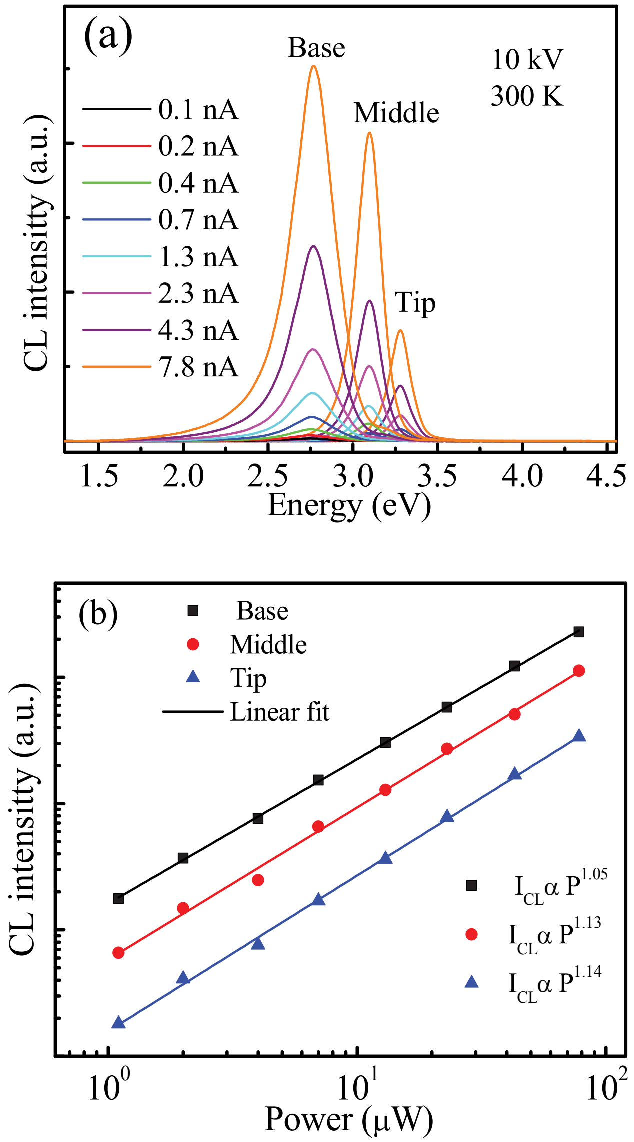

Figure 6.6. (a) Room temperature CL spectra collected from the tip, middle and base of a single Ga-doped ZnO microrod at different beam currents. (b) Log-log plots of the integrated intensities from the tip, middle and base of the Ga-doped ZnO microrod as a function of excitation power. The solid lines are the power law ($I_{CL}\ \alpha\ P_b^n$) fit to the experimental data.

Figure 6.6 (a) shows the CL spectra at different beam currents. The CL intensities from the tip, middle and base of a single Ga-doped ZnO microrod increase with increasing beam current. As shown in Figure 6.6 (b), the integrated CL intensities from different parts of the microrod as a function of excitation power. The CL intensities follow the power law $(I_{CL}\ \alpha\ P_b^n)$, where I_{CL} and P_b are the CL integrated intensity and the excitation power, respectively [173]. The exponent n of the Ga-doped ZnO microrod are found to be 1.05 ± 0.01, 1.13 ± 0.01 and 1.14 ± 0.01 for the emissions from tip, middle and base of the graded bandgap microrod, respectively. As shown in Figure 6.6 (b), the emission intensities do not become saturated with increasing CL excitation density, indicating fast recombination kinetics with a typical lifetime in the range of nanoseconds. The value of n lies between 1 and 2 for excitonic emission [44]. Thus, the optical emissions from the Ga-doped ZnO microrods are the NBE luminescence [44].

6.6. Defect-mediated bandgap engineering

To explain further the origin of the red-shift of NBE emission in Ga-doped ZnO microrods, the Density Function Theory (DFT) calculations were performed to estimate the variation of bandgap with Ga concentration. All the calculations were undertaken using the Siesta [219] implementation of spin-unrestricted DFT with the Perdew Burke Ernzerhof approximation [220] to the exchange-correlation functional. The nucleus-electron interaction is represented by norm-conserving pseudopotentials calculated according to the method described by Troullier and Martins [221]. The electronic charge is represented by numerical pseudo-atomic orbitals equivalent to a double-zeta plus polarisation basis set. In Siesta, these orbitals are strictly confined to a cut-off radius determined by a single energy value representing the shift in orbital energy due to confinement. Here, a confinement energy value of 5mRy is used, which ensures sufficient convergence without excessive computational time. Pristine ZnO is first geometrically optimised using a 21 × 21 × 21 Monkhurst-Pack reciprocal space grids to a tolerance of 0.01 eVÅ^{-1}. A large 3 × 3 × 2 supercell containing 36 ZnO units with a varying Ga concentration is used to realize defect structures $Ga_xZn_{1-x}V_{Zn}$ (Zinc vacancy and 'Ga' substituting for Zn) and $Ga_xZn_{1-x}O_i$ (Oxygen interstitial in octahedra site and Ga substituting for Zn). Figure 6.7 shows the defect structure at $x = 0 - 0.9$. For a supercell of this size, a reciprocal space grid of 7 × 7 × 10 is sufficient to ensure convergence of the total energy. The atoms in the defects structures are allowed to fully relax below a force tolerance of 0.03 eVÅ^{-1}. These optimised structures are used to calculate the optical properties in random phase approximation using an optical mesh of 14 × 14 × 14 and an optical broadening of 0.02 eV.

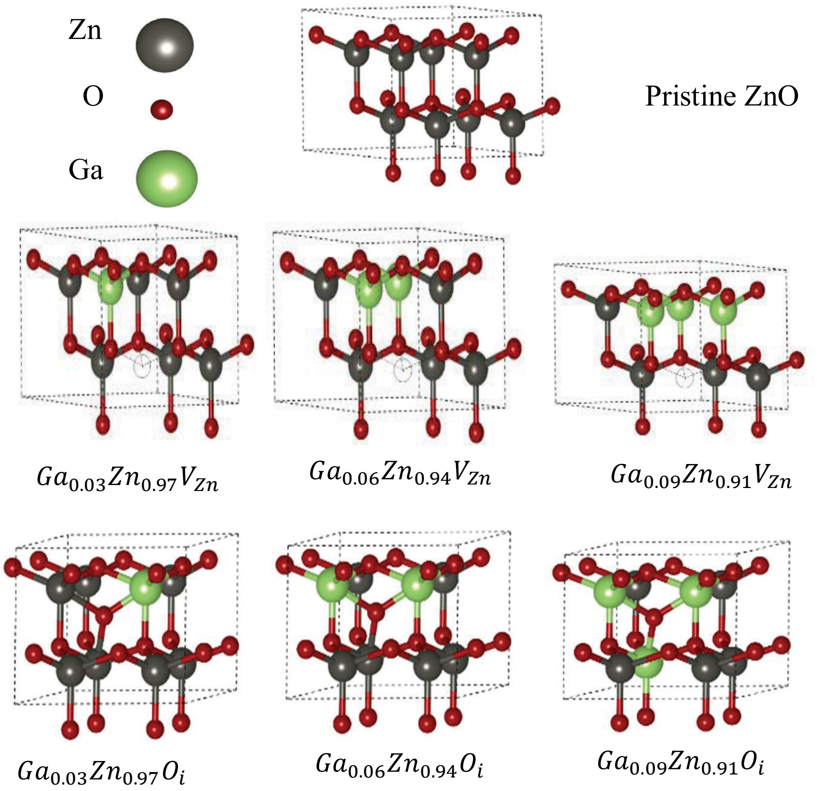

$Ga_{0.03}Zn_{0.97}V_{Zn}$ $Ga_{0.06}Zn_{0.94}V_{Zn}$ $Ga_{0.09}Zn_{0.91}V_{Zn}$

$Ga_{0.03}Zn_{0.97}O_i$ $Ga_{0.06}Zn_{0.94}O_i$ $Ga_{0.09}Zn_{0.91}O_i$

Figure 6.7. A representative $2 \times 2 \times 1$ supercell of pristine ZnO (1st row), supercells depicting $Ga_xZn_{1-x}V_{Zn}$ ($Ga_xZn_{1-x}O_i$) defect structure with varying concentration of Ga, 2nd row (3rd row). For clarity these structures are cut from bigger $3 \times 3 \times 2$ supercells used in the calculations.

The absorption edge affected by the formation of $Ga_{Zn} - O_i$ and $Ga_{Zn} - V_{Zn}$ complexes with increasing Ga concentration has been estimated using DFT (Figure 6.8 (a-b)). The absorption edge of pure ZnO is underestimated due to customary underestimation of fundamental bandgap by PBE [222]. However, the motivation of present work is to show the trend of optical absorption with increasing Ga concentration rather than producing the absolute values, therefore, we limit ourselves to PBE functional and avoid using computational expensive HSE06.

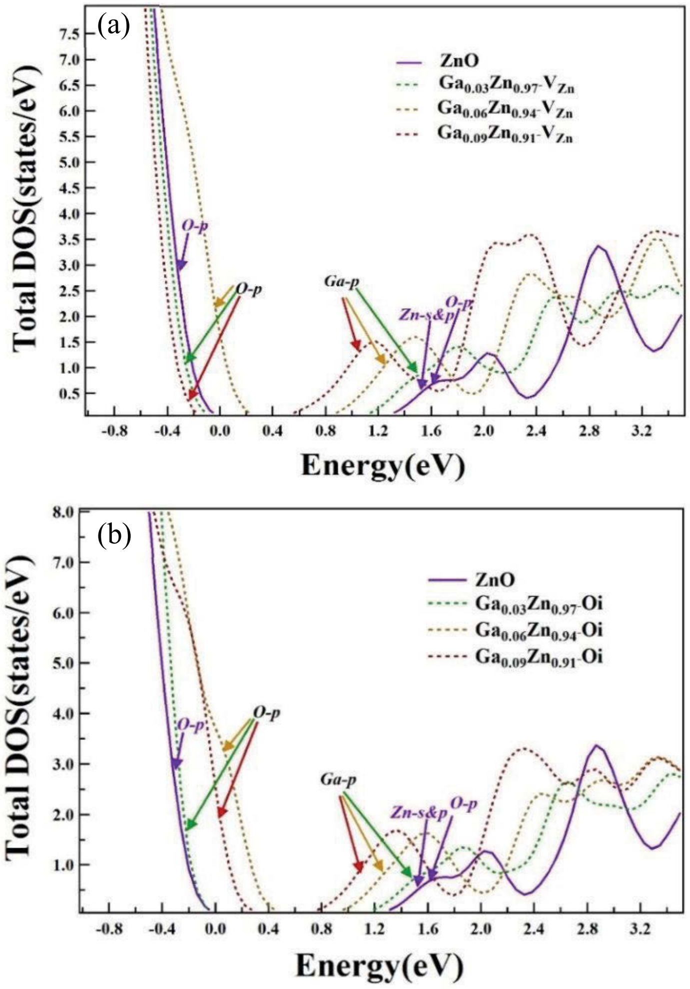

Figure 6.8. Total density of states of ZnO with varying concentration of Ga in (a) $Ga_xZn_{1-x}V_{Zn}$ and (b) $Ga_xZn_{1-x}O_i$ defect structures.

Figure 6.9 shows the comparison of the experimental and theoretical band gap shift as a function of Ga-doping concentration in ZnO. The increase of bandgap is observed with Ga in the Zn site in agreement with previous studies [223, 224]. This increase in the bandgap is due to the shift of Fermi level above the conduction band. The upward shift of Fermi level is caused by the increase of carrier concentration with high Ga doping level, which is due to the well-known Burstein–Moss (BM) [225, 226].

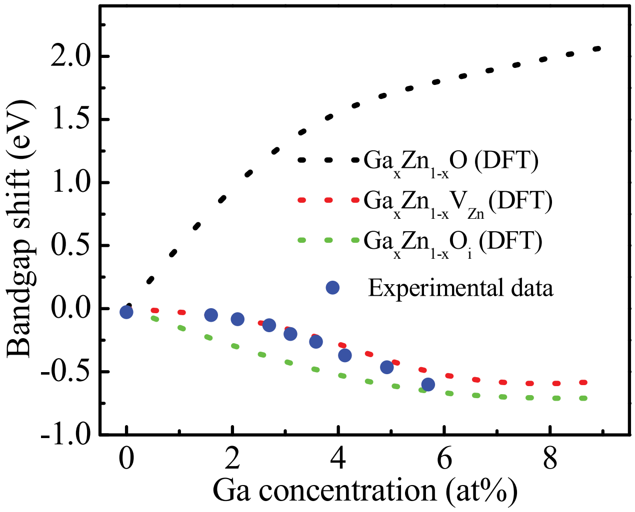

Figure 6.9. The optical bandgap shift with increasing Ga concentration. The black dotted line showing the increase of bandgap by the increase of Ga donor concentration. The red and green dotted line showing the decrease of bandgap with the formation $Ga_{Zn} - V_{Zn}$ and $Ga_{Zn} - O_i$complexes. The blue solid circles showing the experimental NBE shift with increasing Ga doping concentration from top to bottom of the microrod.

The decrease of bandgap is observed with the formation of $Ga_{Zn} - V_{Zn}$ and $Ga_{Zn} - O_i$ complexes in Ga-doped ZnO. Ga occupies substitutionally the Zn site (Ga_{Zn}), which acts as a shallow donor leading to the formation of $Ga_{Zn} - V_{Zn}$ and $Ga_{Zn} - O_i$ complexes in Ga-doped ZnO [24]. As mentioned earlier, Ga-doped ZnO microrods were grown at the oxygen-rich condition. In the oxygen-rich environment, the $Ga_{Zn} - V_{Zn}$ and $Ga_{Zn} - O_i$ complexes have lower formation energy than the Ga donors at higher Ga doing level. The valence band maximum and conduction band minimum of pure ZnO is contributed mostly by ‘O-p’ states and hybridisation of Zn-s&p and O-p states, respectively. For these $Ga_{Zn} - V_{Zn}$ and $Ga_{Zn} - O_i$ complexes, the charge compensating Ga donor and acceptor states (V_{Zn}, O_i) coexist in energy resulting in the decrease of bandgap as the conduction band minimum formed by hybridisation of Ga-p and O-p states is pulled down in energy [88, 222]. The upward shift of valence band occurs for $Ga_xZn_{1-x}O_i$ complexes for all Ga concentration while the downward shift is observed for $Ga_xZn_{1-x}V_{Zn}$ until $x = 0.09$. Thus a complete compensation of Ga donors by V_{Zn} acceptors results in an upward shift of the valence band maximum. The formation of $Ga_xZn_{1-x}V_{Zn}$ and $Ga_xZn_{1-x}O_i$ defects do not change the basic electronics of the ZnO lattice, but only generate an additional fully occupied impurity band above the valence band maximum. With increasing Ga doping, the wave functions of the impurity band overlap and ultimately merge with the valence band maximum, results in a band tail state. The absorption will occur between the occupied impurity band rather than the original valence band and the Ga_{Zn} donor states in the conduction band, leading to the narrowing of the bandgap of ZnO. The spectral broadening is attributed from the random distribution of the density of charged impurities and also from the Coulombic interaction between individual donors and acceptor complexes involved in the recombination mechanism [227].

6.7. Conclusions

Bandgap engineering of ZnO was studied in a single tapered microrod whose diameter varies from 1 to 6 μm from tip to base. ZnO microrods with a graded distribution of Ga were fabricated by a self-catalyst vapour phase transport method. The emission peak was found to be red shifted by 0.6 eV and broadened with increasing local Ga concentration from 1.5 to 6 at%. These emissions from the tapered Ga-doped ZnO microrod have characteristics of a near-band-edge emission. From the Density Functional Theory, it is argued that the bandgap narrowing arises from the merging of Ga defect complexes with ZnO energy bands. The broadening of the NBE emission monotonically increases with Ga concentration, which can be explained in terms of alloy potential fluctuations. These results demonstrate self-regulation of the charged defect compensation and the possibility of multi-wavelength light sources within a microrod.

Chapter 7

Optimisation of ZnO nanorods for LED devices

ZnO semiconductor is recognised as an alternative of GaN for solid state lighting due to its high crystal quality, superior optical properties and low production cost. Moreover, the growth of vertically aligned ZnO nanorods is easier than GaN nanorods. In addition, vertically aligned nanowires/nanorods can provide waveguided optical emission, which enables the fabrication of LEDs with improved light extraction efficiency. ZnO is an attractive material for tunable visible LEDs, since its various point defects act as a source of different visible emissions. However, due to the lack of stable p-type doping in ZnO, most LED devices are developed based on p-n heterojunctions. In general, ZnO heterojunction diodes exhibit inefficient electrical injection and have weaker light emission than homojunction devices because band offsets at the interface can reduce carrier injection. This chapter focuses on the fabrication of chromaticity stable and colour tunable heterojunction light emitting diodes using vertically aligned Ga-doped ZnO nanorods grown on p-type silicon. The effect of Ga doping concentration on the light extraction efficiency and junction current of ZnO nanorod-based heterojunction LEDs are investigated.

7.1. Uses of ZnO nanowires in optoelectronic applications

Although significant accomplishments have been attained in nitride-based light emitting devices, the pursuit of higher emission intensity and long-life photonic devices never ceases. Compared with thin films, nanowires offer immense potential in photonics as they can support lasing and enhance light extraction efficiency by virtue of nanowire waveguide properties [228-230]. Although Gallium Nitride (GaN) has become a key material for the light emitting diode (LED) technology operating in the green to UV range, GaN nanowires are technically difficult to grow, requiring advanced semiconductor growth reactors. Conversely, ZnO nanowires can be fabricated using the simple vapour transport method. Accordingly, ZnO nanowires have emerged as one of the most important building block in photonics and have been exploited in LEDs [231, 232], laser diodes [233, 234], and multi-coloured displays [235].

Nanowires offer immense prospects in photonics as they can support lasing and act as direct waveguides in LED devices to increase light extraction efficiency without the need of reflectors and lenses [228-230]. However, photonic and optoelectronic devices based on ZnO nanowires generally exhibit inefficient electrical injection into the semiconductor and weak light output because of poor carrier transport in nanowires and at the junction interface [231, 236, 237]. These issues arise largely from inherent limitations associated with the low conductivity of ZnO nanowires and high energy barrier heights of ZnO heterostructures [238, 239]. To overcome this issue, considerable efforts have been dedicated to controlled incorporation of n-type and p-type dopants. Among various n-type dopants, Ga has been recognized as one of the most efficient dopants for enhancing the electrical conductivity of ZnO nanorods [28, 157]. The bond length Ga–O (0.192 nm) is almost identical to that of Zn–O (0.197 nm), resulting minimal distortion in the lattice. Taking advantage of the Ga donor's excellent lattice match, bandgap engineering has been successfully demonstrated for Ga-doped ZnO nanowires with a maximum redshift of ~ 0.3 eV in the UV range [29]. Recently, experimental observation of electroluminescence (EL) was reported in micrometre-sized Ga-doped ZnO rods under Joule heating at high temperatures [80, 156]. The luminescence performance of p-n heterojunction diodes employing Ga-doped ZnO nanorods has not been investigated thus far. For practical applications, it is important to develop an efficient method to widely tune the emission of ZnO nanowire heterojunctions in the visible range.

The work in this chapter is aimed to grow vertically aligned ZnO nanorods fabricated by a direct route vapour transport method and to use these nanorods as an active nanostructured layer as well as nanoscale optical waveguides for LEDs. Ga dopants produce very high-quality n-type ZnO nanorods. The enhancement of the nanorod quality and the higher carrier transport at the nanorod heterojunction were found to significantly increase the EL emission performance of ZnO nanorods/p-Si heterojunction LED devices. LED devices fabricated with Ga-doped nanorods produce chromaticity-stable emission in the visible range without damaging heating effects. Furthermore, these electrically driven Ga-doped nanorod LED devices exhibit a significantly lower turn-on voltage and higher electrical injection, and colour-tunable EL that is an order of magnitude brighter than equivalent devices made with pristine nanorods.

7.2. Fabrication of ZnO nanorod-based LEDs

Highly oriented Ga-doped ZnO nanorods were grown on heavily B-doped p-type Si substrates (resistivity 8.7 Ω.cm and hole concentration 1.44×10^{17} cm^{-3}) using the vapour phase transport methods as described in the chapter 3. In this high temperature (950 °C) growth technique, the p-Si substrate is more suitable than p-GaN due to its high thermal stability. Different Ga concentrations in nanorods were achieved by adding different amounts of Ga_2O_3 powder to the source material with concentrations up to 1.4 at%. The source material was heated at 950ºC under a constant flow of Ar/O_2 (20:6 sccm) gas during growth to promote the growth of nanorods.

A series of undoped and Ga-doped ZnO nanorods/p-Si heterojunction LED devices were fabricated. Figure 7.1 (a) shows vertically aligned ZnO nanorods grown on p-Si substrate. The polymethyl methacrylate (PMMA) was deposited by spin coating on the nanorods with a rotation speed of 2000 rpm for 2 minutes to fill up the gaps between the nanorods (Figure 7.1 (b)). Then, oxygen plasma etching (at 20 sccm oxygen flow for 20 mins) was subsequently applied to expose the tips of ZnO nanorods (Figure 7.1 (c)). The Ohmic contact of indium tin oxide (ITO) electrode (200 nm thick) was deposited onto the exposed nanorod tips through a shadow mask using an Edwards EO6 deposition system.

Figure 7.1 (d) shows a typical small area (~1 × 1 mm^2) and large size (~5 × 2 mm^2) devices and their corresponding photographs of EL emission in the inset. In this VPT method, a large area sample up to 20 × 20 mm^2 with a uniform distribution of nanorod arrays can be grown. So, the size of the LED device can be easily adjusted in the range of up to 15 × 15 mm^2 by changing the area of the shadow mask used during the growth of ITO electrode.

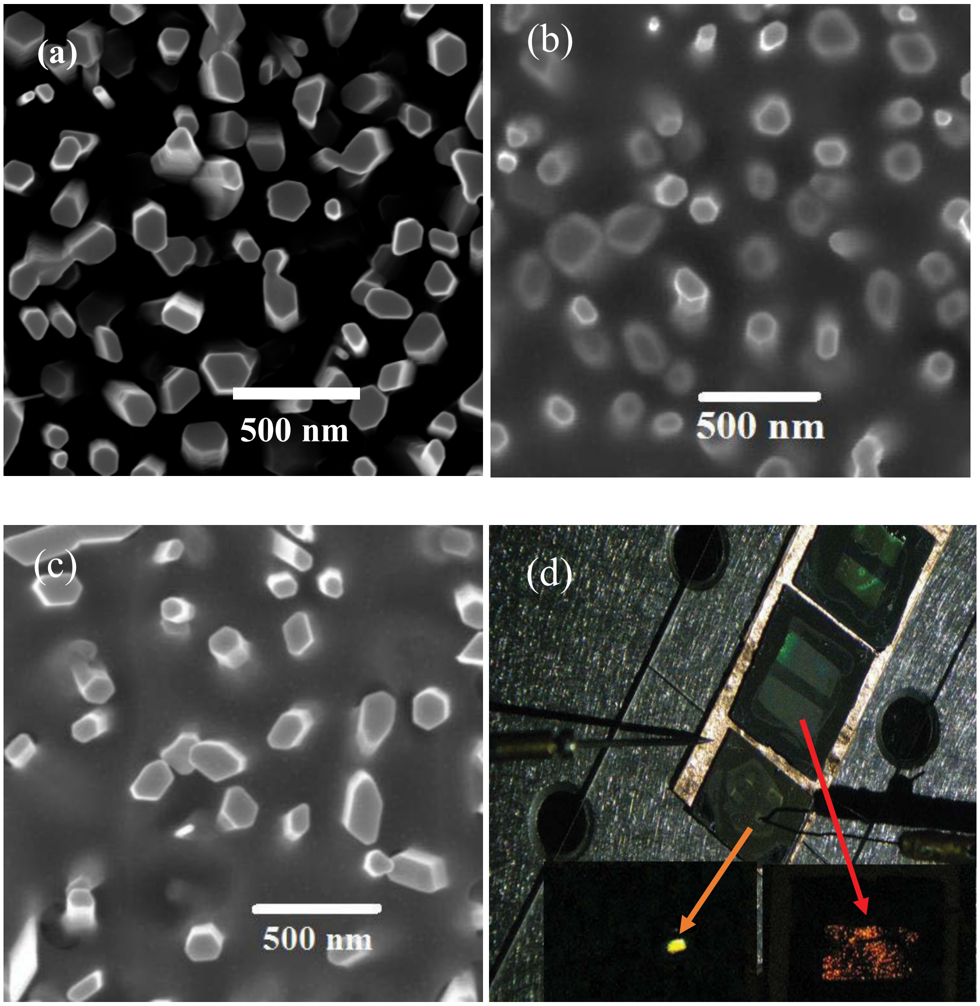

Figure 7.1. Optimisation of ZnO nanorods and LED device structure. (a) As grown Ga-doped ZnO nanorods, (b) PMMA coated nanorods and (c) the exposed nanorods tips produced by oxygen plasma etching. (d) Typical small area (~1 x 1 mm^2) and large size (~5 x 2 mm^2) devices and their corresponding photographs of EL emission in the inset.

7.3. Current-voltage characteristics of ZnO nanorod-based LEDs

The tips of the Ga-doped ZnO nanorods were directly contacted with an ITO layer; the p-Si substrate was spaced by a thin PMMA layer (deposited by spin coating) in order to prevent direct contact between the ITO electrode and p-Si substrate. Figure 7.2 (a) presents the *I–V* characteristics of nanorods/p-Si heterojunctions measured under direct current biased conditions at room temperature, displaying a characteristic diode behaviour for both undoped and Ga-doped ZnO nanorods. Under the same bias, the LED devices of the same area fabricated from Ga-doped nanorods exhibit a much higher current density. This suggests that the incorporated Ga atoms form additional midgap states especially Ga_{Zn}-V_{Zn} pairs, which lower carrier injection barriers for the heterojunction.

The *I–V* characteristics of the heterojunction diode were further analysed by plotting the data on a log-log scale (Figure 7.2 (b)). In region I, $V < 3.8$ V, the junction current increases almost linearly with applied voltage, $I \propto V^{1.1}$, which demonstrates the transport mechanism followed Ohm's law due to the inter-band electron tunnelling at the Si-ZnO interface [240]. In the region II, $V > 3.8$ V, the current increases exponentially, $I \propto V^{11.7}$, which is attributed to a recombination-tunnelling mechanism commonly observed in wide band gap semiconductor p-n junctions [241].

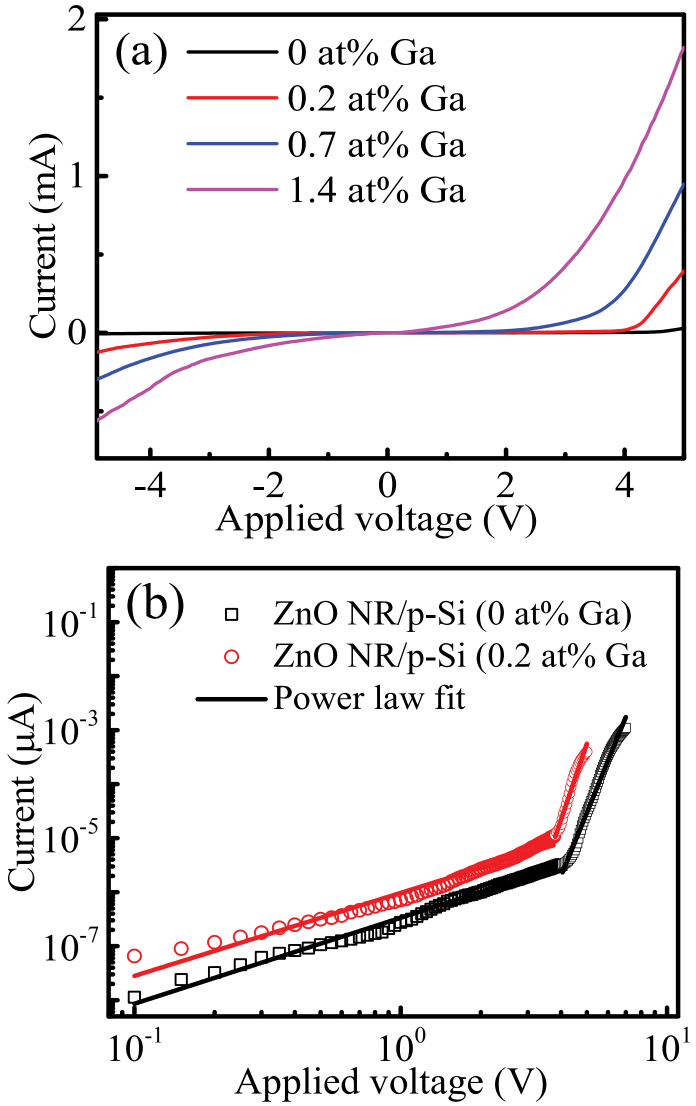

Figure 7.2. (a) *I*-*V* characteristic of the ITO/nanorods/p-Si heterojunction LED, showing substantial enhancement of the electrical conduction of the heterojunction with increasing Ga doping concentration. (b) *I*-*V* characteristics in the log-log plot curve displaying two regions with different characteristics: $I \propto V^{1.1}$ at $V < 3.5$ V and $I \propto V^{11.7}$ at $V > 3.5$ V.

The total series resistance, R_s, accounts for Ohmic losses due to the resistance of Si substrate and ZnO nanorods, the shunt resistance, R_{sh}, represents the current leakage across the heterojunction. The *I–V* characteristics were analysed by using a one-diode equivalent circuit model [242], as described in chapter 3. R_{sh} and R_s can be determined from the slope of the dark *I–V* curve at near-zero voltage (-0.3 V < V < 0.3 V) and the linear, high current region, respectively (Figure 7.3 (a) [242].

The R_s and R_{sh} values of the ZnO nanorod/Si LED are shown in Figure 7.3 (b). For the LED fabricated with undoped ZnO nanorods, $R_s = 34 \pm 2$ kΩ, which is large due to the high resistance of the nanorods. The R_s value decreases dramatically by two orders of magnitude upon the use of Ga-doped ZnO nanorods in identical LED devices; this can be attributed to the improved nanorod crystal quality and the activation of Ga_{Zn} shallow donors, which in turn lead to higher conductivity of the nanorods. The reason for the decrease in R_{sh} in the LEDs fabricated with Ga-doped ZnO nanorods is unclear but likely due to increasing current passing along the Ga-doped ZnO nanorod sidewalls and bypassing the heterojunction.

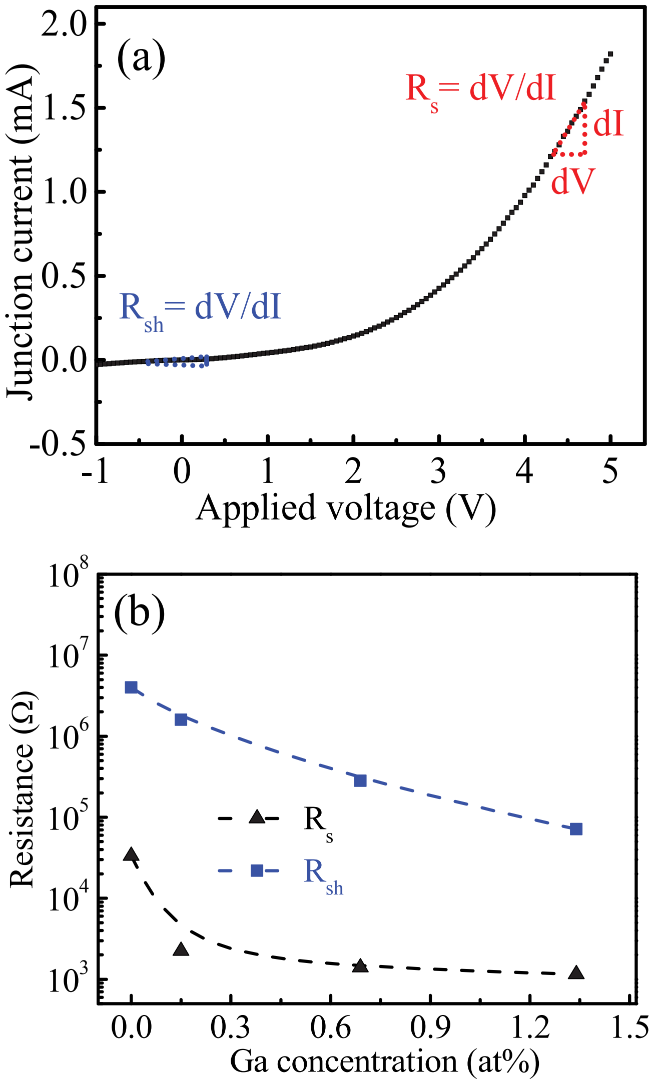

Figure 7.3. (a) A typical *I*-*V* curve showing the determination of shunt resistance (R_{sh}) and series resistance (R_s) from the slope of the curve at near-zero voltage (-0.3 V < V < 0.3 V) and the linear, high current region, respectively. (b) Variations of R_{sh} and R_s and turn-on voltage of the heterojunction as a function of Ga doping concentration.

Figures 7.4 (a)-(c) show the determination of turn-on voltages of Ga-doped ZnO nanorods at different Ga doping concentrations. The measured turn-on voltages are plotted in Figure 7.4 (d). The turn-on voltage is found to decrease from 4.5 to 2.8 V, when Ga doping concentration increases from 0 to 1.4 at%. The decrease in the turn-on voltage with increasing Ga doping concentration can be directly attributed to lower total series resistance across the LED device.

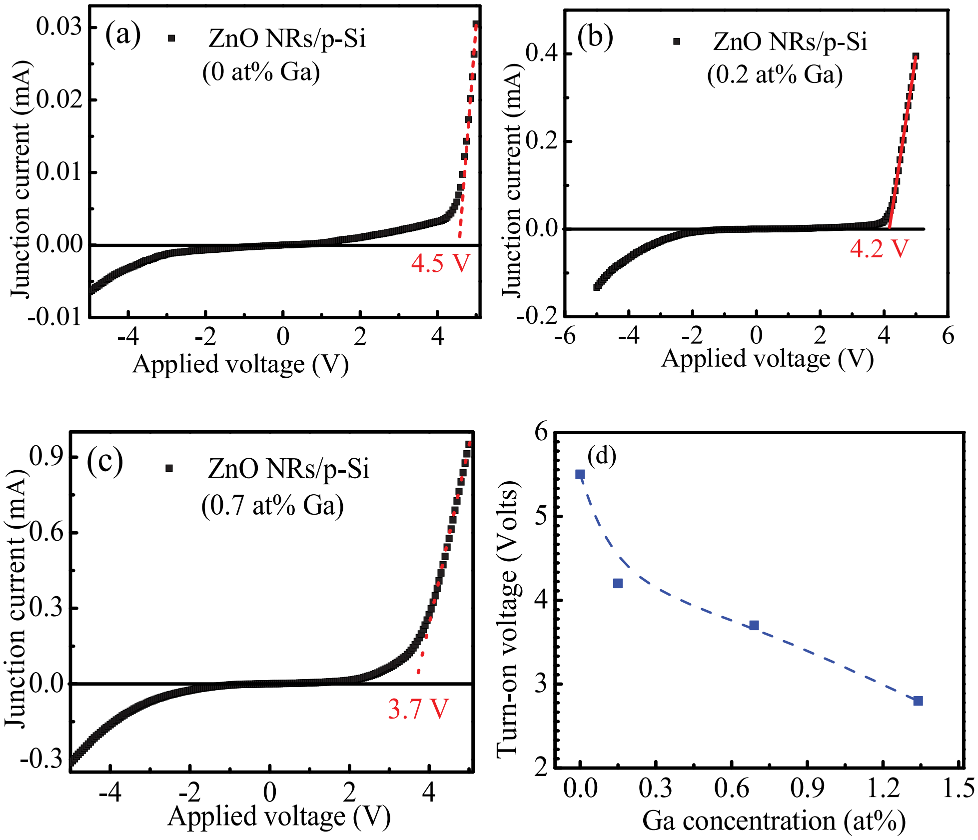

Figure 7.4. (a) – (c) *I-V* plots for the determination of turn-on voltages of p-Si/Ga-doped ZnO nanorods LEDs. (d) Turn-on voltage as a function of Ga doping. The turn-on voltage is gradually decreased with increasing Ga doping concentration in the nanorods.

7.4 Optical properties of Ga-doped nanorod-based LEDs

7.4.1. Temperature-dependent excitonic emissions

The near-band-edge CL spectra of undoped ZnO nanorods show bound exciton (D^oX) and free exciton (FX) emissions at 3.362 and 3.376 eV, respectively, together with several phonon replicas (Figure 7.5 (a)). The bound exciton at 3.362 eV in undoed ZnO is due to H impurities [23]. The shoulder at 3.331 eV is assigned as Y-line attributed to the localisation of excitons at the structural defects, usually referring to the exciton bound to surface defects [243].

In Ga-doped ZnO nanorods, the Y-line is largely suppressed, indicating the dissociation of excitons from the surface structural defects and improvement of crystal quality (Figure 7.5 (b)). The NBE emission is dominated by the I_8 line at 3.359 eV attributed to excitons bound to neutral Ga_{Zn} donors [94]. The emission line at 3.32 eV in Ga-doped ZnO has previously been assigned as donor-acceptor pair due to the electronic transition between neutral Ga_{Zn} donors to neutral V_{Zn} acceptor or acceptor complexes [94].

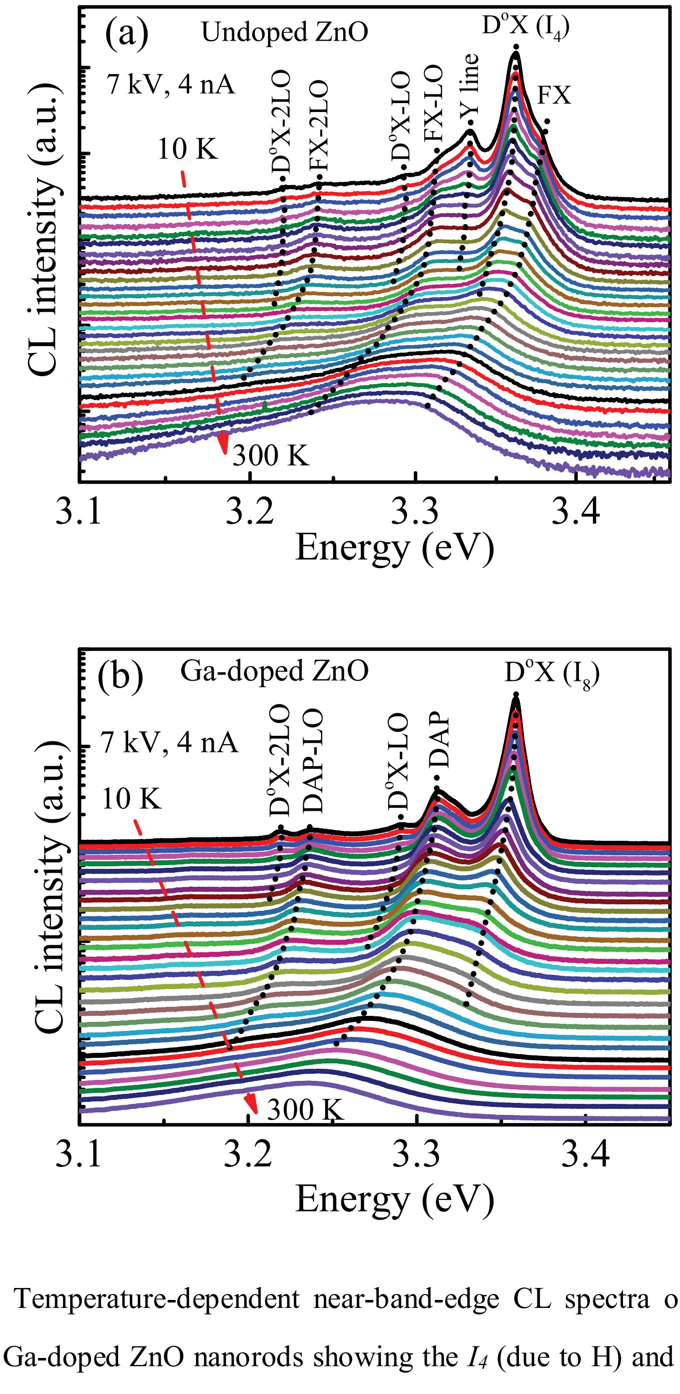

Figure 7.5. Temperature-dependent near-band-edge CL spectra of (a) undoped (b) 1.4 at% Ga-doped ZnO nanorods showing the *I₄* (due to H) and *I₈* (due to Ga) lines.

In order to determine the thermal activation energies of bound excitons, the temperature-dependent NBE CL intensities of undoped and Ga-doped ZnO nanorods were studied (Figure 7.6 (a)). The temperature-dependent CL intensity can be expressed by the following expression [244];

$$I(T) = \frac{I_o}{1 + C\exp\left(-\frac{E_A}{k_B T}\right)} \tag{7.1}$$

where C is constant and other symbols have their usual meaning. The activation energies for undoped and Ga-doped ZnO nanorods are almost similar of about 6 meV below 60 K. In the 60-160 K temperature range, the values of activation energies are found to be 32 meV and 52 meV for undoped and Ga-doped ZnO, respectively. Above 160 K, the bound excitons emissions were quenched. The 52 meV energy is consistent with the ionisation energy of Ga_{Zn} donors. The strong I_8 line indicates that Ga dopants are incorporated in the nanorods by substituting Zn in the ZnO lattice.

The temperature dependence of bandgap, $E_g(T)$, for ZnO nanorods can be evaluated by Varshni's empirical formula [245];

$$E_g(T) = E_g(0) - \frac{\alpha T^2}{T + \beta} \tag{7.2}$$

where $E_g(0)$ is the bandgap energy at 0 K, α and β are constants and β is proportional to the Debye temperature (θ_D). For $T > \theta_D$, β is approximately $3/8\theta_D$ while β is equal to θ_D at low temperature [246]. The equation (7.2) was used to calculate the peak energies of bound excitons, where the E_g is replaced by $D^{\circ}X$. The experimental data were best fitted with the following parameters; $\alpha = 7.5 \times 10^{-4}\ eV/K$, $E_g(0) = 3.363\ eV$ and $\beta = 800 \pm 20$ for undoped ZnO and $\alpha = 7.5 \times 10^{-4}\ eV/K$, $E_g(0) = 3.359\ eV$ and $\beta = 500 \pm 20$ for Ga-doped ZnO nanorods.

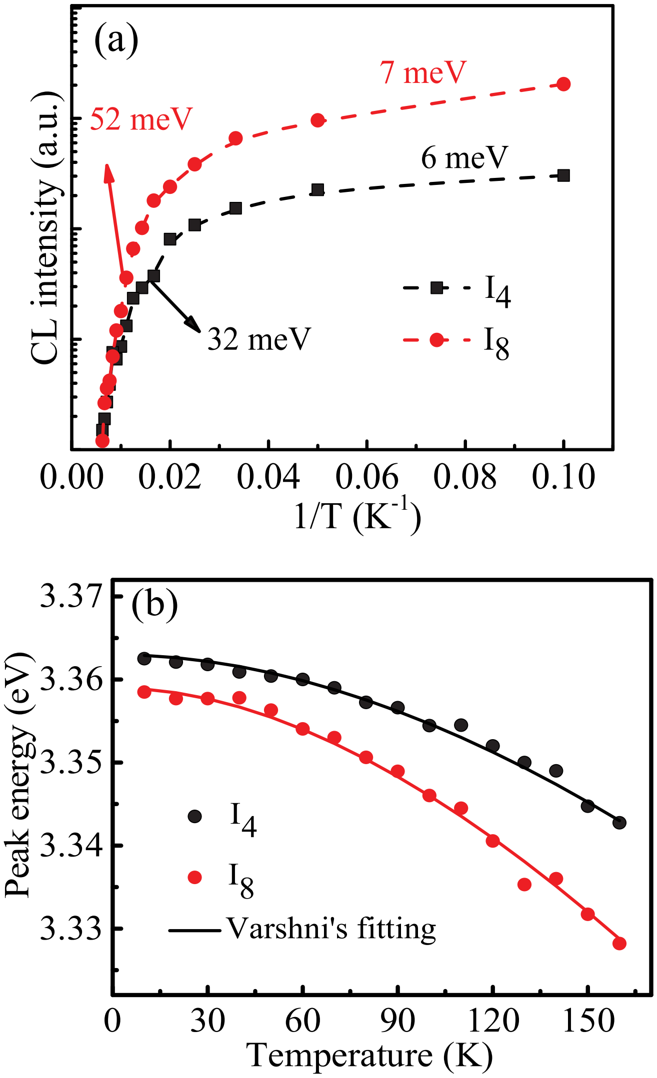

Figure 7.6. (a) Arrhenius plots of CL integrated intensities of bound excitons showing activation energies of 32 and 52 meV for undoped and Ga-doped ZnO nanorods. (b) The variation of bandgap as a function of temperature for undoped and Ga-doped ZnO nanorods. The solid lines are the least square fit of Varshni's equation to the experimental data.

In the Figure 7.6 (b), the least square fit of equation (7.2) is shown as the solid lines with the experimental CL data (solid circles). The calculated peak energies are consistent with the experimental data. The results indicate that the Varshni's equation provides an adequate insight of the temperature dependence of bound excitons and the bandgap of ZnO. The redshift of bound excitons with increasing temperature in undoped and Ga-doped ZnO nanorods is attributed to bandgap shrinkage.

7.4.2. Colour-tunable emission in ZnO by Ga doping

Figure 7.7 (a) illustrates room temperature deep level CL spectra of Ga-doped ZnO nanorods at different Ga concentrations. The CL spectra of undoped ZnO show an NBE emission centred at 3.28 eV with a broad green luminescence band at 2.43 eV. Comparison with the CL spectra before and after Ga doping, the spectra reveal; (i) the enhancement of NBE emission with no significant peak shift, (ii) the deep level emission peak shifts to lower energy, results in a tunable emission from green to yellow at room temperature.

As mentioned, the 2.43 eV green emission in undoped ZnO has been attributed to V_{Zn} [35]. With increasing Ga doping concentration, the deep level emission peak shifts to the lower energy while the V_{Zn}-related green luminescence at 2.43 eV gradually quenched and become negligible at 1.4 at% Ga doping (Figure 7.7 (a)). This observation is consistent with Ga dopants occupying the Zn sites, leading to a decrease in the concentration of V_{Zn} defects. The Ga-mediated redshift of visible emission band has previously been reported in Ga-doped ZnO microrods [80]. The incorporation of 1.4 at% Ga leads to the quenching green luminescence in the Ga-doped ZnO nanorods, which exhibits strong Ga-mediated yellow emission band as the Ga luminescence centres become abundant and dominate the radiative recombination (Figure 7.7 (a)). At O-rich conditions, Ga donors interact with acceptor-like defects (V_{Zn}), producing the abundance of Ga_{Zn}-V_{Zn} acceptor complexes [24]. These defects provide a new recombination pathway for the yellow emission while the V_{Zn}-related GL emission is almost quenched as a result of the formation of Ga_{Zn}-V_{Zn} complexes.

The undoped ZnO shows a weak NBE emission, which gradually increases with increasing Ga doping concentration. It has been reported that the NBE emission depends on the crystalline quality of ZnO and the shallow donor concentration [161]. The integrated intensity ratio of near-band-edge to deep level (I_{NBE}/I_{DL}) as a function of Ga doping concentration under same excitation conditions is shown in Figure 7.7 (b). It can be seen that the I_{NBE}/I_{DL} increases with increasing Ga doping concentration. This result indicates that the Ga doping improves the nanorod crystal quality as well as the optical properties of ZnO nanorods. This result is also consistent with the Raman spectra, which shows the enhancement of E_2 (high) peak after Ga doping as presented in chapter 5. The near-band-edge emission peak shows no significant shift with Ga doping concentration. This is because the lightly Ga doping only shifts the Fermi level of several meV without changing the bandgap of ZnO at lower Ga-doping concentration. This result is also consistent with the upward shift of the Fermi level without changing the bandgap at lower Ga doping level as demonstrated in the chapter 5.

It is worth noting that Ga-doped ZnO microrods show strong near-band-edge emission with negligible deep level emission as presented in chapter 6, while Ga-doped ZnO nanorods show relatively stronger deep level emission. The defect emission is more dominant in a smaller size nanorod. This is because the reduction of nanorod size causes more atoms to be closer to the surface, results in the increase of surface recombination [247].

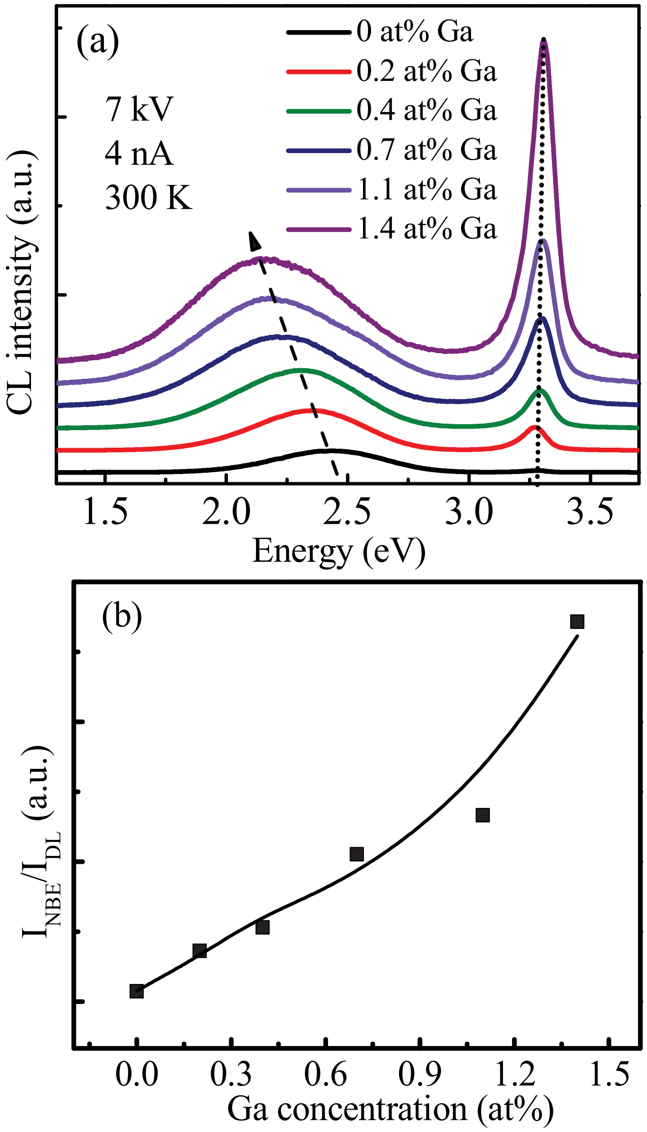

Figure 7.7. (a) Room temperature CL spectra at different Ga doping concentrations. The deep level emission showing a gradual redshift with increasing Ga doping concentration resulting a colour-tunable emission from green to yellow luminescence. (b) The integrated intensities of I_{NBE}/I_{DL} as a function of Ga doping concentration showing an increase of I_{NBE}/I_{DL} with increasing Ga doping.

7.4.3. Recombination kinetics of Ga-related defects in ZnO

To study the kinetics of observed emissions in Ga-doped ZnO nanorods, the nanorods were examined by the excitation power density-dependent CL analysis. In this analysis the electron beam current was varied from 0.04 to 35 nA, while the acceleration voltage was kept constant at 7 kV, corresponding to a CL generation depth of 380 nm.

Figures 7.8 (a)-(b) show the room temperature CL spectra of undoped and 0.7 at% Ga-doped ZnO nanorods at different beam currents. The excitation power dependent CL integrated intensities of YL and GL are determined from the Gaussian fitting of 0.7 at% Ga-doped ZnO nanorods (Figure 7.8 (c)). These peak parameters were obtained from the spectral profiles of the undoped ZnO (which exhibits only the GL emission with a peak of 2.43 ± 0.02 and FWHM = 0.50 ± 0.05 eV), whereas the 1.4 at% Ga-doped ZnO displays distinct YL (E_{YL} = 2.10 ± 0.02 and FWHM = 0.60 ± 0.05 eV).

Figure 7.8 (d) show the CL integrated intensity as a function of excitation power. The CL intensities follow the power law ($I_{CL}\ \alpha\ P_b^n$), where I_{CL} and P_b are the CL integrated intensity and excitation power, respectively [173]. The exponent n of the undoped and 0.7 at% Ga-doped ZnO nanorods are found to be 0.75 ± 0.01, 0.94 ± 0.01 for GL and YL, respectively. The YL emission possesses slower saturation rate (higher n value) than the GL band in Ga-doped ZnO nanorods. This result confirms the existence of Ga-related luminescence centres in Ga-doped ZnO nanorods and the success of producing abundant Ga-related radiative centres in the nanorods.

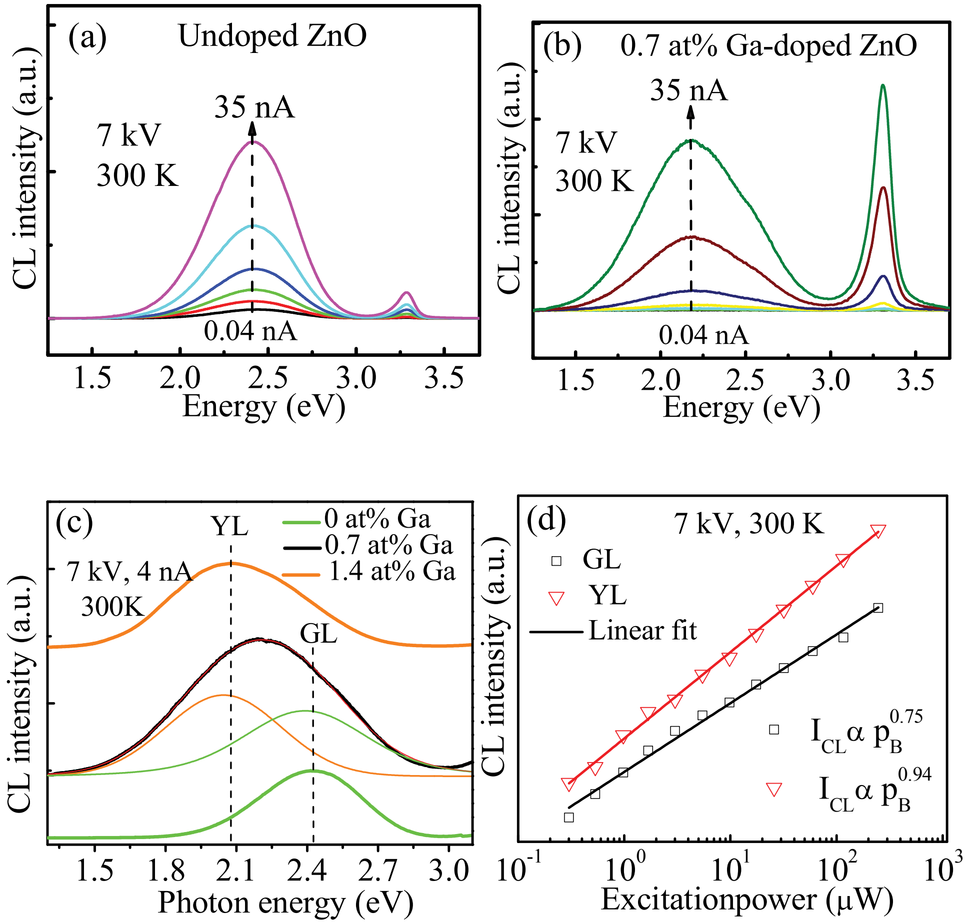

Figure 7.8. (a) - (b) Room temperature CL spectra of undoped and Ga-doped ZnO nanorods at different electron beam currents. (c) The Gaussian fitting of green and yellow emissions in 0.7 at% Ga-doped ZnO nanorods. (d) Log-log plots of the integrated intensities of the ZnO GL and Ga-mediated YL emissions as a function of excitation power. The solid lines are the power law $(I_{CL} \alpha P_b^n)$ fit to the experimental data.

7.4.4. Thermal behaviour of Ga-related defects in ZnO

In order to achieve further information about the Ga-related defect states in the ZnO nanorods, the temperature dependent deep level CL spectra of undoped and Ga doped ZnO nanorods were investigated.

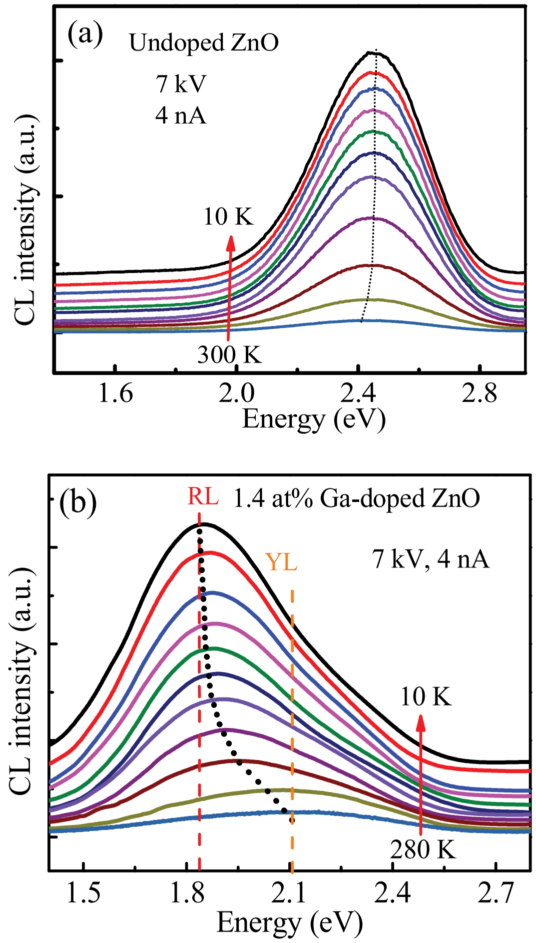

Figure 7.9. (a) Temperature-dependent CL spectra of (a) undoped and (b) 1.4 at% Ga-doped ZnO. With decreasing temperature from 10 to 300 K, the CL peak of undoped ZnO showing a 25 meV redshift, while the Ga-doped ZnO showing 250 meV blueshift.

Figures 7.9 (a)-(b) show the temperature-dependent CL spectra of undoped and 1.4 at% Ga-doped ZnO in the temperature range of 10-300K. With increasing temperature from 10 to 300 K, the CL peak position of undoped ZnO exhibits a 25 meV redshift, while 1.4 at% Ga-doped ZnO shows a 250 meV blueshift. At 10 K, the 1.4 at% Ga-doped ZnO shows red luminescence (RL) at 1.85 eV. With increasing temperature, this spectrum shows a gradual blueshift and appears as YL (2.10 eV) emission at 300 K. The variation of peak positions as a function of temperature of undoped and Ga-doped ZnO nanorods are shown in Figure 7.10. With increasing temperature, the 25 meV redshift of ZnO GL can be explained by the Varshni's equation (7.2). This redshift of the GL with the increasing temperature is attributed to bandgap shrinkage.

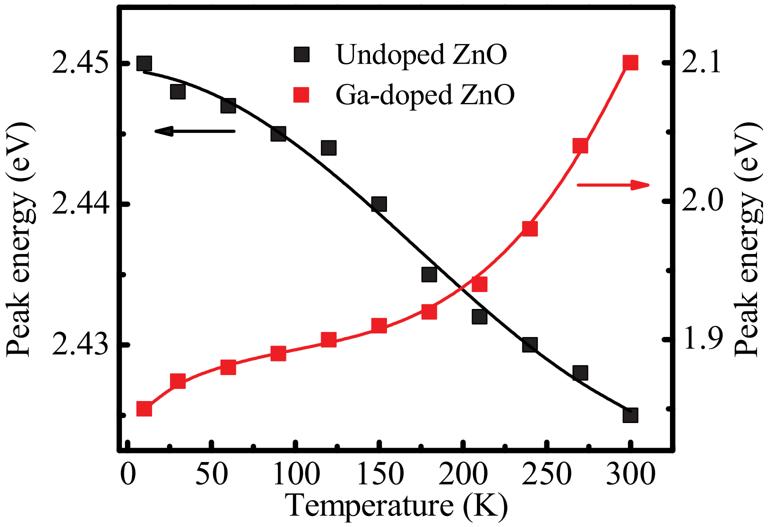

Figure 7.10. The peak position of deep level emissions showing 25 meV redshift and 250 meV blueshift for undoped and Ga-doped ZnO, respectively with increasing temperature from 10 to 300 K.

The Varshni's equation can not explain the 250 meV blueshift in Ga-doped ZnO. Several theoretical and experimental predictions have shown that the Ga_{Zn} donors are located at 55 meV below the conduction band and the Ga-related Ga_{Zn}-V_{Zn} acceptor complexes are located at 0.75 eV above the valence band maximum [23, 24, 78]. The variation of CL intensity as a function of temperature is shown in Figure 7.11. The measured activation energies from the Figure 7.11 are presented in Table 7.1. These activation energies are reasonably agreed with the previously reported energy activation energies of Ga-related defects as measured by Hall measurements [23, 24, 78].

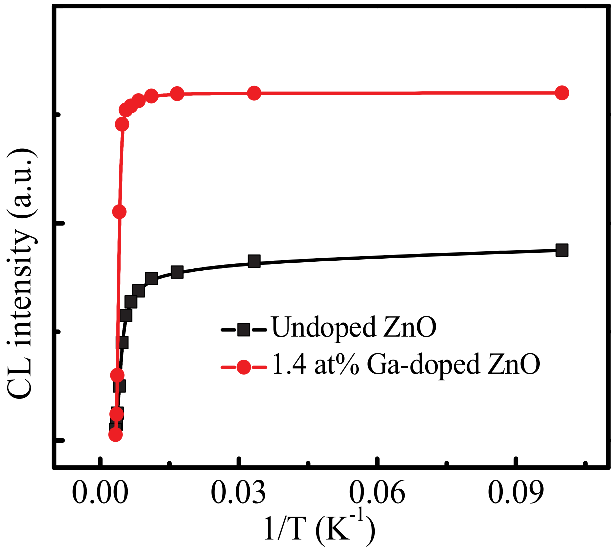

Figure 7.11. Arrhenius plots of CL integrated intensity for undoped and Ga-doped ZnO. The undoped and Ga-doped ZnO showing a rapid decrease in intensity in the high temperature region (200-300K). The activation energies for this temperature range are 180 meV and 510 meV for undoped and Ga-doped ZnO, respectively.

Table 7.1: Activation energies for undoped and Ga-doped ZnO at different temperature ranges.

Doping in at%	Temperature in K		
	10–70	80–190	200–300
0	4 meV	17 meV	180 meV
1.4	5 meV	36 meV	510 meV

From these experimental results, it can be concluded that two types of possible recombination channels are responsible for this intense YL and RL emissions in Ga-doped ZnO nanorods. First, the conduction band electrons can relax to a lower energy donor level at low temperature, and the RL emission is produced by the electronic transitions from the lower energy donor level to Ga_{Zn}-V_{Zn} deep acceptor state. Second, the electron could be localised at a higher energy level at the higher temperature. The transition from this higher energy electron level to deep state causes a blueshift. So, the YL emission in Ga-doped ZnO nanorods is due to the direct transition from the conduction band electron to Ga_{Zn}-V_{Zn} acceptor state. A similar temperature-dependent blueshift of 240 meV has previously been reported in Ga-doped ZnO nanorods [248].

7.4.5. Colour-tunable LEDs in ZnO by Ga doping

EL from the ZnO nanorod/p-Si heterojunction LEDs is observed when the Si side of the heterostructure is positively biased and was sufficiently intense to be clearly observed by the naked eye at applied bias above 6 V. EL spectra acquired under identical conditions at room temperature, shown in Figure 7.12 (a), reveal increased EL intensity by an order of magnitude when Ga-doped nanorods are used in the ZnO/p-Si heterojunction LED device. The LED fabricated from undoped ZnO nanorods exhibits a predominantly YL EL centred at 2.05 eV, which is quenched upon doping with Ga. For Ga-doped nanorods, the LEDs exhibit a strong RL EL band peaking at 1.78 eV. A typical CL spectrum of updoped ZnO nanorods consist of a weak near-band-edge ultraviolet emission and an intense defect-related green emission band at 2.43 eV, which is characteristic of O-rich grown ZnO nanowires with a high concentration of V_{Zn} defects [44]. Conversely the EL from LED devices only emits light in the visible range, indicating the EL emission originates from radiative recombination of injected carriers at deep level defects in ZnO nanorods. The EL integrated intensity and current injection into the LEDs are plotted as a function of applied voltage in Figure 7.12 (b). The current through the nanorod LED increases remarkably with increasing Ga concentration due to higher conductivity in the Ga-doped nanorods. The EL intensity from a LED device fabricated with 1.4 at% Ga-doped ZnO nanorods is higher than the identical device made with pristine ZnO nanorods by one order of magnitude at the same bias voltage.

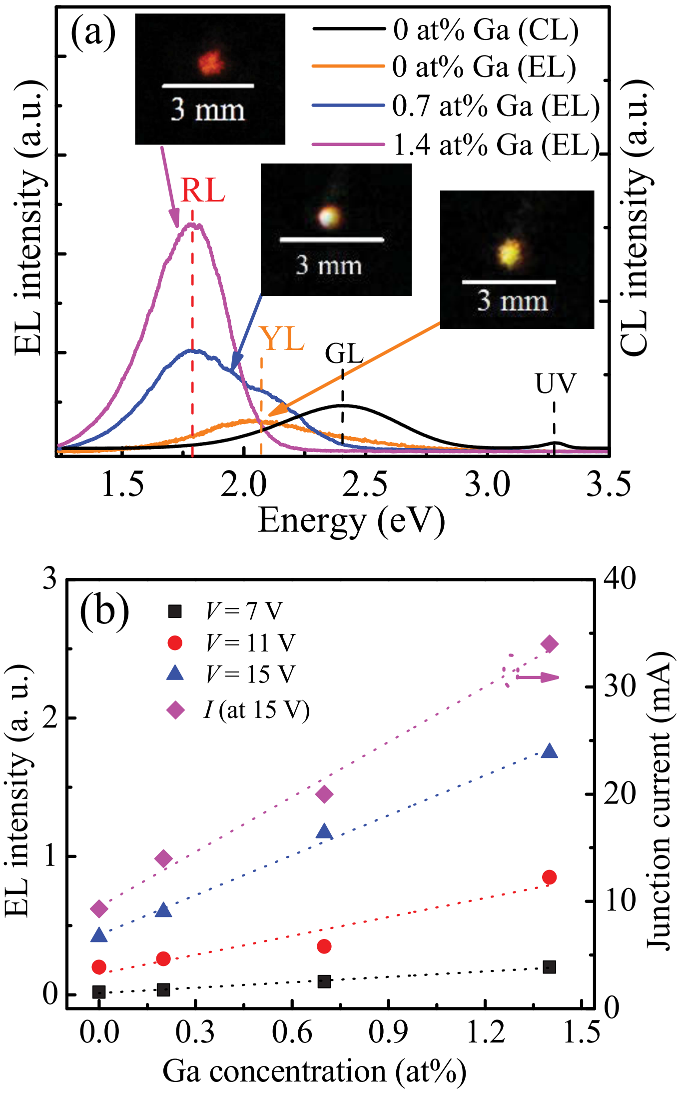

Figure 7.12. (a) Room temperature EL spectra of ZnO nanorod/p-Si LED devices that are fabricated with different Ga doping levels and their corresponding photos of the EL emission. The CL spectrum of the undoped ZnO nanorods is also shown for comparison. The LED devices display two chromaticity-stable emission bands independent of applied voltage: yellow at 2.05 eV and red at 1.78 eV. With increasing Ga concentration in the nanorods, the EL is shifted from yellow to red band, and increases dramatically in intensity. (b) EL integrated intensity and junction current as a function of Ga concentration at different bias voltages.

The observation of the major differences between EL and CL of the Ga-doped nanorods is interesting but complicated. Figures 7.13 (a)-(d)) show the EL spectra of nanorod LEDs at different Ga doping concentration acquired under different bias voltages. With increasing forward bias voltage, the EL intensity increases without changes in the spectral shape and emission energy, indicating that the EL arises from the heterojunction without Joule heating effects, allowing for stable and durable nanorod-based LEDs. This is a significant advantage of the direct growth of Ga-doped ZnO nanorods on Si (and other thermally conductive substrates) as the Si substrate acts as an excellent heat-sink for the nanorod heterojunction [249], which makes the chromaticity of the LED thermally stable. In nanosized junctions such as in the p-Si/nanorod LED the depletion region is influenced by interface and edge effects. The absence of the GL emission in the EL spectra of the LED can be explained by the fact that V_{Zn} centres are passivated by forming $\mathrm{Ga_{Zn}}$-$\mathrm{V_{Zn}}$ complexes in highly Ga-doped ZnO [79, 86].

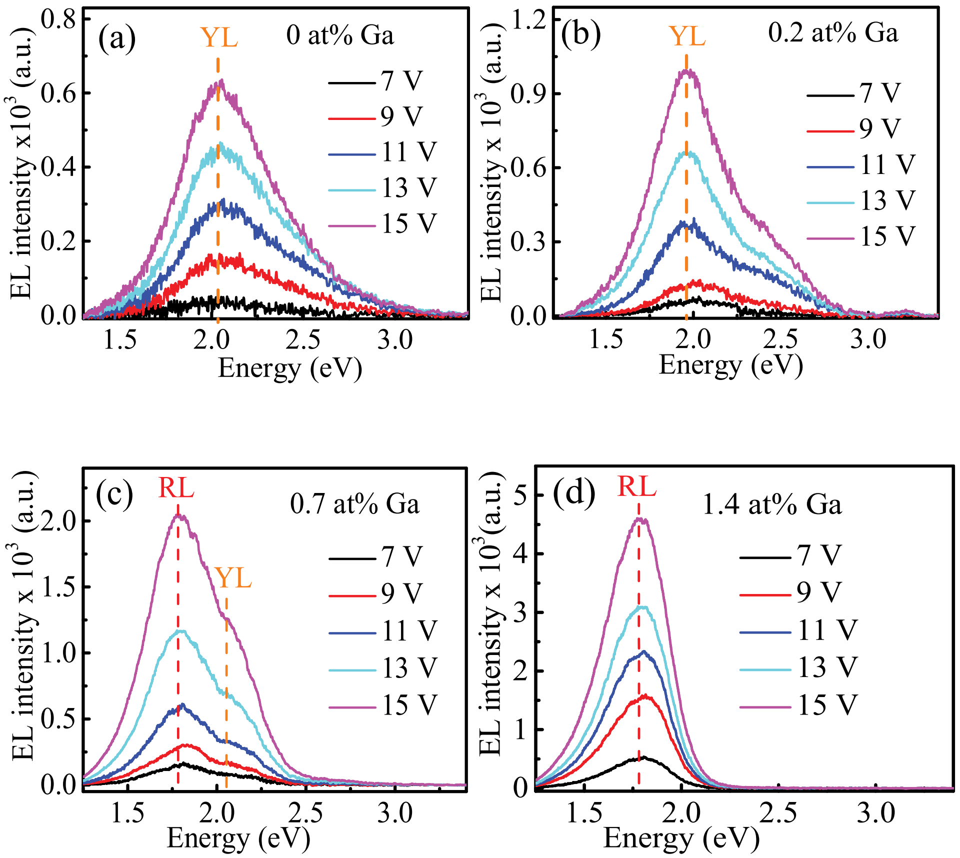

Figure 7.13. (a) – (d) EL spectra of Ga-doped ZnO nanorod/p-Si LED devices acquired at different forward-bias voltages showing two emission bands: YL at 2.05 eV and RL at 1.78 eV. With increasing forward bias voltage, the EL intensity increasing without changing the spectral shape and emission energy, indicating the EL arising from the heterojunction without Joule heating effects, allowing for stable and durable nanorod-based LEDs.

A possible mechanism responsible for the EL enhancement due to the Ga doping of the ZnO nanorods is illustrated in the band alignment diagram of the p-Si/ZnO heterojunction (Figure 7.14), derived from the Anderson model [250]. Based on the electron affinities of Si, ψ_{Si}, and ZnO, ψ_{ZnO}, the band offsets are expected to be $\Delta E_c \sim 0.3$ and $\Delta E_v \sim 2.5$ eV. The large ΔE_v value means that hole injection into the valence band of undoped ZnO is strongly suppressed, leading to low light emission in the LED based on undoped nanorod. This problem could be overcome by Ga doping, which results in deep acceptor states, especially Ga_{Zn}-V_{Zn} and Ga_{Zn}-O_i [24, 86], thus reducing bias voltage required to inject holes into ZnO nanorods. Under forward bias, the Si bands are shifted downwards, moving the Si valence band closer to the acceptor states in Ga-doped ZnO. At low bias voltages (in which the LED obeys Ohm's law), holes tunnel from p-Si to n-ZnO through the thin SiO_x layer; this mechanism is consistent with the linear I-V relation in region I. At sufficiently high voltages, it is likely that an inversion layer of holes is formed in Si underneath the SiO_x layer [251, 252]. The rapid enhancement of EL intensity with Ga concentration can be explained by the formation of abundant Ga_{Zn}-V_{Zn} pairs in the Ga-doped ZnO nanorods, which enable a highly efficient injection of holes into the Ga-doped nanorods where radiative recombination occurs. This mechanism is consistent with the exponential current rise in region II of the I-V curve.

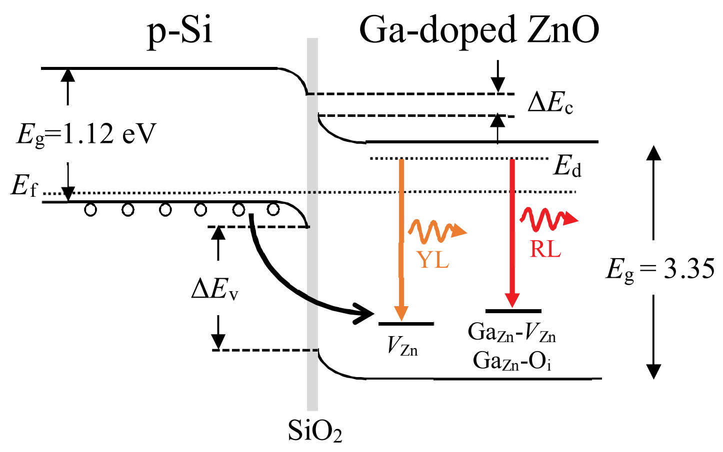

Figure 7.14. Energy band diagram for p-Si/Ga-doped ZnO heterojunction at thermal equilibrium. The bandgap discontinuity at conduction band and valence band is therefore equal to $\Delta E_c = \psi_{ZnO} - \psi_{Si} = 0.3\, eV$ and $\Delta E_v = E_{g,ZnO} - E_{g,Si} + E_c = 2.5\, eV$. Approximate positions of the defect levels are drawn based on the calculated values of V_{Zn}, Ga_{Zn}-V_{Zn} and Ga_{Zn}-O_i. Arrows indicate radiative recombination channels in Ga-doped ZnO after hole injection from p-Si.

7.5. Conclusions

ZnO nanorods doped with Ga donors by *in-situ* dopant incorporation during vapour-solid growth exhibit superior optoelectronic properties and accordingly can be electrically integrated into Si-based photonic devices. Significantly, in addition to increasing the conductivity, Ga donor doping was found to improve the nanorod quality by decreasing the concentration of point defects. Light emitting diodes fabricated from the Ga-doped ZnO nanorod/p-Si heterojunction displayed bright and colour-tunable electroluminescence. These nanorod LEDs possess a dramatically enhanced performance and an order of magnitude higher EL compared with equivalent devices made with pristine nanorods. These results point to an effective route for large-scale fabrication of conductive, single-crystalline ZnO nanorods for photonic and optoelectronic applications.

Chapter 8

Conclusions and outlook

8.1. Conclusions

In summary, doped ZnO nanostructures were successfully grown by the spray pyrolysis and vapour phase transport methods. The donor and acceptor impurities and their effects on the optoelectronic properties of ZnO nanostructures were investigated. Moreover, vertically aligned ZnO nanorods were electrically integrated in Si-based optoelectronic devices in order to fabricate colour-tunable light emitting diodes.

First, Li-doped ZnO thin films with efficient, multi-coloured emissions were successfully fabricated by the spray pyrolysis technique. The films exhibit yellow, green and blue emissions, which can be tuned by varying the Li doping concentration. The V_{Zn}-associated green luminescence in the ZnO film can be medicated by Li dopants. The characteristic parameters of the visible luminescence centres obtained from the Huang-Rhys simulation of the CL spectra of the pyrolytic films are similar to the reported values for V_{Zn} and Li_{Zn} defects in ZnO films fabricated by high-temperature growth.

Second, the carrier-mediated switching behaviour of Cu acceptors in ZnO nanorods by Ga doping was investigated. Using the vapour-liquid-solid growth, Ga is *in-situ* incorporated substitutionally at Zn lattice sites in nanorods without compromising the crystal quality, producing Ga donor-bound exciton signatures in ZnO. The Ga donor doping increases the carrier density, which pushes the Fermi-level above the $Cu^{+/2+}$ charge transfer level, producing doublet fine structures in the green band. This luminescence band is attributed to hole transition to the negatively charged Cu^{+} state located at 390 eV above the valence band.

Third, the bandgap engineering in a single ZnO microstructure with a graded distribution of Ga was studied. The ultraviolet emission peak was found to be red shifted by 0.6 eV and broadens with increasing local Ga concentration from 1.5 to 6 at%. This emission band from the Ga-doped ZnO microrods has characteristics of a near-band-edge emission. Theoretical calculations indicate that the decrease of bandgap arises from the merging of Ga defect complexes with ZnO energy bands. The broadening of the NBE emission monotonically increases with Ga concentration, which can be explained in terms of alloy potential fluctuations. These results demonstrate self-regulation of charged defect compensation and the possibility of multi-wavelength light sources within a microstructure.

Finally, the optimised Ga-doped ZnO nanorods were used to fabricate Si-based photonic devices. LED devices fabricated from the p-Si/Ga-doped ZnO nanorods heterojunctions exhibited a lower turn-on voltage, lower series resistance and enhanced EL, with the emission intensity increased by an order of magnitude than the device fabricated with undoped ZnO nanorods. The nanorod-based LEDs display light emission in the visible range, which are attributed to defect-related emissions in Ga-doped ZnO. Furthermore, the chromaticity of the LED devices can be tuned from yellow to red by varying the Ga content in the ZnO nanorods.

8.2. Outlook

Although ZnO has attracted a considerable attention in optoelectronic applications, a few controversial issues still need be further investigation for the improvement of ZnO-based applications. New ideas for the fabrication of stable p-type ZnO with a high hole concentration are required to fabricate the ZnO-based homojunction light emitting devices with improved light extraction efficiency. In this project, the growth of Ga-doped ZnO nanorods and their integration in light emitting devices have been accomplished. Continued research work of controlling Ga doping in a single ZnO nano/microrods and their properties, as examined in the chapter 6, is of special interest, particularly in the possibility of single ZnO nano/microrod- based photonic devices.

It has been observed that the Ga-doping into ZnO nano/microrods can be used for tuning the emission colour in the ultraviolet (chapter 6) and visible (chapter 7) spectral regions. Hexagonal ZnO nano/microrods with controlled Ga doping concentration could be used for tuning the optical resonant modes in the ultraviolet and visible spectral range. A hexagonal Ga-doped ZnO microrod with variable diameter along its length (see Figure 8.1 below) could have the potential for optical resonant mode engineering in a single nano/microrod. Fundamental physics under the surface plasmonic effect of gold and the application beyond the visible and ultraviolet lasing of ZnO could be an interesting research area of future work.

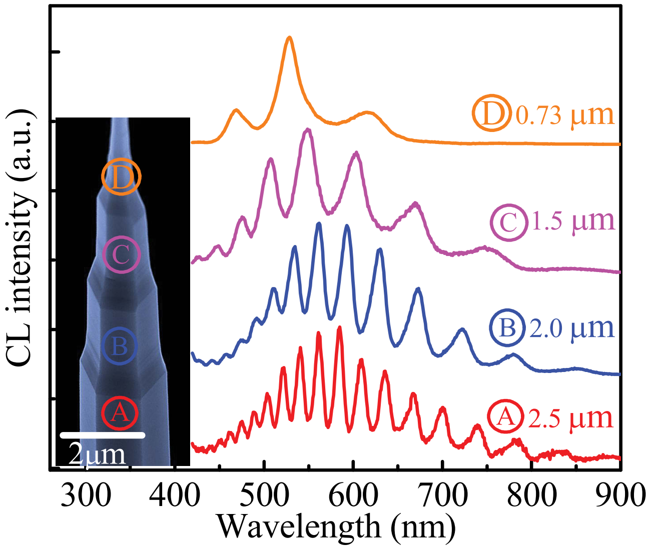

Figure 8.1. A hexagonal microrod with diameter varying between 2.5 and 0.73 µm from bottom to top. Optical resonance mode recorded locally by CL at different section of the microrod showing a decrease in the resonance mode number with decreasing diameter of the microrod.

References

[1] S. Su, C. Ling, F. Azad, H. Zeng, Y. Lu, S. Xing, Fabrication and Modification of n-ZnO/p-GaN Heterojunction Light Emitting Diodes with White Light Emission Characteristics, Nanoscience and Nanotechnology Letters, 9 (2017) 880-884.

[2] M.H. Huang, S. Mao, H. Feick, H. Yan, Y. Wu, H. Kind, E. Weber, R. Russo, P. Yang, Room-temperature ultraviolet nanowire nanolasers, Science, 292 (2001) 1897-1899.

[3] K. Matsubara, P. Fons, K. Iwata, A. Yamada, K. Sakurai, H. Tampo, S. Niki, ZnO transparent conducting films deposited by pulsed laser deposition for solar cell applications, Thin Solid Films, 431 (2003) 369-372.

[4] K. Vanheusden, C. Seager, W.t. Warren, D. Tallant, J. Voigt, Correlation between photoluminescence and oxygen vacancies in ZnO phosphors, Applied Physics Letters, 68 (1996) 403-405.

[5] A. Janotti, C.G. Van de Walle, Fundamentals of zinc oxide as a semiconductor, Reports on Progress in Physics, 72 (2009) 126501.

[6] Ü. Özgür, Y.I. Alivov, C. Liu, A. Teke, M. Reshchikov, S. Doğan, V. Avrutin, S.-J. Cho, H. Morkoc, A comprehensive review of ZnO materials and devices, Journal of Applied Physics, 98 (2005) 11.

[7] C. Park, S. Zhang, S.-H. Wei, Origin of p-type doping difficulty in ZnO: The impurity perspective, Physical Review B, 66 (2002) 073202.

[8] E.-C. Lee, K. Chang, Possible p-type doping with group-I elements in ZnO, Physical Review B, 70 (2004) 115210.

[9] A. Carvalho, A. Alkauskas, A. Pasquarello, A. Tagantsev, N. Setter, A hybrid density functional study of lithium in ZnO: Stability, ionization levels, and diffusion, Physical Review B, 80 (2009) 195205.

[10] M. Wardle, J. Goss, P. Briddon, Theory of Li in ZnO: A limitation for Li-based p-type doping, Physical Review B, 71 (2005) 155205.

[11] J. Lee, S. Cha, J. Kim, H. Nam, S. Lee, W. Ko, K.L. Wang, J. Park, J. Hong, p-Type Conduction Characteristics of Lithium-Doped ZnO Nanowires, Advanced Materials, 23 (2011) 4183-4187.

[12] G. Du, Y. Ma, Y. Zhang, T. Yang, Preparation of intrinsic and N-doped p-type ZnO thin films by metalorganic vapor phase epitaxy, Applied Physics Letters, 87 (2005) 213103.

[13] W. Liu, F. Xiu, K. Sun, Y.-H. Xie, K.L. Wang, Y. Wang, J. Zou, Z. Yang, J. Liu, Na-doped p-type ZnO microwires, Journal of the American Chemical Society, 132 (2010) 2498-2499.

[14] G.Z. Xing, J.B. Yi, J.G. Tao, T. Liu, L.M. Wong, Z. Zhang, G.P. Li, S.J. Wang, J. Ding, T.C. Sum, Comparative Study of Room-Temperature Ferromagnetism in Cu-Doped ZnO Nanowires Enhanced by Structural Inhomogeneity, Advanced Materials, 20 (2008) 3521-3527.

[15] C.-L. Hsu, Y.-D. Gao, Y.-S. Chen, T.-J. Hsueh, Vertical p-type Cu-doped ZnO/n-type ZnO homojunction nanowire-based ultraviolet photodetector by the furnace system with hotwire assistance, ACS Applied Materials & Interfaces, 6 (2014) 4277-4285.

[16] M. Younas, R. Lortz, S.-C. Su, F. Ling, Observation of Room Temperature Ferromagnetism in Conducting and Insulating Cu doped ZnO Thin Films, Journal of Superconductivity and Novel Magnetism, 28 (2015) 855-858.

[17] D. Buchholz, R. Chang, J.-Y. Song, J. Ketterson, Room-temperature ferromagnetism in Cu-doped ZnO thin films, Applied Physics Letters, 87 (2005) 082504.

[18] A. Tiwari, M. Snure, D. Kumar, J.T. Abiade, Ferromagnetism in Cu-doped ZnO films: Role of charge carriers, Applied Physics Letters, 92 (2008) 062509.

[19] K. Sato, H. Katayama-Yoshida, Material design for transparent ferromagnets with ZnO-based magnetic semiconductors, Japanese Journal of Applied Physics, 39 (2000) L555.

[20] M.A. Reshchikov, V. Avrutin, N. Izyumskaya, R. Shimada, H. Morkoc, S. Novak, About the Cu-related green luminescence band in ZnO, Journal of Vacuum Science & Technology B: Microelectronics and Nanometer Structures Processing, Measurement, and Phenomena, 27 (2009) 1749-1754.

[21] Y. Liu, H. Liang, L. Xu, J. Zhao, J. Bian, Y. Luo, Y. Liu, W. Li, G. Wu, G. Du, Cu related doublets green band emission in ZnO: Cu thin films, Journal of Applied Physics, 108 (2010) 113507.

[22] D. Reynolds, D.C. Look, B. Jogai, Fine structure on the green band in ZnO, Journal of Applied Physics, 89 (2001) 6189-6191.

[23] B. Meyer, Alves, H, D. Hofmann, W. Kriegseis, D. Forster, F. Bertram, J. Christen, A. Hoffmann, M. Straßburg, M. Dworzak, Bound exciton and donor–acceptor pair recombinations in ZnO, Physica Status Solidi (b), 241 (2004) 231-260.

[24] D. Demchenko, B. Earles, H. Liu, V. Avrutin, N. Izyumskaya, Ü. Özgür, H. Morkoç, Impurity complexes and conductivity of Ga-doped ZnO, Physical Review B, 84 (2011) 075201.

[25] S.Y. Bae, C.W. Na, J.H. Kang, J. Park, Comparative structure and optical properties of Ga-, In-, and Sn-doped ZnO nanowires synthesized via thermal evaporation, The Journal of Physical Chemistry B, 109 (2005) 2526-2531.

[26] J. Kim, G.V. Naik, A.V. Gavrilenko, K. Dondapati, V.I. Gavrilenko, S. Prokes, O.J. Glembocki, V.M. Shalaev, A. Boltasseva, Optical properties of gallium-doped zinc oxide—a low-loss plasmonic material: first-principles theory and experiment, Physical Review X, 3 (2013) 041037.

[27] G.V. Naik, J. Kim, A. Boltasseva, Oxides and nitrides as alternative plasmonic materials in the optical range, Optical Materials Express, 1 (2011) 1090-1099.

[28] G.D. Yuan, W.J. Zhang, J.S. Jie, X. Fan, J.X. Tang, I. Shafiq, Z.Z. Ye, C.S. Lee, S.T. Lee, Tunable n-Type Conductivity and Transport Properties of Ga-doped ZnO Nanowire Arrays, Advanced Materials, 20 (2008) 168-173.

[29] X. Zhang, L. Li, J. Su, Y. Wang, Y. Shi, X. Ren, N. Liu, A. Zhang, J. Zhou, Y. Gao, Bandgap engineering of GaxZn1−xO nanowire arrays for wavelength-tunable light-emitting diodes, Laser & Photonics Reviews, 8 (2014) 429-435.

[30] J. T-Thienprasert, S. Rujirawat, W. Klysubun, J. Duenow, T. Coutts, S. Zhang, D. Look, S. Limpijumnong, Compensation in Al-doped ZnO by Al-related acceptor complexes: synchrotron X-ray absorption spectroscopy and theory, Physical Review Letters, 110 (2013) 055502.

[31] U. Ozgur, D. Hofstetter, H. Morkoc, ZnO devices and applications: a review of current status and future prospects, Proceedings of the IEEE, 98 (2010) 1255-1268.

[32] E. Lai, W. Kim, P. Yang, Vertical nanowire array-based light emitting diodes, Nano Research, 1 (2008) 123-128.

[33] F. Selim, M. Weber, D. Solodovnikov, K. Lynn, Nature of native defects in ZnO, Physical Review Letters, 99 (2007) 085502.

[34] D.C. Look, G.C. Farlow, P. Reunchan, S. Limpijumnong, S. Zhang, K. Nordlund, Evidence for native-defect donors in n-type ZnO, Physical Review Letters, 95 (2005) 225502.

[35] A. Janotti, C.G. Van de Walle, Native point defects in ZnO, Physical Review B, 76 (2007) 165202.

[36] A. Janotti, C.G. Van de Walle, Oxygen vacancies in ZnO, Applied Physics Letters, 87 (2005) 122102.

[37] L. Kappers, O. Gilliam, S. Evans, L. Halliburton, N. Giles, EPR and optical study of oxygen and zinc vacancies in electron-irradiated ZnO, Nuclear Instruments and Methods in Physics Research Section B: Beam Interactions with Materials and Atoms, 266 (2008) 2953-2957.

[38] F. Oba, M. Choi, A. Togo, I. Tanaka, Point defects in ZnO: an approach from first principles, Science and Technology of Advanced Materials, 12 (2011) 034302.

[39] P. Erhart, A. Klein, K. Albe, First-principles study of the structure and stability of oxygen defects in zinc oxide, Physical Review B, 72 (2005) 085213.

[40] P. Erhart, K. Albe, A. Klein, First-principles study of intrinsic point defects in ZnO: Role of band structure, volume relaxation, and finite-size effects, Physical Review B, 73 (2006) 205203.

[41] A. Janotti, C.G. Van de Walle, Hydrogen multicentre bonds, Nature Materials, 6 (2007) 44.

[42] F. Leiter, H. Alves, A. Hofstaetter, D. Hofmann, B. Meyer, The oxygen vacancy as the origin of a green emission in undoped ZnO, Physica Status Solidi (b), 226 (2001) R4-R5.

[43] T.M. Børseth, B. Svensson, A.Y. Kuznetsov, P. Klason, Q. Zhao, M. Willander, Identification of oxygen and zinc vacancy optical signals in ZnO, Applied Physics Letters, 89 (2006) 262112.

[44] C. Ton-That, L. Weston, M. Phillips, Characteristics of point defects in the green luminescence from Zn-and O-rich ZnO, Physical Review B, 86 (2012) 115205.

[45] J. Ye, S. Gu, F. Qin, S. Zhu, S. Liu, X. Zhou, W. Liu, L. Hu, R. Zhang, Y. Shi, Correlation between green luminescence and morphology evolution of ZnO films, Applied Physics A, 81 (2005) 759-762.

[46] D. Hofmann, D. Pfisterer, J. Sann, B. Meyer, R. Tena-Zaera, V. Munoz-Sanjose, T. Frank, G. Pensl, Properties of the oxygen vacancy in ZnO, Applied Physics A, 88 (2007) 147-151.

[47] F. Tuomisto, V. Ranki, K. Saarinen, D.C. Look, Evidence of the Zn vacancy acting as the dominant acceptor in n-type ZnO, Physical Review Letters, 91 (2003) 205502.

[48] A. Kohan, G. Ceder, D. Morgan, C.G. Van de Walle, First-principles study of native point defects in ZnO, Physical Review B, 61 (2000) 15019.

[49] S. Lany, A. Zunger, Dopability, intrinsic conductivity, and nonstoichiometry of transparent conducting oxides, Physical Review Letters, 98 (2007) 045501.

[50] X. Wang, L. Vlasenko, S. Pearton, W. Chen, I.A. Buyanova, Oxygen and zinc vacancies in as-grown ZnO single crystals, Journal of Physics D: Applied Physics, 42 (2009) 175411.

[51] S. Evans, N. Giles, L. Halliburton, L. Kappers, Further characterization of oxygen vacancies and zinc vacancies in electron-irradiated ZnO, Journal of Applied Physics, 103 (2008) 043710.

[52] S. Lima, F. Sigoli, M. Jafelicci Jr, M.R. Davolos, Luminescent properties and lattice defects correlation on zinc oxide, International Journal of Inorganic Materials, 3 (2001) 749-754.

[53] V. Nikitenko, Optics and spectroscopy of point defects in ZnO, in: Zinc Oxide—A Material for Micro-and Optoelectronic Applications, Springer, 2005, pp. 69-81.

[54] P. Thiyagarajan, M. Kottaisamy, N. Rama, M.R. Rao, White light emitting diode synthesis using near ultraviolet light excitation on Zinc oxide–Silicon dioxide nanocomposite, Scripta Materialia, 59 (2008) 722-725.

[55] A. Djurišić, A. Ng, X. Chen, ZnO nanostructures for optoelectronics: material properties and device applications, Progress in Quantum Electronics, 34 (2010) 191-259.

[56] B. Lin, Z. Fu, Y. Jia, Green luminescent center in undoped zinc oxide films deposited on silicon substrates, Applied Physics Letters, 79 (2001) 943-945.

[57] S. Choi, M.R. Phillips, I. Aharonovich, S. Pornsuwan, B.C. Cowie, C. Ton-That, Photophysics of Point Defects in ZnO Nanoparticles, Advanced Optical Materials, 3 (2015) 821-827.

[58] P. Xu, Y. Sun, C. Shi, F. Xu, H. Pan, The electronic structure and spectral properties of ZnO and its defects, Nuclear Instruments and Methods in Physics Research Section B: Beam Interactions with Materials and Atoms, 199 (2003) 286-290.

[59] J. Hu, B. Pan, Electronic structures of defects in ZnO: hybrid density functional studies, The Journal of Chemical Physics, 129 (2008) 154706.

[60] N. Alvi, K. Ul Hasan, O. Nur, M. Willander, The origin of the red emission in n-ZnO nanotubes/p-GaN white light emitting diodes, Nanoscale Research Letters, 6 (2011) 130.

[61] A. Escobedo-Morales, U. Pal, Defect annihilation and morphological improvement of hydrothermally grown ZnO nanorods by Ga doping, Applied Physics Letters, 93 (2008) 193120.

[62] C. Xu, X. Sun, X. Zhang, L. Ke, S. Chua, Photoluminescent properties of copper-doped zinc oxide nanowires, Nanotechnology, 15 (2004) 856.

[63] C.G. Van de Walle, Hydrogen as a cause of doping in zinc oxide, Physical Review Letters, 85 (2000) 1012.

[64] E. Lavrov, J. Weber, F. Börrnert, C.G. Van de Walle, R. Helbig, Hydrogen-related defects in ZnO studied by infrared absorption spectroscopy, Physical Review B, 66 (2002) 165205.

[65] J. Lv, C. Li, Evidences of VO, VZn, and Oi defects as the green luminescence origins in ZnO, Applied Physics Letters, 103 (2013) 232114.

[66] X. Wu, G. Siu, C. Fu, H. Ong, Photoluminescence and cathodoluminescence studies of stoichiometric and oxygen-deficient ZnO films, Applied Physics Letters, 78 (2001) 2285-2287.

[67] R. Dingle, Luminescent transitions associated with divalent copper impurities and the green emission from semiconducting zinc oxide, Physical Review Letters, 23 (1969) 579.

[68] N. Garces, L. Wang, L. Bai, N. Giles, L. Halliburton, G. Cantwell, Role of copper in the green luminescence from ZnO crystals, Applied Physics Letters, 81 (2002) 622-624.

[69] V. Kumar, H. Swart, O. Ntwaeaborwa, R. Kroon, J. Terblans, S. Shaat, A. Yousif, M. Duvenhage, Origin of the red emission in zinc oxide nanophosphors, Materials Letters, 101 (2013) 57-60.

[70] A.R. Gheisi, C. Neygandhi, A.K. Sternig, E. Carrasco, H. Marbach, D. Thomele, O. Diwald, O 2 adsorption dependent photoluminescence emission from metal oxide nanoparticles, Physical Chemistry Chemical Physics, 16 (2014) 23922-23929.

[71] X. Liu, X. Wu, H. Cao, R. Chang, Growth mechanism and properties of ZnO nanorods synthesized by plasma-enhanced chemical vapor deposition, Journal of Applied Physics, 95 (2004) 3141-3147.

[72] C.H. Ahn, Y.Y. Kim, D.C. Kim, S.K. Mohanta, H.K. Cho, A comparative analysis of deep level emission in ZnO layers deposited by various methods, Journal of Applied Physics, 105 (2009) 013502.

[73] D. Zwingel, Trapping and recombination processes in the thermoluminescence of Li-doped ZnO single crystals, Journal of Luminescence, 5 (1972) 385-405.

[74] Z. Zhang, K.E. Knutsen, T. Merz, A.Y. Kuznetsov, B. Svensson, L. Brillson, Thermal process dependence of Li configuration and electrical properties of Li-doped ZnO, Applied Physics Letters, 100 (2012) 042107.

[75] R. Sahu, K. Dileep, B. Loukya, R. Datta, Native defects affecting the Li atom distribution tune the optical emission of ZnO: Li epitaxial thin film, Applied Physics Letters, 104 (2014) 051908.

[76] B. Meyer, J. Sann, A. Zeuner, Lithium and sodium acceptors in ZnO, Superlattices and Microstructures, 38 (2005) 344-348.

[77] L. Brillson, Z. Zhang, D. Doutt, D. Look, B. Svensson, A.Y. Kuznetsov, F. Tuomisto, Interplay of dopants and native point defects in ZnO, Physica Status Solidi (b), 250 (2013) 2110-2113.

[78] A. Tang, Z. Mei, Y. Hou, L. Liu, V. Venkatachalapathy, A. Azarov, A. Kuznetsov, X. Du, Ga Zn-V Zn acceptor complex defect in Ga-doped ZnO, Science China Physics, Mechanics & Astronomy, 61 (2018) 077311.

[79] H. Matsui, H. Saeki, H. Tabata, T. Kawai, Role of Ga for Co-doping of Ga with N in ZnO Films, Japanese Journal of Applied Physics, 42 (2003) 5494.

[80] M. Jiang, G. He, H. Chen, Z. Zhang, L. Zheng, C. Shan, D. Shen, X. Fang, Wavelength-Tunable Electroluminescent Light Sources from Individual Ga-Doped ZnO Microwires, Small, 13 (2017).

[81] G.-H. He, M.-M. Jiang, L. Dong, Z.-Z. Zhang, B.-H. Li, C.-X. Shan, D.-Z. Shen, Near-infrared light-emitting devices from individual heavily Ga-doped ZnO microwires, Journal of Materials Chemistry C, 5 (2017) 2542-2551.

[82] D. Thomas, Interstitial zinc in zinc oxide, Journal of Physics and Chemistry of Solids, 3 (1957) 229-237.

[83] D.C. Look, J.W. Hemsky, J. Sizelove, Residual native shallow donor in ZnO, Physical Review Letters, 82 (1999) 2552.

[84] Y.-Y. Peng, T.-E. Hsieh, C.-H. Hsu, White-light emitting ZnO–SiO2 nanocomposite thin films prepared by the target-attached sputtering method, Nanotechnology, 17 (2005) 174.

[85] L.J. Brillson, Y. Dong, F. Tuomisto, B.G. Svensson, A.Y. Kuznetsov, D. Doutt, H.L. Mosbacker, G. Cantwell, J. Zhang, J.J. Song, Interplay of native point defects with ZnO Schottky barriers and doping, Journal of Vacuum Science & Technology B, 30 (2012) 050801.

[86] A. Tang, Z. Mei, Y. Hou, L. Liu, V. Venkatachalapathy, A. Azarov, A. Kuznetsov, X. Du, GaZn-VZn acceptor complex defect in Ga-doped ZnO, Cond-Mat.Mtrl-Sci., arXiv:1709.07603 (2017).

[87] Y.-S. Lee, Y.-C. Peng, J.-H. Lu, Y.-R. Zhu, H.-C. Wu, Electronic and optical properties of Ga-doped ZnO, Thin Solid Films, 570 (2014) 464-470.

[88] M.-H. Lee, Y.-C. Peng, H.-C. Wu, Effects of intrinsic defects on electronic structure and optical properties of Ga-doped ZnO, Journal of Alloys and Compounds, 616 (2014) 122-127.

[89] T. Yamada, K. Ikeda, S. Kishimoto, H. Makino, T. Yamamoto, Effects of oxygen partial pressure on doping properties of Ga-doped ZnO films prepared by ion-plating with traveling substrate, Surface and Coatings Technology, 201 (2006) 4004-4007.

[90] C.-Y. Tsay, K.-S. Fan, C.-M. Lei, Synthesis and characterization of sol–gel derived gallium-doped zinc oxide thin films, Journal of Alloys and Compounds, 512 (2012) 216-222.

[91] J.B. Park, Y.T. Chun, Y.B. Lee, J.I. Sohn, W.-K. Hong, Defect-mediated modulation of optical properties in vertically aligned ZnO nanowires via substrate-assisted Ga incorporation, Nanotechnology, 26 (2015) 145202.

[92] B. Meyer, J. Sann, S. Lautenschläger, M. Wagner, A. Hoffmann, Ionized and neutral donor-bound excitons in ZnO, Physical Review B, 76 (2007) 184120.

[93] E. Tomzig, R. Helbig, Band-edge emission in ZnO, Journal of Luminescence, 14 (1976) 403-415.

[94] Z. Yang, D.C. Look, J. Liu, Ga-related photoluminescence lines in Ga-doped ZnO grown by plasma-assisted molecular-beam epitaxy, Applied Physics Letters, 94 (2009) 072101.

[95] D.C. Look, R. Jones, J. Sizelove, N.Y. Garces, N.C. Giles, L.E. Halliburton, The path to ZnO devices: donor and acceptor dynamics, Physica Status Solidi (a), 195 (2003) 171-177.

[96] R.T. Ginting, C.C. Yap, M. Yahaya, M. Mat Salleh, Solution-processed Ga-doped ZnO nanorod arrays as electron acceptors in organic solar cells, ACS Applied Materials & Interfaces, 6 (2014) 5308-5318.

[97] H. He, Z. Wang, H. Duan, Z. Ye, Band tail-induced photoluminescence broadening in heavily In-doped n-type ZnO nanowires, Physical Chemistry Chemical Physics, 17 (2015) 17552-17556.

[98] K.J. Kim, Y.R. Park, Large and abrupt optical band gap variation in In-doped ZnO, Applied Physics Letters, 78 (2001) 475-477.

[99] G.V. Naik, V.M. Shalaev, A. Boltasseva, Alternative plasmonic materials: beyond gold and silver, Advanced Materials, 25 (2013) 3264-3294.

[100] R. Vidya, P. Ravindran, H. Fjellvåg, Ab-initio studies on Li doping, Li-pairs, and complexes between Li and intrinsic defects in ZnO, Journal of Applied Physics, 111 (2012) 123713.

[101] C. Rauch, W. Gehlhoff, M. Wagner, E. Malguth, G. Callsen, R. Kirste, B. Salameh, A. Hoffmann, S. Polarz, Y. Aksu, Lithium related deep and shallow acceptors in Li-doped ZnO nanocrystals, Journal of Applied Physics, 107 (2010) 024311.

[102] A. Hoffmann, E. Malguth, B. Meyer, Deep Centres in ZnO, in: Zinc Oxide, Springer, 2010, pp. 233-266.

[103] D. Huang, Y.-J. Zhao, D.-H. Chen, Y.-Z. Shao, Magnetism and clustering in Cu doped ZnO, Applied Physics Letters, 92 (2008) 182509.

[104] Y.-J. Zhao, C. Persson, S. Lany, A. Zunger, Why can CuInSe 2 be readily equilibrium-doped n-type but the wider-gap CuGaSe 2 cannot?, Applied Physics Letters, 85 (2004) 5860-5862.

[105] M. Wardle, J. Goss, P. Briddon, Theory of Fe, Co, Ni, Cu, and their complexes with hydrogen in ZnO, Physical Review B, 72 (2005) 155108.

[106] Y. Yan, M. Al-Jassim, S.-H. Wei, Doping of ZnO by group-IB elements, Applied physics letters, 89 (2006) 181912.

[107] E. Mollwo, G. Müller, P. Wagner, Energetische lage des Cu-akzeptorniveaus in ZnO-Einkristallen, Solid State Communications, 13 (1973) 1283-1287.

[108] Y. Kanai, Admittance spectroscopy of Cu-doped ZnO crystals, Japanese Journal of Applied Physics, 30 (1991) 703.

[109] P. Dahan, V. Fleurov, P. Thurian, R. Heitz, A. Hoffmann, I. Broser, Properties of the intermediately bound and-excitons in ZnO: Cu, Journal of Physics: Condensed Matter, 10 (1998) 2007.

[110] M.D. McCluskey, C.D. Corolewski, J. Lv, M.C. Tarun, S.T. Teklemichael, E.D. Walter, M.G. Norton, K.W. Harrison, S. Ha, Acceptors in ZnO, Journal of Applied Physics, 117 (2015) 112802.

[111] P. Carcia, R. McLean, M. Reilly, G. Nunes Jr, Transparent ZnO thin-film transistor fabricated by rf magnetron sputtering, Applied Physics Letters, 82 (2003) 1117-1119.

[112] T. Minami, S. Ida, T. Miyata, Y. Minamino, Transparent conducting ZnO thin films deposited by vacuum arc plasma evaporation, Thin Solid Films, 445 (2003) 268-273.

[113] N. Bouhssira, S. Abed, E. Tomasella, J. Cellier, A. Mosbah, M. Aida, M. Jacquet, Influence of annealing temperature on the properties of ZnO thin films deposited by thermal evaporation, Applied Surface Science, 252 (2006) 5594-5597.

[114] S.T. Tan, B. Chen, X. Sun, W. Fan, H.S. Kwok, X. Zhang, S. Chua, Blueshift of optical band gap in ZnO thin films grown by metal-organic chemical-vapor deposition, Journal of Applied Physics, 98 (2005) 013505.

[115] Y. Nakanishi, A. Miyake, H. Kominami, T. Aoki, Y. Hatanaka, G. Shimaoka, Preparation of ZnO thin films for high-resolution field emission display by electron beam evaporation, Applied Surface Science, 142 (1999) 233-236.

[116] V. Musat, B. Teixeira, E. Fortunato, R. Monteiro, P. Vilarinho, Al-doped ZnO thin films by sol–gel method, Surface and Coatings Technology, 180 (2004) 659-662.

[117] B. Jin, S. Im, S.Y. Lee, Violet and UV luminescence emitted from ZnO thin films grown on sapphire by pulsed laser deposition, Thin Solid Films, 366 (2000) 107-110.

[118] J. Wang, L. Gao, Hydrothermal synthesis and photoluminescence properties of ZnO nanowires, Solid State Communications, 132 (2004) 269-271.

[119] R. Wagner, W. Ellis, Vapor-liquid-solid mechanism of single crystal growth, Applied Physics Letters, 4 (1964) 89-90.

[120] S.C. Lyu, Y. Zhang, C.J. Lee, H. Ruh, H.J. Lee, Low-Temperature Growth of ZnO Nanowire Array by a Simple Physical Vapor-Deposition Method, Chemistry of Materials, 15 (2003) 3294-3299.

[121] A. Umar, S.H. Kim, Y.S. Lee, K.S. Nahm, Y.B. Hahn, Catalyst-free large-quantity synthesis of ZnO nanorods by a vapor–solid growth mechanism: Structural and optical properties, Journal of Crystal Growth, 282 (2005) 131-136.

[122] N. Roy, A. Roy, Growth and temperature dependent photoluminescence characteristics of ZnO tetrapods, Ceramics International, 41 (2015) 4154-4160.

[123] M.S. Kim, J.-Y. Leem, D.Y. Kim, S.-O. Kim, D.-Y. Lee, Catalyst-free ZnO on porous silicon grown by using vapor phase transport, Journal of the Korean Physical Society, 60 (2012) 1129-1134.

[124] H.K. Yu, J.-L. Lee, Growth mechanism of metal-oxide nanowires synthesized by electron beam evaporation: A self-catalytic vapor-liquid-solid process, Scientific Reports, 4 (2014) 6589.

[125] G.C. Yi, Semiconductor Nanostructures for Optoelectronic Devices: Processing, Characterization and Applications, Springer Berlin Heidelberg, 2012.

[126] M. Zhou, H. Zhu, Y. Jiao, Y. Rao, S. Hark, Y. Liu, L. Peng, Q. Li, Optical and electrical properties of Ga-doped ZnO nanowire arrays on conducting substrates, The Journal of Physical Chemistry C, 113 (2009) 8945-8947.

[127] W.-K. Hong, G. Jo, M. Choe, T. Lee, J.I. Sohn, M.E. Welland, Influence of surface structure on the phonon-assisted emission process in the ZnO nanowires grown on homoepitaxial films, Applied Physics Letters, 94 (2009) 043103.

[128] C.-L. Hsu, S.-J. Chang, H.-C. Hung, Y.-R. Lin, C.-J. Huang, Y.-K. Tseng, I.-C. Chen, Vertical single-crystal ZnO nanowires grown on ZnO: Ga/glass templates, IEEE Transactions on Nanotechnology, 4 (2005) 649-654.

[129] C.H. Ahn, W.S. Han, B.H. Kong, H.K. Cho, Ga-doped ZnO nanorod arrays grown by thermal evaporation and their electrical behavior, Nanotechnology, 20 (2008) 015601.

[130] C. Xu, M. Kim, J. Chun, D. Kim, Growth of Ga-doped ZnO nanowires by two-step vapor phase method, Applied Physics Letters, 86 (2005) 133107.

[131] C. Xu, X. Sun, B. Chen, P. Shum, S. Li, X. Hu, Nanostructural zinc oxide and its electrical and optical properties, Journal of Applied Physics, 95 (2004) 661-666.

[132] C.-L. Hsu, Y.-R. Lin, S.-J. Chang, T.-H. Lu, T.-S. Lin, S.-Y. Tsai, I.-C. Chen, Influence of the Formation of the Second Phase in ZnO⁄Ga Nanowire Systems, Journal of The Electrochemical Society, 153 (2006) G333-G336.

[133] L. Zhu, Doping and characterisation of ZnO nanowires and crystals, in, 2015.

[134] J.E. Allen, E.R. Hemesath, D.E. Perea, J.L. Lensch-Falk, Z.Y. Li, F. Yin, M.H. Gass, P. Wang, A.L. Bleloch, R.E. Palmer, L.J. Lauhon, High-resolution detection of Au catalyst atoms in Si nanowires, Nature Nanotechnology, 3 (2008) 168.

[135] J. Yoo, Y.-J. Hong, S.J. An, G.-C. Yi, B. Chon, T. Joo, J.-W. Kim, J.-S. Lee, Photoluminescent characteristics of Ni-catalyzed GaN nanowires, Applied Physics Letters, 89 (2006) 043124.

[136] L. Zhu, M.R. Phillips, C. Ton-That, Coalescence of ZnO nanowires grown from monodisperse Au nanoparticles, CrystEngComm, 17 (2015) 4987-4991.

[137] A. Cheol Hyoun, H. Won Suk, K. Bo Hyun, C. Hyung Koun, Ga-doped ZnO nanorod arrays grown by thermal evaporation and their electrical behavior, Nanotechnology, 20 (2009) 015601.

[138] C.-H. Chen, S.-J. Chang, S.-P. Chang, M.-J. Li, I.-C. Chen, T.-J. Hsueh, A.-D. Hsu, C.-L. Hsu, Fabrication of a white-light-emitting diode by doping gallium into ZnO nanowire on a p-GaN substrate, The Journal of Physical Chemistry C, 114 (2010) 12422-12426.

[139] S.-J. Chang, B.-G. Duan, C.-H. Hsiao, C.-W. Liu, S.-J. Young, UV enhanced emission performance of low temperature grown Ga-doped ZnO nanorods, Photonics Technology Letters, IEEE, 26 (2014) 66-69.

[140] L. Zhu, C. Ton-That, M.R. Phillips, Nitrogen incorporation in ZnO nanowires using N2O dopant gas, Materials Letters, 99 (2013) 42-45.

[141] S. Sakrani, N. Jamaludin, R. Muhammad, Y. Wahab, A. Ismail, S. Suhaimi, Y. Mohammed, Effect of gas flow rate on structural properties of zinc oxide nanowires grown by vapor-solid mechanism, in: AIP Conference Proceedings, AIP Publishing, 2016, pp. 020040.

[142] L.-l. Yang, J.-h. Yang, D.-d. Wang, Y.-j. Zhang, Y.-x. Wang, H.-l. Liu, H.-g. Fan, J.-h. Lang, Photoluminescence and Raman analysis of ZnO nanowires deposited on Si (1 0 0) via vapor–liquid–solid process, Physica E: Low-dimensional Systems and Nanostructures, 40 (2008) 920-923.

[143] K. Seshan, D. Schepis, Handbook of thin film deposition, William Andrew, 2018.

[144] D. Pashley, M. Stowell, M. Jacobs, T. Law, The growth and structure of gold and silver deposits formed by evaporation inside an electron microscope, Philosophical Magazine, 10 (1964) 127-158.

[145] M. Volmer, A. Weber, Keimbildung in übersättigten Gebilden, Zeitschrift für physikalische Chemie, 119 (1926) 277-301.

[146] R. Becker, W. Doring, Kinetic treatment of the nucleation in supersaturated vapors, (1954).

[147] D. Pashley, The nucleation, growth, structure and epitaxy of thin surface films, Advances in Physics, 14 (1965) 327-416.

[148] F. Zahedi, R. Dariani, S. Rozati, Effect of substrate temperature on the properties of ZnO thin films prepared by spray pyrolysis, Materials Science in Semiconductor Processing, 16 (2013) 245-249.

[149] T.P. Rao, M. Santhoshkumar, Effect of thickness on structural, optical and electrical properties of nanostructured ZnO thin films by spray pyrolysis, Applied Surface Science, 255 (2009) 4579-4584.

[150] P. Nunes, A. Malik, B. Fernandes, E. Fortunato, P. Vilarinho, R. Martins, Influence of the doping and annealing atmosphere on zinc oxide thin films deposited by spray pyrolysis, Vacuum, 52 (1999) 45-49.

[151] S. Ramachandran, J. Narayan, J. Prater, Effect of oxygen annealing on Mn doped ZnO diluted magnetic semiconductors, Applied Physics Letters, 88 (2006) 242503.

[152] J. Dong, X. Zhang, J. You, P. Cai, Z. Yin, Q. An, X. Ma, P. Jin, Z. Wang, P.K. Chu, Effects of hydrogen plasma treatment on the electrical and optical properties of ZnO films: identification of hydrogen donors in ZnO, ACS Applied Materials & Interfaces, 2 (2010) 1780-1784.

[153] S. Lee, S. Bang, J. Park, S. Park, W. Jeong, H. Jeon, The effect of oxygen remote plasma treatment on ZnO TFTs fabricated by atomic layer deposition, Physica Status Solidi (a), 207 (2010) 1845-1849.

[154] Z. Zang, A. Nakamura, J. Temmyo, Nitrogen doping in cuprous oxide films synthesized by radical oxidation at low temperature, Materials Letters, 92 (2013) 188-191.

[155] S. Chu, J. Lim, L. Mandalapu, Z. Yang, L. Li, J. Liu, Sb-doped p-Zn O∕Ga-doped n-Zn O homojunction ultraviolet light emitting diodes, Applied Physics Letters, 92 (2008) 152103.

[156] Z. Yang, S. Chu, W.V. Chen, L. Li, J. Kong, J. Ren, K. Paul, J. Liu, ZnO: Sb/ZnO: Ga light emitting diode on c-plane sapphire by molecular beam epitaxy, Applied Physics Express, 3 (2010) 032101.

[157] G.C. Park, S.M. Hwang, J.H. Lim, J. Joo, Growth behavior and electrical performance of Ga-doped ZnO nanorod/p-Si heterojunction diodes prepared using a hydrothermal method, Nanoscale, 6 (2014) 1840-1847.

[158] R. Li, C. Yu, H. Dong, W. Jia, T. Li, Z. Zhang, B. Xu, Effects of Ga x Zn 1− x O nanorods on the photoelectric properties of n-ZnO nanorods/p-GaN heterojunction light-emitting diodes, RSC Advances, 7 (2017) 49613-49617.

[159] Y. Liu, M. Jiang, G. He, S. Li, Z. Zhang, B. Li, H. Zhao, C. Shan, D. Shen, Wavelength-Tunable Ultraviolet Electroluminescence from Ga-Doped ZnO Microwires, ACS Applied Materials & Interfaces, 9 (2017) 40743-40751.

[160] M.K. Choi, W.S. Han, Y.Y. Kim, B.H. Kong, H.K. Cho, J.H. Kim, H.-S. Seo, K.-P. Kim, J.-H. Lee, n-ZnO: Ga/i-ZnO/p-Si heterojunction light emitting diodes fabricated on patterned Si substrates, Journal of Materials Science: Materials in Electronics, 20 (2009) 1214-1218.

[161] D.-T. Phan, G.-S. Chung, Effects of defects in Ga-doped ZnO nanorods formed by a hydrothermal method on CO sensing properties, Sensors and Actuators B: Chemical, 187 (2013) 191-197.

[162] W.S. Han, Y.Y. Kim, B.H. Kong, H.K. Cho, J.Y. Moon, H.S. Lee, Improvement of the Light Extraction Efficiency in n-ZnO: Ga/p-Si Heterojunction Light Emitting Diodes by a SiO2 Current-Blocking Layer, Japanese Journal of Applied Physics, 48 (2009) 08HK03.

[163] J.H. Lim, S.M. Lee, H.-S. Kim, H.Y. Kim, J. Park, S.-B. Jung, G.C. Park, J. Kim, J. Joo, Synergistic effect of Indium and Gallium co-doping on growth behavior and physical properties of hydrothermally grown ZnO nanorods, Scientific Reports, 7 (2017) 41992.

[164] M.K.R. Khan, M.A. Rahman, M. Shahjahan, M.M. Rahman, M.A. Hakim, D.K. Saha, J.U. Khan, Effect of Al-doping on optical and electrical properties of spray pyrolytic nano-crystalline CdO thin films, Current Applied Physics, 10 (2010) 790-796.

[165] S.S. Kumar, E. Rubio, M. Noor-A-Alam, G. Martinez, S. Manandhar, V. Shutthanandan, S. Thevuthasan, C. Ramana, Structure, morphology, and optical properties of amorphous and nanocrystalline gallium oxide thin films, The Journal of Physical Chemistry C, 117 (2013) 4194-4200.

[166] W. Han, S. Fan, Q. Li, Y. Hu, Synthesis of gallium nitride nanorods through a carbon nanotube-confined reaction, Science, 277 (1997) 1287-1289.

[167] J. Hu, Y. Bando, Z. Liu, Synthesis of Gallium-Filled Gallium Oxide–Zinc Oxide Composite Coaxial Nanotubes, Advanced Materials, 15 (2003) 1000-1003.

[168] D. Yu, T. Trad, J.T. McLeskey, V. Craciun, C.R. Taylor, ZnO Nanowires Synthesized by Vapor Phase Transport Deposition on Transparent Oxide Substrates, Nanoscale Research Letters, 5 (2010) 1333.

[169] B.G. Yacobi, D.B. Holt, Cathodoluminescence microscopy of inorganic solids, Springer Science & Business Media, 2013.

[170] C. Ton-That, M. Phillips, Cathodoluminescence microanalysis of ZnO nanowires, in: Semiconductor Nanowires, Elsevier, 2015, pp. 393-407.

[171] J.H. Walker, Spectral irradiance calibrations, US Department of Commerce, National Bureau of Standards, 1987.

[172] A. Grün, Lumineszenz-photometrische messungen der energieabsorption im strahlungsfeld von elektronenquellen eindimensionaler fall in luft, Zeitschrift für Naturforschung A, 12 (1957) 89-95.

[173] M.R. Phillips, H. Telg, S.O. Kucheyev, O. Gelhausen, M. Toth, Cathodoluminescence efficiency dependence on excitation density in n-type gallium nitride, Microscopy and Microanalysis, 9 (2003) 144-151.

[174] S.M. Sze, K.K. Ng, Metal-semiconductor contacts, Wiley Online Library, 2006.

[175] H. Von Wenckstern, E. Kaidashev, M. Lorenz, H. Hochmuth, G. Biehne, J. Lenzner, V. Gottschalch, R. Pickenhain, M. Grundmann, Lateral homogeneity of Schottky contacts on n-type ZnO, Applied Physics Letters, 84 (2004) 79-81.

[176] Y. Zeng, Z. Ye, W. Xu, D. Li, J. Lu, L. Zhu, B. Zhao, Dopant source choice for formation of p-type ZnO: Li acceptor, Applied Physics Letters, 88 (2006) 062107.

[177] M.A. Rahman, M.R. Phillips, C. Ton-That, Efficient multi-coloured Li-doped ZnO thin films fabricated by spray pyrolysis, Journal of Alloys and Compounds, 691 (2017) 339-342.

[178] S. Shinde, C. Bhosale, K. Rajpure, Photoelectrochemical properties of highly mobilized Li-doped ZnO thin films, Journal of Photochemistry and Photobiology B: Biology, 120 (2013) 1-9.

[179] M. Joseph, H. Tabata, T. Kawai, Ferroelectric behavior of Li-doped ZnO thin films on Si (100) by pulsed laser deposition, Applied Physics Letters, 74 (1999) 2534-2536.

[180] A.Y. Oral, Z.B. Bahşi, M.H. Aslan, Microstructure and optical properties of nanocrystalline ZnO and ZnO:(Li or Al) thin films, Applied Surface Science, 253 (2007) 4593-4598.

[181] M. Caglar, Y. Caglar, S. Aksoy, S. Ilican, Temperature dependence of the optical band gap and electrical conductivity of sol–gel derived undoped and Li-doped ZnO films, Applied Surface Science, 256 (2010) 4966-4971.

[182] M.A. Rahman, M. Khan, Effect of annealing temperature on structural, electrical and optical properties of spray pyrolytic nanocrystalline CdO thin films, Materials Science in Semiconductor Processing, 24 (2014) 26-33.

[183] G. Harris, X. Quantitative measurement of preferred orientation in rolled uranium bars, The London, Edinburgh, and Dublin Philosophical Magazine and Journal of Science, 43 (1952) 113-123.

[184] K.-H. Wu, L.-Y. Peng, M. Januar, K.-C. Chiu, K.-C. Liu, Fabrication and optimization process of p-type Li: ZnO oxide semiconductor, Thin Solid Films, 570 (2014) 417-422.

[185] H.-J. Fitting, T. Barfels, A. Trukhin, B. Schmidt, A. Gulans, A. Von Czarnowski, Cathodoluminescence of Ge+, Si+, and O+ implanted SiO2 layers and the role of mobile oxygen in defect transformations, Journal of Non-Crystalline Solids, 303 (2002) 218-231.

[186] D. Drouin, A.R. Couture, D. Joly, X. Tastet, V. Aimez, R. Gauvin, CASINO V2. 42—A Fast and Easy-to-use Modeling Tool for Scanning Electron Microscopy and Microanalysis Users, Scanning, 29 (2007) 92-101.

[187] H. Ong, A. Li, G. Du, Depth profiling of ZnO thin films by cathodoluminescence, Applied Physics Letters, 78 (2001) 2667-2669.

[188] K. Huang, A. Rhys, Theory of light absorption and non-radiative transitions in F-centres, Proceedings of the Royal Society London A, 204 (1950) 406-423.

[189] Y. Jin, G. Li, L. Zhang, Electron-lattice coupling in ZnFe 2 O 4⁄ TiO 2 nanocomposite films, Applied Physics Letters, 86 (2005) 091906.

[190] Y. Tay, T. Tan, S. Li, Determinants of the structured and structureless green emissions of ZnO, Solid State Communications, 151 (2011) 372-376.

[191] A. Carvalho, A. Alkauskas, A. Pasquarello, A. Tagantsev, N. Setter, Li-related defects in ZnO: Hybrid functional calculations, Physica B: Condensed Matter, 404 (2009) 4797-4799.

192] B.K. Meyer, J. Stehr, A. Hofstaetter, N. Volbers, A. Zeuner, J. Sann, On the role of group I elements in ZnO, Applied Physics A, 88 (2007) 119-123.

[193] N. Kouklin, Cu-Doped ZnO Nanowires for Efficient and Multispectral Photodetection Applications, Advanced Materials, 20 (2008) 2190-2194.

[194] C.-w. Zhang, C. Han, S.-s. Yan, F.-b. Zheng, Design of ferromagnetism in Cu-doped ZnO nanowires: First-principles prediction, Europhysics Letters, 95 (2011) 47011.

[195] N.J. Pearce, W.T. Perkins, J.A. Westgate, M.P. Gorton, S.E. Jackson, C.R. Neal, S.P. Chenery, A compilation of new and published major and trace element data for NIST SRM 610 and NIST SRM 612 glass reference materials, Geostandards and Geoanalytical Research, 21 (1997) 115-144.

[196] M.A. Rahman, M.T. Westerhausen, C. Nenstiel, S. Choi, A. Hoffmann, A. Gentle, M.R. Phillips, C. Ton-That, Charge state switching of Cu acceptors in ZnO nanorods, Applied Physics Letters, 110 (2017) 121907.

[197] K. Johnston, M.O. Henry, D. McCabe, E. McGlynn, M. Dietrich, E. Alves, M. Xia, Identification of donor-related impurities in ZnO using photoluminescence and radiotracer techniques, Physical Review B, 73 (2006) 165212.

[198] B. Wei, K. Zheng, Y. Ji, Y. Zhang, Z. Zhang, X. Han, Size-Dependent Bandgap Modulation of ZnO Nanowires by Tensile Strain, Nano Letters, 12 (2012) 4595-4599.

[199] D.C. Look, K. Leedy, L. Vines, B. Svensson, A. Zubiaga, F. Tuomisto, D.R. Doutt, L. Brillson, Self-compensation in semiconductors: The Zn vacancy in Ga-doped ZnO, Physical Review B, 84 (2011) 115202.

[200] M. Grundmann, The Physics of Semiconductors: An Introduction Including Nanophysics and Applications, Springer, 2015.

[201] M. Oshikiri, Y. Imanaka, F. Aryasetiawan, G. Kido, Comparison of the electron effective mass of the n-type ZnO in the wurtzite structure measured by cyclotron resonance and calculated from first principle theory, Physica B: Condensed Matter, 298 (2001) 472-476.

[202] Z. Ye, Y. Zeng, Y. Lu, S. Lin, L. Sun, L. Zhu, B. Zhao, Donor/acceptor doping and electrical tailoring in ZnO quantum dots, Applied Physics Letters, 91 (2007) 112110.

[203] W. Baer, Faraday rotation in ZnO: Determination of the electron effective mass, Physical Review, 154 (1967) 785.

[204] S. Mukamel, Principles of nonlinear optical spectroscopy, Oxford University Press on Demand, 1999.

[205] R. Kuhnert, R. Helbig, Vibronic structure of the green photoluminescence due to copper impurities in ZnO, Journal of Luminescence, 26 (1981) 203-206.

[206] F. Qian, Y. Li, S. Gradečak, H.-G. Park, Y. Dong, Y. Ding, Z.L. Wang, C.M. Lieber, Multi-quantum-well nanowire heterostructures for wavelength-controlled lasers, Nature Materials, 7 (2008) 701.

[207] P. Kumar, H.K. Malik, A. Ghosh, R. Thangavel, K. Asokan, Bandgap tuning in highly c-axis oriented Zn1− xMgxO thin films, Applied Physics Letters, 102 (2013) 221903.

[208] X. Wang, Y. Jin, H. He, F. Yang, Y. Yang, Z. Ye, Bandgap engineering and shape control of colloidal Cd x Zn 1− x O nanocrystals, Nanoscale, 5 (2013) 6464-6468.

[209] J. Khoshman, D. Ingram, M. Kordesch, Bandgap engineering in amorphous Be x Zn y O thin films, Applied Physics Letters, 92 (2008) 091902.

[210] K. Iwata, P. Fons, A. Yamada, H. Shibata, K. Matsubara, K. Nakahara, H. Takasu, S. Niki, Bandgap engineering of ZnO using Se, Physica Status Solidi (b), 229 (2002) 887-890.

[211] D.P. Joseph, C. Venkateswaran, Bandgap engineering in ZnO by doping with 3d transition metal ions, Journal of Atomic, Molecular, and Optical Physics, 2011 (2011).

[212] H. Hung-Chun Lai, T. Basheer, V.L. Kuznetsov, R.G. Egdell, R.M. Jacobs, M. Pepper, P.P. Edwards, Dopant-induced bandgap shift in Al-doped ZnO thin films prepared by spray pyrolysis, Journal of Applied Physics, 112 (2012) 083708.

[213] M. Osada, T. Sakemi, T. Yamamoto, The effects of oxygen partial pressure on local structural properties for Ga-doped ZnO thin films, Thin Solid Films, 494 (2006) 38-41.

[214] T. Makino, Y. Segawa, S. Yoshida, A. Tsukazaki, A. Ohtomo, M. Kawasaki, Gallium concentration dependence of room-temperature near-band-edge luminescence in n-type ZnO: Ga, Applied Physics Letters, 85 (2004) 759-761.

[215] T. Makino, Y. Segawa, S. Yoshida, A. Tsukazaki, A. Ohtomo, M. Kawasaki, H. Koinuma, Spectral shape analysis of ultraviolet luminescence in n-type ZnO: Ga, Journal of Applied Physics, 98 (2005) 093520.

[216] J. De-Sheng, Y. Makita, K. Ploog, H. Queisser, Electrical properties and photoluminescence of Te-doped GaAs grown by molecular beam epitaxy, Journal of Applied Physics, 53 (1982) 999-1006.

[217] E. Iliopoulos, D. Doppalapudi, H. Ng, T. Moustakas, Broadening of near-band-gap photoluminescence in n-GaN films, Applied Physics Letters, 73 (1998) 375-377.

[218] E. Schubert, I. Goepfert, W. Grieshaber, J. Redwing, Optical properties of Si-doped GaN, Applied Physics Letters, 71 (1997) 921-923.

[219] J.M. Soler, E. Artacho, J.D. Gale, A. García, J. Junquera, P. Ordejón, D. Sánchez-Portal, The SIESTA method for ab initio order-N materials simulation, Journal of Physics: Condensed Matter, 14 (2002) 2745.

[220] J.P. Perdew, K. Burke, M. Ernzerhof, Generalized gradient approximation made simple, Physical Review Letters, 77 (1996) 3865.

[221] N. Troullier, J.L. Martins, Efficient pseudopotentials for plane-wave calculations, Physical Review B, 43 (1991) 1993.

[222] J. Wróbel, K.J. Kurzydłowski, K. Hummer, G. Kresse, J. Piechota, Calculations of ZnO properties using the Heyd-Scuseria-Ernzerhof screened hybrid density functional, Physical Review B, 80 (2009) 155124.

[223] H.-C. Wu, Y.-C. Peng, C.-C. Chen, Effects of Ga concentration on electronic and optical properties of Ga-doped ZnO from first principles calculations, Optical Materials, 35 (2013) 509-515.

[224] J. Zhao, X. Sun, H. Ryu, Y. Moon, Thermally stable transparent conducting and highly infrared reflective Ga-doped ZnO thin films by metal organic chemical vapor deposition, Optical Materials, 33 (2011) 768-772.

[225] E. Burstein, Anomalous optical absorption limit in InSb, Physical Review, 93 (1954) 632.

[226] T. Moss, The interpretation of the properties of indium antimonide, Proceedings of the Physical Society. Section B, 67 (1954) 775.

[227] S. Maximenko, L. Mazeina, Y. Picard, J. Freitas Jr, V. Bermudez, S. Prokes, Cathodoluminescence studies of the inhomogeneities in Sn-doped Ga2O3 nanowires, Nano Letters, 9 (2009) 3245-3251.

[228] S. Chu, G. Wang, W. Zhou, Y. Lin, L. Chernyak, J. Zhao, J. Kong, L. Li, J. Ren, J. Liu, Electrically pumped waveguide lasing from ZnO nanowires, Nature Nanotechnology, 6 (2011) 506.

[229] R. Yan, D. Gargas, P. Yang, Nanowire photonics, Nature Photonics, 3 (2009) 569.

[230] C. Zhang, C.E. Marvinney, H.Y. Xu, W.Z. Liu, C.L. Wang, L.X. Zhang, J.N. Wang, J.G. Ma, Y.C. Liu, Enhanced waveguide-type ultraviolet electroluminescence from ZnO/MgZnO core/shell nanorod array light-emitting diodes via coupling with Ag nanoparticles localized surface plasmons, Nanoscale, 7 (2015) 1073-1080.

[231] M. Chen, C. Pan, T. Zhang, X. Li, R. Liang, Z.L. Wang, Tuning light emission of a pressure-sensitive silicon/ZnO nanowires heterostructure matrix through piezo-phototronic effects, ACS Nano, 10 (2016) 6074-6079.

[232] W.I. Park, G.C. Yi, Electroluminescence in n-ZnO Nanorod Arrays Vertically Grown on p-GaN, Advanced Materials, 16 (2004) 87-90.

[233] S.W. Eaton, A. Fu, A.B. Wong, C.-Z. Ning, P. Yang, Semiconductor nanowire lasers, Nature Reviews Materials, 1 (2016) 16028.

[234] H. Zhu, C.X. Shan, B. Yao, B.H. Li, J.Y. Zhang, Z.Z. Zhang, D.X. Zhao, D.Z. Shen, X.W. Fan, Y.M. Lu, Ultralow-Threshold Laser Realized in Zinc Oxide, Advanced Materials, 21 (2009) 1613-1617.

[235] Y. Yang, Y. Li, C. Wang, C. Zhu, C. Lv, X. Ma, D. Yang, Rare-Earth Doped ZnO Films: A Material Platform to Realize Multicolor and Near-Infrared Electroluminescence, Advanced Optical Materials, 2 (2014) 240-244.

[236] F. Gao, D. Zhang, J. Wang, H. Sun, Y. Yin, Y. Sheng, S. Yan, B. Yan, C. Sui, Y. Zheng, Ultraviolet electroluminescence from Au-ZnO nanowire Schottky type light-emitting diodes, Applied Physics Letters, 108 (2016) 261103.

[237] O. Lupan, T. Pauporté, B. Viana, Low-temperature growth of ZnO nanowire arrays on p-Silicon (111) for visible-light-emitting diode fabrication, The Journal of Physical Chemistry C, 114 (2010) 14781-14785.

[238] A. Jana, S. Ghosh, P.S. Devi, N.R. Bandyopadhyay, M. Ray, Tunable charge transport through n-ZnO nanorods on Au coated macroporous p-Si, Journal of Materials Chemistry C, 2 (2014) 9613-9619.

[239] K. Kim, Y. Jeon, K. Cho, S. Kim, Enhancement of Trap-Assisted Green Electroluminescence Efficiency in ZnO/SiO2/Si Nanowire Light-Emitting Diodes on Bendable Substrates by Piezophototronic Effect, ACS Applied Materials & Interfaces, 8 (2016) 2764-2773.

[240] T. Cao, L. Luo, Y. Huang, B. Ye, J. She, S. Deng, J. Chen, N. Xu, Integrated ZnO Nano-Electron-Emitter with Self-Modulated Parasitic Tunneling Field Effect Transistor at the Surface of the p-Si/ZnO Junction, Scientific Reports, 6 (2016) 33983.

[241] Z. Shi, D. Wu, T. Xu, Y. Zhang, B. Zhang, Y. Tian, X. Li, G. Du, Improved electrical transport and electroluminescence properties of p-ZnO/n-Si heterojunction via introduction of patterned SiO2 intermediate layer, The Journal of Physical Chemistry C, 120 (2016) 4504-4510.

[242] E.F. Schubert, T. Gessmann, J.K. Kim, Light emitting diodes, Cambridge University Press, Cambridge, U.K., 2006.

[243] M. Wagner, G. Callsen, J. Reparaz, J.-H. Schulze, R. Kirste, M. Cobet, I. Ostapenko, S. Rodt, C. Nenstiel, M. Kaiser, Bound excitons in ZnO: Structural defect complexes versus shallow impurity centers, Physical Review B, 84 (2011) 035313.

[244] J. Krustok, H. Collan, K. Hjelt, Does the low-temperature Arrhenius plot of the photoluminescence intensity in CdTe point towards an erroneous activation energy?, Journal of Applied Physics, 81 (1997) 1442-1445.

[245] Y.P. Varshni, Temperature dependence of the energy gap in semiconductors, Physica, 34 (1967) 149-154.

[246] M. Manasreh, Optical absorption near the band edge in GaN grown by metalorganic chemical-vapor deposition, Physical Review B, 53 (1996) 16425.

[247] I. Shalish, H. Temkin, V. Narayanamurti, Size-dependent surface luminescence in ZnO nanowires, Physical Review B, 69 (2004) 245401.

[248] X. Zhao, Y. Gao, Y. Wang, H.V. Demir, S. Wang, H. Sun, Manipulating Optical Properties of ZnO/Ga: ZnO Core–Shell Nanorods Via Spatially Tailoring Electronic Bandgap, Advanced Optical Materials, 3 (2015) 1066-1071.

[249] S. Chung, J.-H. Lee, J. Jeong, J.-J. Kim, Y. Hong, Substrate thermal conductivity effect on heat dissipation and lifetime improvement of organic light-emitting diodes, Applied Physics Letters, 94 (2009) 168.

[250] R. Anderson, Germanium-gallium arsenide heterojunctions [letter to the editor], IBM Journal of Research and Development, 4 (1960) 283-287.

[251] S. Tan, X. Sun, J. Zhao, S. Iwan, Z. Cen, T. Chen, J. Ye, G. Lo, D. Kwong, K. Teo, Ultraviolet and visible electroluminescence from n-Zn O/ Si O x/(n, p)-Si heterostructured light-emitting diodes, Applied Physics Letters, 93 (2008) 013506.

[252] Y. Xu, Y. Li, H. Zhang, L. Jin, X. Fang, L. Shi, L. Xu, X. Ma, Y. Zou, J. Yin, Ultraviolet-enhanced electroluminescence from individual ZnO microwire/p-Si light-emitting diode by reverse tunneling effect, Journal of Materials Chemistry C, 5 (2017) 6640-6646.